



Production de phi et omega dans les collisions PbPb a 158 GeV par nucléon

Tao Wu

► To cite this version:

Tao Wu. Production de phi et omega dans les collisions PbPb a 158 GeV par nucléon. Nuclear Theory [nucl-th]. Université Paris Sud - Paris XI, 2003. English. NNT : . tel-00004516

HAL Id: tel-00004516

<https://theses.hal.science/tel-00004516>

Submitted on 5 Feb 2004

HAL is a multi-disciplinary open access archive for the deposit and dissemination of scientific research documents, whether they are published or not. The documents may come from teaching and research institutions in France or abroad, or from public or private research centers.

L'archive ouverte pluridisciplinaire **HAL**, est destinée au dépôt et à la diffusion de documents scientifiques de niveau recherche, publiés ou non, émanant des établissements d'enseignement et de recherche français ou étrangers, des laboratoires publics ou privés.

IPNO-T-03-03-04

THESE de DOCTORAT de l'UNIVERSITE PARIS XI

Spécialité

Physique Nucléaire et des Particules

présentée

par M. Wu Tao

pour obtenir le grade de DOCTORAT de l'UNIVERSITE PARIS XI

subject de thèse

Production de ϕ et ω dans les collisions Pb–Pb à 158 GeV par nucleon

Soutenue le 21 Octobre 2003 à l'institut de physique nucleaire d'Orsay

devant le jury composé de:

Madame SCHIFF Dominique	Présidente
Monsieur BAUBILLIER Michel	Rapporteur
Monsieur GAZDZIKI Marek	Rapporteur
Monsieur JOUAN Denis	
Monsieur ZHOU Daicui	
Monsieur CAI XU	

Preface

*Who has seen the wind?
Neither I nor you,
But when the leaves hang trembling,
The wind is passing through.
Who has seen the wind?
Neither you nor I,
But when the trees bow down their heads,
The wind is passing by.*

Acknowledgments

This thesis would not have been possible without the help from my advisor, Mr. Denis Jouan. I wish to give my deepest gratitude to him for his patient guidance and warm-hearted care. I also wish to express my sincerest respect for his hardworking spirits and serious attitude to the science, which has always been inspiring to me and encouraging me.

I would like to thank Professor Daicui Zhou for his assistance during my graduate life, who leads me into the field of High-Energy Heavy-Ion Collision Physics. His devoted working spirits and the cooperative spirits are always affecting me and stimulating me.

I also would like to thank Professor Xu Cai, for his pilot and developmental help. His attractive personality, his unique eye-sight into the nature, and his characteristic outlook and philosophy of the life have been impressing and impacting me.

Working with colleagues and folks in the NA50 collaboration group, they have been very harmonious and friendly. Last but not least, I thank all my fellow graduate friends, who have made my three years at Orsay and Wuhan very enjoyable.

Any words couldn't express myself to my parents!

Abstract

The Ultra-relativistic heavy-ion collisions provide a unique opportunity to study the properties of extremely hot and dense system. At large enough temperature and/or baryon density, statistical lattice QCD predicts a phase transition from hadronic matter to a new state of matter: a deconfined quarks and gluons plasma. Among the proposed signatures of the plasma, the enhancement of strangeness production is studied in the NA50 experiment.

A strong enhancement of strange particle production, as compared to the yield expected from hadronic gas, has been predicted if QGP formed. In NA50 experiment Pb–Pb collisions at 158 GeV/c per nucleon incident momentum at CERN/SPS, ϕ meson production is measured through dimuon channels and compare it to the ω meson yields.

In this thesis ϕ meson study is based on the data collected in 2000 runs. Compared to previous measurements from 1996 and 1998, this one benefits from improvements in the experimental setup, in particular concerning the measurement of minimum bias spectrum used to determine J/ψ , ϕ , ω and ρ multiplicities. The results of ϕ/ω ratios are presented, as a function of transverse mass and transverse energy. The present study confirms that ϕ/ω ratio does not depend on M_T , but increases with the collision centrality, by a factor about 2. The effective temperature analysis shows that $T_\phi \approx T_\omega$ at the order of 220 MeV. The multiplicity of ω per participant nucleon does not exhibit any N_{part} dependence, while ϕ multiplicity per participant nucleon increases with N_{part} .

Finally, the comparison of the ϕ central multiplicity in Pb-Pb system between NA50 and NA49 is made with updated $BR_{\mu\mu}$ constant, also the comparison of the cross section measurement between Pb-Pb system and lighter systems is done. The evolution of production in J/ψ mass dominated region for the most central collisions is also considered by comparing to the minimum bias spectrum.

Contents

Preface	i
Acknowledgments	iii
Abstract	iv
List of Figures	ix
List of Tables	xv
1 Introduction	1
1.1 The production of the Quark-Gluon Plasma	1
1.1.1 Where to find the QGP and how to create it	1
1.1.2 The stopping power and transparency region	2
1.1.3 Evolution of the system	4
1.2 The signatures of the Quark-Gluon Plasma	6
1.2.1 The J/ψ suppression	6
1.2.2 Signature of direct photons	7
1.2.3 Dilepton signature	8
1.3 Strangeness production	11
1.3.1 Thermal models	12
1.3.2 Some applications and strangeness saturation at 40 GeV per nucleon	14
1.3.3 Strangeness saturation	18
1.3.4 Multiple strange baryons	19
1.4 The ϕ production	20
1.4.1 Strangeness saturation factor and ϕ/ω ratio	21
1.4.2 Studies as a function of $p_T^{\mu\mu}$ or $M_T^{\mu\mu}$?	22
1.4.3 ϕ/ω or $\phi/(\rho + \omega)$?	22

1.4.4	Effective temperature	24
1.4.5	Experimental results of ϕ yield	24
1.5	Future searches	25
2	Experimental apparatus	27
2.1	Beam detectors	28
2.1.1	BH detector	28
2.1.2	Interaction detectors	28
2.1.3	Anti-halo detectors	29
2.2	The target region	29
2.3	Detectors for the centrality measurements	29
2.3.1	The multiplicity detector	30
2.3.2	The electromagnetic calorimeter	30
2.3.3	The Zero Degree Calorimeter	31
2.4	The Muon spectrometer	33
2.4.1	Absorbers	33
2.4.2	Scintillating hodoscopes	35
2.4.3	Multiwire proportional chambers	35
2.4.4	The Magnet	36
2.5	The trigger system	37
2.6	The data acquisition system and the reconstruction of tracks	39
2.7	Experimental improvements for 2000 runs	39
3	Data Selection and Analysis Treatment	41
3.1	The image cut	42
3.2	The Pileup cut	42
3.3	The target identification (<i>NOCIBI</i> and <i>NOCIMD</i>)	43
3.4	P^*D_{targ} cut on tracks	44
3.5	The Minimum bias spectra analysis	46
3.6	Study of E_T as a function of E_{ZDC}	46
3.7	Consistency of minimum bias analyses for dimuons	51
3.8	Determination of efficiency corrections	56
3.9	The prescaling of the minimum bias	61
3.10	Background subtraction	62
3.11	The centrality variables of the collision system	63
3.11.1	Determination of N_{part} and N_{coll}	64

3.11.2	Equivalent variables of centrality measurement	68
3.11.3	Centrality selection: E_T or E_{ZDC} ?	69
3.12	Application to J/ψ analysis	73
3.12.1	The fit to the mass spectra	74
3.12.2	J/ψ minimum bias behavior	75
4	Monte-Carlo Simulation	77
4.1	The physical generation of DIMUJET	77
4.2	The generation function	78
4.2.1	Generation on mass distribution	78
4.2.2	Generation on rapidity distribution	79
4.2.3	Generation on transverse mass distribution	79
4.2.4	Generation on $\cos \Theta_{CS}$ and φ_{CS} distribution	80
4.3	Accepted dimuon distributions	81
4.4	The acceptances in M_T slices	81
4.4.1	The acceptance as a function of M_T	81
4.4.2	The acceptance comparison to NA38 setup	84
4.5	Decomposition of the mass spectra	84
5	Experimental Results	91
5.1	The results $(\phi/\omega)_{\mu\mu}$	91
5.1.1	The uncertainties of the results $(\phi/\omega)_{\mu\mu}$	92
5.1.2	Evolution of $(\phi/\omega)_{\mu\mu}$ as a function of M_T	93
5.1.3	Evolution of $(\phi/\omega)_{\mu\mu}$ as a function of E_T	94
5.2	Cross section of σ^ϕ and σ^ω	95
5.2.1	Determination of σ^ϕ and σ^ω	95
5.2.2	The efficiency determination	96
5.2.3	The uncertainties of σ^ϕ and σ^ω	97
5.2.4	The σ^ϕ and σ^ω values in all E_T domain	98
5.3	The Effective temperature of ω and ϕ	98
5.3.1	Determine the M_T abscissa	98
5.3.2	Effective temperature as a function of centrality	99
5.4	The multiplicity measurement	100
5.4.1	The multiplicity definition	100
5.4.2	The Multiplicities of ω , ϕ as a function of N_{part}	102

6	Results Discussion	109
6.1	Comparison of other ϕ central multiplicity determinations in NA50 and NA49	109
6.2	Comparison with lighter systems	112
6.3	T slope of ϕ in Pb–Pb	114
6.4	Incomplete saturation of strangeness	116
7	Conclusions	119
	References	122

List of Figures

1.1	Diagram of the temperature <i>versus</i> baryonic density.	2
1.2	Diagram of the heavy ion collision.	4
1.3	Space-time diagram of the heavy ion collision according to Bjorken model.	5
1.4	Ratio $J/\psi/DY$ as a function of transverse energy of NA50 experiment in Pb-Pb collisions at 158 A GeV/c from 1996, 1996 with minimum bias and 1998 with minimum bias results.	7
1.5	WA80 direct photons in central $S + Au$ collisions at 200 A GeV.	8
1.6	WA98 direct photons in central Pb-Pb collisions at 158 GeV/c.	8
1.7	Dielectron invariant mass spectrum measured by CERES experiment in central Pb-Au collision at 158 A GeV, compared with expected contributions from hadronic decays.	9
1.8	The same results as in Figure 1.7, but compared with the contribution from ρ decays with and without in the dense medium effects.	9
1.9	Dimuons mass spectra for low and high E_T bins in Pb-Pb collision, displaying the various contributions considered in the fit and showing the increase of the $D\bar{D}$ like component (blue lines).	10
1.10	Evolution of measured/expected $D\bar{D}$ like component as a function of the number of participant nucleons, from protons to ions induced collisions, see [21] in detail.	10
1.11	The lowest-order Feynman diagrams for the production of $s\bar{s}$ by gluon fusion and quark pair fusion.	11
1.12	Schematic illustration of the energy levels inside a multiquark bag with two or three flavours.	12
1.13	Comparison between thermal model predictions and experimental particle ratios for Pb-Pb collisions at 158 GeV/nucleon. The thermal model calculations are obtained with $T = 170$ MeV and $\mu_B = 255$ MeV.	14

1.14	Wroblewski factor λ_S determined within the statistical model in several elementary [42, 43] and heavy ion collisions [44, 45] as a function of (nucleon-nucleon) centre-of-mass energy. Unlike all other points, the RHIC value has been obtained by using mid-rapidity hadron yields.	15
1.15	The dependence of the $\langle K^+ \rangle / \langle \pi^+ \rangle$ (left) and E_S (right) ratios on the collision energy for central A–A collisions (closed symbols) and inelastic p–p interactions (open symbols). The predictions of SMES for the E_S ratio are shown by a line. Different line styles indicate predictions in the energy domains in which confined matter (dashed line), mixed phase (dashed–dotted line) and deconfined matter (dotted line) are created at the early stage of the collisions (Where $F = (\sqrt{s_{NN}} - 2m_N)^{3/4} / \sqrt{s_{NN}}^{1/4}$).	16
1.16	The energy dependence of the inverse slope parameter T^* for K^+ mesons produced at mid-rapidity in central Pb+Pb (Au+Au) collisions at AGS (triangles), SPS (squares) and RHIC (circles) energies.	17
1.17	Contributions to the Wroblewski factor from strange baryons, strange mesons and hidden strange particles. Full line is a sum of all these contributions.	19
1.18	The multiple strange baryon production in Pb-Pb collisions at 158 A GeV compared to the corresponding yields in proton induced collisions as measured by NA57/WA97 experiment.	20
1.19	The various analysis methods : (a) a fit of the experimental invariant mass spectrum with simulated components taking into account smearing and acceptance effects, (b) a fit with physical components of a mass invariant spectrum corrected for smearing and acceptance. In both cases the same simulation program is used.	23
1.20	Phase diagram of strongly interacting matter in the temperature T and baryonic chemical potential μ_B . The points indicate $T - \mu_B$ values extracted from analysis of hadron multiplicities in central nucleus–nucleus collisions.	26
2.1	The NA50 experimental apparatus in the configuration used for the study of Pb–Pb collisions.	27
2.2	The layout of the active target (in 2000 data runs, only 1 sub-target located at position 4) region.	30
2.3	A schematic view of the NA50 apparatus in target region.	31
2.4	The multiplicity detector planes MD1 and MD2.	32
2.5	The zero degree calorimeter	32
2.6	The muon spectrometer	34

2.7	The absorber	34
2.8	A schematic view of the scintillating hodoscopes	35
2.9	The Multiwire proportional chambers PC1 to PC8.	36
2.10	The magnet and the shape of magnetic field.	37
2.11	The schematic view of the reconstruction of tracks.	39
3.1	<i>Pile-up</i> (left) and <i>NPARAS</i> (right) cut effects on minimum bias E_T spectrum.	43
3.2	<i>NICALO</i> cut influence on minimum bias (BH) and Dimuon trigger events in $E_T - E_{ZDC}$ plane.	44
3.3	A comparison of the E_T spectra with <i>NOCIBI</i> and <i>NOCIMD</i> cuts. Top plots show the spectra obtained using BH trigger, whereas the bottom plots are the spectra obtained using dimuon trigger.	45
3.4	Definitions of P^*Dtarg , <i>DMAG</i> and <i>DPHI</i> variables.	46
3.5	Minimum bias BH Trigger E_T spectra for four data taking periods.	47
3.6	Minimum bias ZDC Trigger (left) and Dimuon Trigger (right) E_T spectra (any dimuons) for the data part 2	47
3.7	Ratios of E_T spectra (BH trigger) obtained from different data taking periods: Ratios of Part1(left), Part3(middle) and Part4(right) to Part2	48
3.8	Ratios of E_T spectra (ZDC trigger) obtained from different data taking periods: Ratios of Part1(left), Part3(middle) and Part4(right) to Part2	48
3.9	E_T - E_{ZDC} correlation for Dimuon trigger (left) and for BH trigger (right) with minimal event level ≥ 1	49
3.10	The illustration of the transformation procedure from E_T - E_{ZDC} plane (left) to E'_T - E'_{ZDC} plane (right).	49
3.11	Left: The dependences on E'_T of the mean and the sigma of E'_{ZDC} spectrum for BH and Dimuon trigger of Low and High intensity runs separately. Right: A typical distribution of E'_{ZDC}	50
3.12	A dependence of $\langle E_T \rangle$ and σ_{E_T} on E_{ZDC} (minimum bias BH trigger) for low and high intensity runs.	51
3.13	E_T - E_{ZDC} correlation after <i>Banana</i> cut, left Dimuon Trigger, right BH Trigger.	52
3.14	E_T - E_{ZDC} correlation for 4 different <i>Banana</i> cuts.	53
3.15	The yields of like-sign, opposite-sign and signal dimuon pairs as a function of E_T for four different <i>Banana</i> cuts (part 1,2,4 data).	54
3.16	The yields of like-sign, opposite-sign and signal dimuon pairs as a function of E_T , after <i>ZVertex</i> and <i>P*Dtarg</i> cuts (part 1,2,4 data).	55

3.17	The yields of like-sign, opposite-sign and signal dimuon pairs as a function of E_T for four different <i>Banana</i> cuts (ONLY part 2,4 data).	56
3.18	The yields of like-sign, opposite-sign and signal dimuon pairs as a function of E_T , after <i>ZVertex</i> and <i>P*Dtarg</i> cuts (ONLY part 2,4 data).	57
3.19	Raw yields of J/ψ , ϕ and ω (BH trigger minimum bias) as a function of E_T (GeV).	57
3.20	Left: the fraction of the raw J/ψ signal remaining after various cuts as a function of E_T ; Right: the fraction of minimum bias remaining after various cuts as a function of E_T	59
3.21	J/ψ transverse energy spectrum, before and after <i>PILEUP</i> and <i>NPARAS</i> cuts.	61
3.22	The dimuon mass spectrum rejected by the <i>NPARAS</i> cut and the remaining dimuons.	61
3.23	Ratio of J/ψ to Minimum bias efficiency as a function of E_T for different cuts.	62
3.24	BH scalers of Only one BH blade and the BH blade logical signal prescaling versus run number.	63
3.25	The ratio of Luminosity/BH and Luminosity/ZDC versus run number. . .	63
3.26	The invariant mass spectra of dimuons from the same events and the combinatorial background spectra (Eq.3.3) in low mass (<i>left</i>) and high mass (<i>right</i>) domains.	64
3.27	A schematic diagram of geometry of nucleus-nucleus collision.	65
3.28	Wood-Saxon distribution with $\rho_0=0.169 \text{ fm}^{-3}$, $r_0=6.62 \text{ fm}$, $C=0.549 \text{ fm}$, normalized	66
3.29	(a) Fit to the Minimum Bias E_T spectrum; (b) Comparison with the E_T spectrum obtained within Wounded Nucleon Model.	69
3.30	The cross section $d\sigma/db$ as a function of the impact parameter b calculated within the Glauber MC (unnormalized).	70
3.31	E_T - b (column 1), E_{ZDC} - b (column 2) and E_T - E_{ZDC} (column 3) correlations for σ_{E_T} and $\sigma_{E_{ZDC}}$ resolutions increasing from top to bottom.	72
3.32	The dependence of $\langle E_T \rangle$ on b (left) and $\langle E_{ZDC} \rangle$ on b (right) for normal and improved resolutions.	73
3.33	Fitted dimuon invariant mass spectrum for Pb–Pb collisions at 158 A GeV (2000 data).	75

3.34	Left: E_T spectrum of J/ψ events; Right: unnormalized J/ψ multiplicity per number of collisions versus E_T for Pb–Pb collisions at 158 A GeV (2000 data).	76
4.1	The definitions of Collins-Soper angles in the Collins-Soper reference frame.	80
4.2	Dimuon invariant mass, rapidity, transverse mass and $\cos \Theta_{CS}$ distributions for Generated (top plots) and reconstructed (bottom plots) events. The vertical scale are in arbitrary units.	81
4.3	Reconstructed mass spectra for ϕ , ρ , ω and continuum (all M_T).	82
4.4	Left: the acceptance factor for ω and ϕ as a function of M_T (GeV/ c^2); Right: A comparison of the ratio of acceptance factors for ω and ϕ simulated for different data taking periods.	83
4.5	The ω and ϕ acceptance factors versus M_T (GeV/ c^2) obtained when changing the magnetic field, the iron absorber and both from NA50 setup.	85
4.6	The ratio of ϕ acceptance factors calculated before and after subsequent set-up modifications.	85
4.7	The ratios of acceptance factors for ω and ϕ versus M_T calculated including various set-up modifications in Figure 4.5.	85
4.8	The dependence of the width of the invariant masses of ω and ϕ on M_T . The integrated Gaussian fit with 50 MeV/ c^2 bin was used.	87
4.9	The fits to the invariant mass spectra for various M_T intervals for $E_T > 10$ GeV.	88
4.10	The fits to the invariant mass spectra for various E_T intervals in M_T domain $1.5 \leq M_T \leq 3.2$ GeV/ c^2	89
4.11	Fits to the invariant mass spectra in various E_T and M_T intervals.	90
5.1	The ratio $(\phi/\omega)_{\mu\mu}$ as a function of M_T in different E_T bins.	93
5.2	The ratio $(\phi/\omega)_{\mu\mu}$ as a function of M_T in different E_T bins.	94
5.3	The ratio $(\phi/\omega)_{\mu\mu}$ as a function of E_T in various M_T intervals and in all M_T interval.	95
5.4	The M_T spectra of ϕ meson for various E_T intervals. The “thermal” fits to the spectra with $M_T^{3/2} \exp(-M_T/T)$ are indicating by solid lines.	100
5.5	The effective temperature of ϕ and ω versus E_T with the horizontal line fits (top) and with the linear fits (bottom).	101
5.6	The multiplicity of ϕ as a function of N_{part} for various M_T intervals.	104
5.7	The multiplicity of ω as a function of N_{part} for various M_T intervals.	105

5.8	The multiplicity of ϕ per participant nucleon as a function of N_{part} for various M_T intervals.	106
5.9	The multiplicity of ω per participant nucleon as a function of N_{part} for various M_T intervals.	107
5.10	The multiplicities and the multiplicities per participant for ϕ and ω as a function of N_{part} in the interval $1.5 \leq M_T \leq 3.2$ GeV/ c^2	108
6.1	A comparison of the M_T spectra of ϕ meson in central Pb–Pb collisions at 158 A GeV measured by NA49 and NA50 (old results).	110
6.2	A comparison of the M_T spectra of ϕ meson as in figure 6.1 measured by NA49 and by NA50 obtained in this thesis.	111
6.3	A comparison of the M_T spectra of ϕ meson as in figure 6.1 measured by NA49 and by NA50 in various analysis (early 1996 results, 1996, and 2000).	112
6.4	A comparison of the M_T spectra of ϕ meson as in figure 6.1 measured by NA49 and various analysis by NA50 considering the electrons branching ratio.	113
6.5	The dependence of ϕ and ω cross section for $M_T > 1.5$ GeV/ c^2 as a function of the product $A \times B$ of nuclear mass numbers of the colliding nuclei.	114
6.6	The T slopes of ϕ and $\rho + \omega$ versus $A \times B$ for different systems.	115
6.7	The T slopes versus particle masses measured by several experiments in Pb–Pb collisions at 158 GeV/ c at SPS.	115
6.8	Blast wave fits to the transverse spectra measured by NA49. Pions and deuterons were excluded from the fits. (for 158 AGeV)	116
6.9	T slopes of ϕ versus \sqrt{s} [94]	117
6.10	The ratio of ϕ/K^- versus \sqrt{s} [94]	117
6.11	Left panel: Comparison of γ_S extracted from mid-rapidity NA49 data with the results of earlier analysis of NA49 4π -yields; Right panel: γ_S observed in Au+Au collisions as extracted from PHENIX data.	118

List of Tables

1.1	ϕ meson properties (Particle Data Booklet 2002)	21
3.1	Corrections applied to luminosity, dimuons or minimum bias, in order to take into account the signal rejection by background cuts.	58
3.2	The values of equivalent relationship for E_T , N_{part} , N_{coll} and b and centrality selection (%) in 9 E_T intervals.	70
4.1	Characteristic variable domains for components.	79
4.2	Acceptance factors for ϕ and ω in different M_T intervals and statistical errors.	83
5.1	Relative errors (%) for acceptance and fit method	92
5.2	The values for $(\phi/\omega)_{\mu\mu}$ per M_T and E_T interval.	96
5.3	Values used for the cross section in Pb+Pb collisions.	97
5.4	The dimuon cross section values of σ^ϕ and σ^ω for Pb-Pb per M_T bins (for $-0.5 \leq \cos \Theta_{CS} \leq 0.5$ and $0 \leq y^* \leq 1$)	98
5.5	The calculated values of the M_T abscissa.	99
5.6	Effective temperature values as a function of E_T	99
5.7	The multiplicity values of ϕ and ω (for $-0.5 \leq \cos \Theta_{CS} \leq 0.5$ and $0 \leq y \leq 1$) .	103

Chapter 1

Introduction

1.1 The production of the Quark-Gluon Plasma

Statistical lattice Quantum Chromo-Dynamics (QCD) calculations predict that a phase transition from ordinary hadronic matter to a new state of matter should occur when the nuclear matter is compressed and heated to a sufficiently high energy density and temperature [1, 2]. The quarks and gluons confined in hadrons are liberated due to the screening effect on their potentials, and they are able to move freely in this deconfined state of matter. This deconfined state of matter is named Quark-Gluon Plasma (QGP). QCD lattice calculation predicts such a phase transition with critical values of the temperature from 150 MeV to 180 MeV and the energy density $\sim 1 \text{ GeV/fm}^3$ [3].

1.1.1 Where to find the QGP and how to create it

Following the “Big Bang” model, it is believed [4, 5] that the early Universe was the first case in this state of quark-gluon plasma, the hadronization having occurred later, as the consequence of its expansion and cooling, about $10 \mu\text{s}$ after the “Big Bang” origin. It is possible that QGP exists inside of the neutron stars [4, 5], whose core is believed to have a density higher than the critical density for the phase transition. In order to experimentally study the phase transition of the quark-gluon plasma, we need to achieve very high energy density and/or temperature in the lab. It is also important to have a large interaction volume in order to approach the thermodynamic limit of the new phase. In the laboratory, QGP can be obtained, as a transient state, by means of very high energy heavy ion collisions.

Ultra-relativistic heavy-ion collisions provide a unique opportunity to study the properties of the matter in the extreme conditions of temperature and/or density. Fixed target

experiments have been performed for many years, by using high energy heavy ion beams, in order to attempt to reach the critical temperature of the phase transition (see figure 1.1).

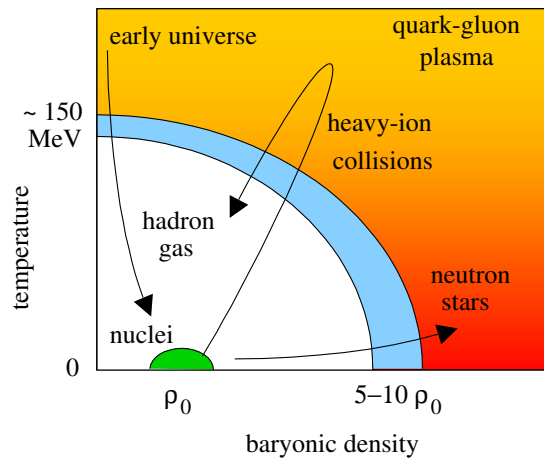


Figure 1.1: Diagram of the temperature *versus* baryonic density.

1.1.2 The stopping power and transparency region

At very high energy the colliding ultra-relativistic ions look like squeezed in the longitudinal direction due to the Lorentz contraction, when they are seen in their center-of-mass reference frame, with their thickness about 1 fm ($1 \text{ fm} = 10^{-15} \text{ m}$) (see figure 1.2).

The nuclear stopping power indicates that the colliding nuclear matter loses a substantial fraction of its energy in the collision process. Since the energy lost by the colliding nuclear matter is deposited in the vicinity of the center of mass with the production of hadrons, high-energy nucleus-nucleus collisions provide an excellent tool to produce a very high energy density region. As estimated by Bjorken [6], the energy density can be so high that these reactions might be utilized to explore the existence of QGP. Qualitatively two different energy regions are defined as the “baryon-free quark-gluon plasma” region (or the transparent region) and the “baryon-rich quark-gluon plasma” region (or the stopping region). For a collision at an energy of a few GeV per nucleon in the center of mass system, like AGS, the nuclear stopping power determines whether the colliding baryons will be stopped in the center of mass system and pile up to form a quark-gluon plasma with large baryon density, which is in the stopping region. While in the transparent region or “baryon-free quark-gluon plasma” region, the nuclear stopping power determines whether

the projectile baryons and the target baryons will recede away from the center of mass without being completely stopped, leaving behind QGP with very little even no baryon contents. For SPS, the energy covers these two regions, for RHIC and LHC, the energy is very high up to the baryon-free quark-gluon plasma region (or the transparent region).

The Rapidity

In order to describe the kinematics of a collision, a kinematical variable of *Rapidity Variable* y for a particle is defined as :

$$y = \frac{1}{2} \ln \frac{E + p_z}{E - p_z} , \quad (1.1)$$

where E is the energy of the particle, p_z is the particle's longitudinal momentum along the beam axis. This variable is a dimensionless quantity. The advantage of this rapidity variable is that the dependency on the frame of references is very simple, i.e., the rapidity of the particle in one Lorentz frame of reference is related to the rapidity in another Lorentz frame of reference just by a additional constant. For instance, the relation between a particle in the laboratory frame of reference and in the center of mass frame of reference is given by $y^{CM} = y^{lab} - y^*$, where y^* is the rapidity of the center-of-mass in the laboratory frame.

In many experiments, it is only possible to measure the angle of the detected particles relative to the beam axis. In that case, it is convenient to utilize this information by the *pseudo-rapidity variable* η , to characterize the detected particles. The pseudo-rapidity is defined as

$$\eta = -\ln \left(\tan(\theta/2) \right) , \quad (1.2)$$

where θ is the angle between the particle's momentum and the beam axis. In the terms of the momentum, the pseudo-rapidity variable can be written as

$$\eta = \frac{1}{2} \ln \frac{|\mathbf{p}| + p_z}{|\mathbf{p}| - p_z} , \quad (1.3)$$

By comparing Equation 1.1 and 1.3, it is easy to see that the pseudo-rapidity variable coincides with the rapidity variable when the momentum is large, i.e. $|\mathbf{p}| \approx E$. For particles with $\beta \approx 1$, $\eta \approx y$, while for massless particles, $\eta = y$.

In the stopping region, the rapidity of all particles in center-of-mass frame y is zero. The baryon density in the central rapidity region is rather high. While for the transparent region, there are three rapidity domains: two regions for the fragmentation corresponding to incident ions of the target and the projectile, the rapidity distributions of the target

and the projectile fragmentation is large and moving fast, the number of baryons is almost intact and redistributed in the region for each. The remained is the rapidity region around $y^* = 0$, where it is excited and emitting particles during collisions, which is baryon-free.

1.1.3 Evolution of the system

According to the hydrodynamical Bjorken model [6], a space-time scenario, the two colliding ions are almost transparent to each other. After they crossing and departing with each other, they leave in-between a hot interaction region, where the system is thermally and chemically equilibrated. The target and projectile fragmentation regions are produced, connected by a region of central rapidity. These acquire the transverse momentum from the multiple collisions in between them. After the interaction the two disks of the target

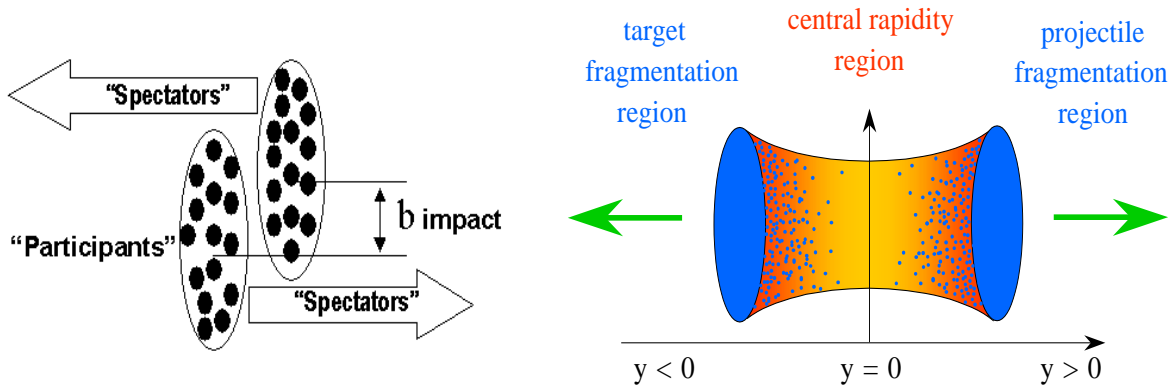


Figure 1.2: Diagram of the heavy ion collision.

and the projectile will continue to move in opposite directions with the speed $\approx c$, the region $y = 0$ in between them will expand cylindrically (see figure 1.2).

The space-time evolution of a collision at high energy is shown in figure 1.3. Since the energy deposited in the collision region around $z \sim 0$ is very high, sooner after the collision of the two nuclei at point $(z, t) = (0, 0)$, the energy density is sufficiently high to form QGP. In the first stage, nucleon-nucleon collisions introduce a redistribution of the original energy into other degrees of freedom, materializing into quarks and gluons after a short time. In a second stage, the dense system of quarks and gluons is formed, with thermal and chemical equilibration. Due to color deconfinement, quarks and gluons are free from each other. Then QGP will rapidly cool down via the expansion and the evaporation, undergoing a "mixed phase" in which the hadrons and the "blobs" of plasma would coexist. Finally it will completely condensate into a state of ordinary hadrons,

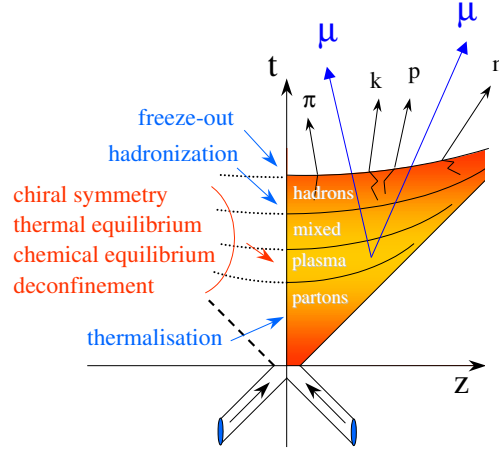


Figure 1.3: Space-time diagram of the heavy ion collision according to Bjorken model.

firstly interacting with each other and then freeze out. The final state reflects the complex evolution of the system, and the different observables carry informations of different aspects and resulting from different stages.

Thermodynamic variables The phase transition of the hot hadronic matter can be derived from the measurement of the energy density ϵ and the temperature T . A phase transition involving a large latent heat would manifest itself in a characteristic shape of T versus ϵ dependence: the T would firstly grow with ϵ , then remain constant while the additional energy goes into the latent heat, and finally grows again. Dileptons being decayed at the early stage, they carry with the original information of the system temperature. The space-time evolution of the system, particular in the freeze-out phase space, can be measured via identical particle interferometry (HBT). Furthermore, the multiplicity fluctuations could feedback the critical phenomena linked to a phase transition.

Chiral symmetry restoration In QGP, the quarks lose their effective mass which they carried when confined in a hadron, and recover back to their “bare mass”. In other words, with the quark masses very small or almost equal to zero, the QGP would be chiral symmetric. This would manifest itself in a change in the strangeness production (strangeness enhancement), and in changes of the hadron masses. The Mass, width and decays of the particles such as ρ and ϕ should experience sharp modifications.

Deconfinement As a sufficiently dense ordinary plasma can prevent the formation of the atoms by electromagnetic screening of nuclei from the electrons (the “Mott transition”), the color force between quarks would be screened in QGP. The heavy $c\bar{c}$ pairs,

like J/ψ or ψ' mesons, are produced only rarely, the processes can happen only in the initial instants of a nuclei collision. The c and \bar{c} quarks are prevented to form the bound states due to the color screening effect. Thus a suppression of J/ψ and ψ' in the central nuclear collisions is expected in a deconfinement phase.

1.2 The signatures of the Quark-Gluon Plasma

Evidences of the formation of the quark-gluon plasma are studied experimentally by looking at the modification of the fraction of produced particles :

1. The comparison between the results of the fraction of the particles measured in nucleus-nucleus, proton-proton and proton-nucleus collisions.
2. The comparison between the results obtained from the nucleus-nucleus collisions at the different energies.
3. Study the variation of the fraction of the particle yields in the nucleus-nucleus collisions as a function of the centrality.

Experimentally, one or several of these procedures are used for physical analysis.

1.2.1 The J/ψ suppression

The production and suppression of heavy quarkonia bound states, such as J/ψ , was proposed by Matsui and Satz in 1986 as an ideal signal of quark deconfinement [7].

In a very dense medium, the c and \bar{c} quarks do not feel the presence of each other, either due to the plasma preventing the $c\bar{c}$ from becoming a bound state (the color charges of quarks are screened because of the Debye screening effects), or alternatively due to the interactions between the dense hadronic matter and $c\bar{c}$ quarks, including the comovers.

The NA38 and NA50 experiments have presented results to interpret the J/ψ suppression as a signal of QGP formation [8, 9, 10], which was one of the most promising and attractive experimental results, and triggered many theoretical calculation to explain the J/ψ suppression in a dense hadron gas, within a non-QGP scenario, as due to the absorption and the re-scattering processes.

This anomalous J/ψ suppression pattern in the central Pb+Pb collisions at 158 AGeV/c [9, 10, 11] is one of the strongest evidences of the initial condition creation up to an extremely hot and dense state of matter at SPS, a state that can not be explained within the scenario of the normal nuclear matter. The J/ψ suppression results

(the ratio $J/\psi/DY$ with minimum bias from 1996 and 1998) are presented in the Figure 1.4, where in this figure the curve corresponding to the normal nuclear absorption.

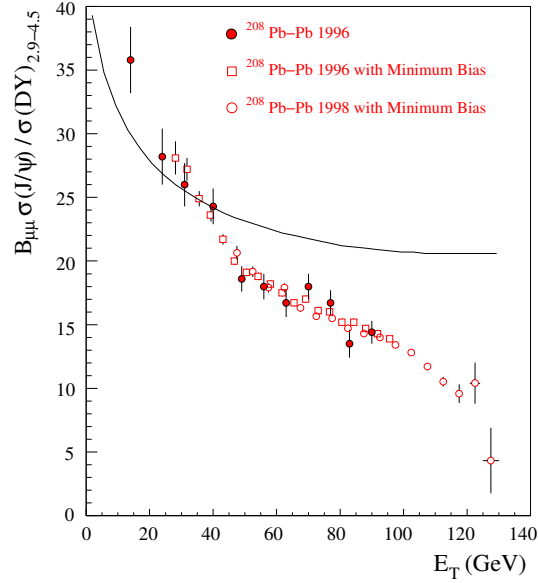


Figure 1.4: Ratio $J/\psi/DY$ as a function of transverse energy of NA50 experiment in Pb-Pb collisions at 158 A GeV/c from 1996, 1996 with minimum bias and 1998 with minimum bias results.

1.2.2 Signature of direct photons

Direct photons have been proposed as a promising signature for the QGP formation in relativistic heavy-ion collisions [12, 13]. WA98 and WA80 experiments have presented direct photons results in Pb+Pb and S+Au collisions [14].

The photons from high-energy hadronic and nucleus-nucleus collisions provide important information about fundamental aspects of the particles involved and their interactions. In particular, they probe the parton distributions in hadrons and nuclei. In relativistic heavy-ion collisions, they serve as a direct probe for all stages of the fireball since they leave the system without further interactions due to their large mean free path. Most important, the thermal radiation from the fireball might allow to extract information on the EOS of the matter produced in the collision. Hence, the direct photon production provides one of the most promising signatures for the QGP.

The extracted direct photon spectrum from WA98 shows a clear excess over the background for photon transverse momenta between 1.5 and 3.5 GeV/c (Figure 1.6)

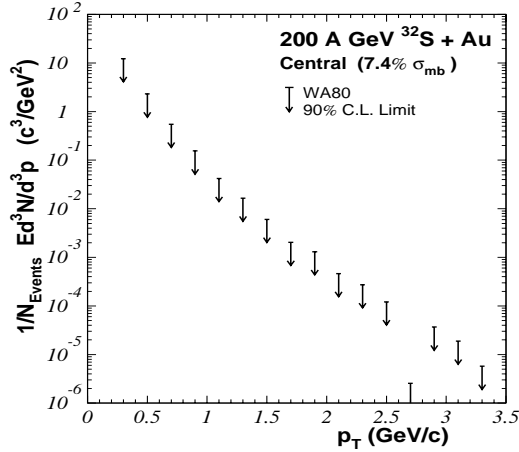


Figure 1.5: WA80 direct photons in central $S + Au$ collisions at 200 A GeV.

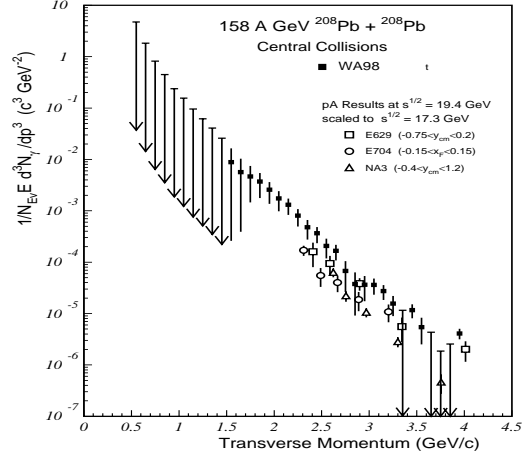


Figure 1.6: WA98 direct photons in central $Pb + Pb$ collisions at 158 GeV/c.

[14], whereas WA80 gave only an upper limit for direct photons in $S + Au$ collisions at 200 A GeV (Figure 1.5) [15]. In Figure 1.6, Data from pp reactions by E704 and from $p+C$ reactions by E629 and NA3 at $\sqrt{s} = 19.4$ GeV have been converted to the lower energy $\sqrt{s} = 17.3$ GeV assuming a scaling according to parameterized cross section $Ed^3\sigma_\gamma/dp^3 = f(x_T, \theta)/s^2$, where $x_T = 2p_T/\sqrt{s}$ and θ is the emission angle of the photon. They have been multiplied with the average number of binary nucleon-nucleon collisions in the central $Pb + Pb$ reactions. These scaled p -induced results are included in Figure 1.6 for comparison [16]. The present experimental results of direct photons can not infer about the existence of a QGP phase in central $Pb + Pb$ collisions at a beam energy of 158 A GeV. However, the data are consistent with a thermal source, either QGP or HHG, for photons with $p_T < 2.5$ GeV/c and with enhanced prompt photons for $p_T > 2.5$ GeV/c [17].

1.2.3 Dilepton signature

Dileptons are one of the direct electromagnetic probes when produced through virtual photons that do not interact strongly. Thermal dileptons, for example, can be produced in the quark-gluon plasma, through the annihilation processes :

$$q\bar{q} \rightarrow \gamma^* \rightarrow l^+l^- . \quad (1.4)$$

There is a contaminant by the continuum corresponding to the mass spectrum from

other contributions (Dalitz decays, *Drell-Yan* and $D\bar{D}$ processes), and eventual processes like $\pi\pi$ annihilation.

The CERES experiment has observed the yields of low mass dielectron pairs e^+e^- measured in p-A collisions [18], the results can be explained in a proper way by a expectable “cocktail” of hadronic decays. In Pb-Au collisions, the measured results have a excess yields [19], by a factor of 2.5, in the mass domain 0.2-0.7 GeV/ c^2 (Figure 1.7 [20]). The dependence with the dielectron transverse momentum [19] shows that the excess dileptons are concentrated at low p_T . This result can also be interpreted based on the changes of the properties of the vector mesons when they are produced in the dense matter, including changes of masses and decay widths. In particular, the chiral symmetry should be (partially) restored, near the phase transition. The life-time of ρ is short, this makes it to be a sensitive probe of the dense medium effects¹.

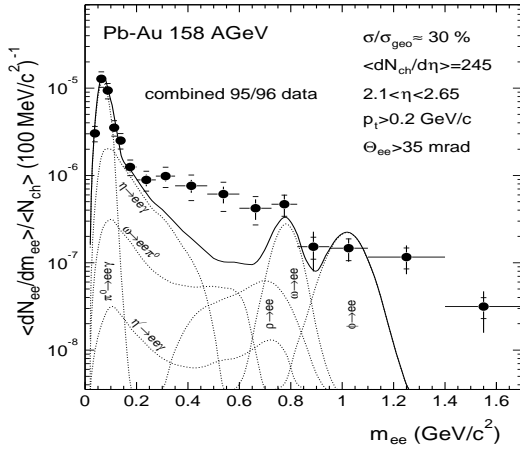


Figure 1.7: Dielectron invariant mass spectrum measured by CERES experiment in central Pb-Au collision at 158 A GeV, compared with expected contributions from hadronic decays.

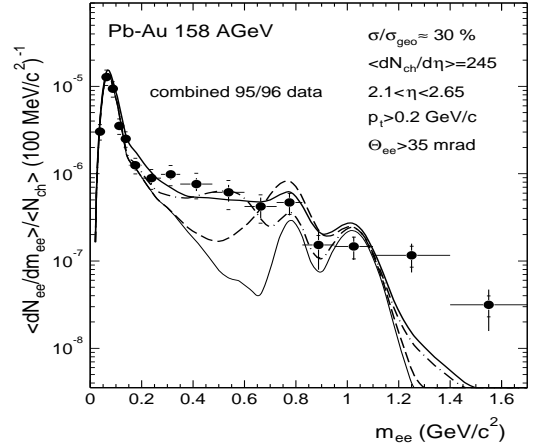


Figure 1.8: The same results as in Figure 1.7, but compared with the contribution from ρ decays with and without in the dense medium effects.

The NA50 experiment has observed an excess production of intermediate mass dileptons. Figure 1.9 displays two complete dimuon mass spectra, for peripheral and central

¹In Figure 1.8, Comparison of the experimental data to i) free hadron decays without ρ decays (thin solid line), ii) model calculations with a vacuum ρ spectral function (thick dashed line), iii) with dropping in-medium ρ -mass (thick dash-dotted line), iv) with a medium-modified ρ spectral function (thick solid line).

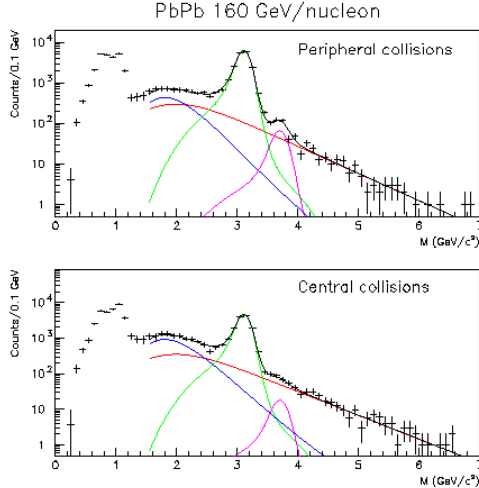


Figure 1.9: Dimuons mass spectra for low and high E_T bins in Pb-Pb collision, displaying the various contributions considered in the fit and showing the increase of the $D\bar{D}$ like component (blue lines).

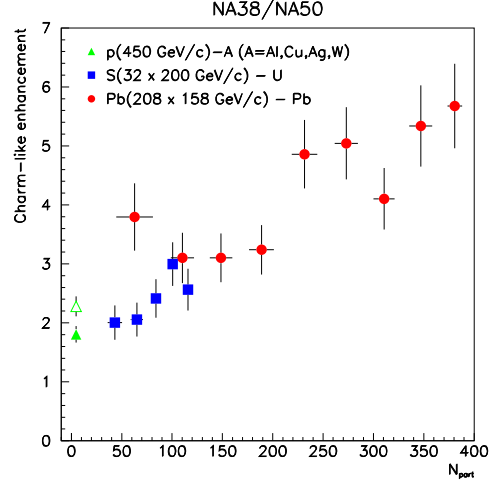


Figure 1.10: Evolution of measured/expected $D\bar{D}$ like component as a function of the number of participant nucleons, from protons to ions induced collisions, see [21] in detail.

collisions in the Pb-Pb system. The various components considered in the fit are shown. The Drell–Yan contribution is determined by the high mass dimuon yield. The background component is mostly fixed by the muon pair of the same signs. J/ψ and ψ' resonances contribute significantly only in their restricted mass domains, so in the intermediate mass range ($1.5 \leq m \leq 2.5 \text{ GeV}/c^2$) only the $D\bar{D}$ component is significantly free.

$D\bar{D}$ and Drell–Yan are hard processes, their cross section scales as the number of nucleon-nucleon collisions. Their ratio should be constant, irrespective of the system considered. This picture is verified for the Drell–Yan, whereas the $D\bar{D}$ component has to be increased relatively to Drell–Yan in order to reproduce the continuum production in the mass range 1.5-2.5 GeV/c^2 , and this excess is increasing with the centrality (figure 1.9). Picture 1.10 shows the evolution as a function of the number of participant nucleons [21].

The kinematical distribution of the excess is consistent with $D\bar{D}$ production as expected from the PYTHIA code, suggesting that this excess is due to an open charm enhancement. This will be checked by the NA60 experiment. Alternative explanations [21, 22] could be rescattering of D mesons in nuclear matter, or production of thermal dileptons. It is necessary to mention that concerning continuum determination in the intermediate mass region and an observation of enhancement of dilepton production for most central collisions, some doubts have been raised[23] on the need to improve the

precision on the eventual bias on the background determination².

1.3 Strangeness production

In pp collisions, strangeness production is suppressed by OZI rule[24], this is often referred also as the “canonical suppression”. As proposed by J.Rafelski[25] in nucleus-nucleus collisions, the occurrence of QGP should lead (due to the increase of gluon number, relative lower s quark mass thanks to the chiral symmetry, and disappearance in the QGP of the need for additional quarks, favoring the strangeness production and the occurrence of equilibrium between u , d and s quarks) to the enhancement of strangeness production, with respect to the canonically suppressed production in pp collisions.

In quark-gluon plasma, the threshold for the production of $s\bar{s}$ pairs is very low, since the s quark bare mass is only 75 to 170 MeV [26] and so to produce a pair it is only necessary a maximum of $2m_s \approx 300$ MeV. On the other hand, the gluon fusion $gg \rightarrow s\bar{s}$, quark fusion $q\bar{q} \rightarrow s\bar{s}$ and gluon decay $g \rightarrow s\bar{s}$ processes (see Figure 1.11) in the plasma are another factor that favors the strangeness production. The gluon fusion $gg \rightarrow s\bar{s}$ process is responsible for about 90% of the $s\bar{s}$ pairs produced. Due to Pauli Exclusion

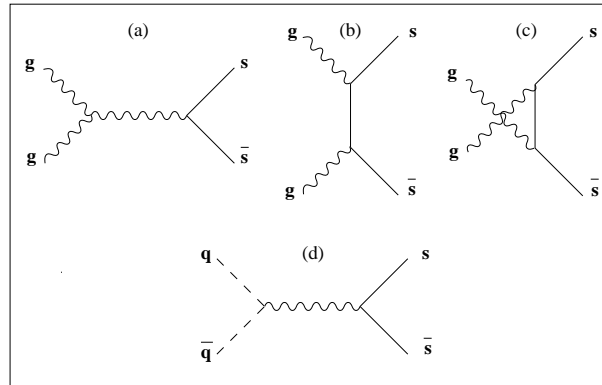


Figure 1.11: The lowest-order Feynman diagrams for the production of $s\bar{s}$ by gluon fusion and quark pair fusion.

Rule, the production of $s\bar{s}$ pairs would be produced in a similar way than u, d quark pairs if the lowest available u, d quarks energy levels are larger than $2M_s$ (see figure 1.12). Finally, the time needed for the system to reach the thermal and chemical equilibrium if

²This is due to the short life time and expected low multiplicity of D -mesons which cause the small experimental signal originating from D decays to be hidden in the large combinatorial background [23].

QGP formed is 20 to 30 times shorter (and comparable to the time needed for the two nuclei to transverse each other at this energy) than that needed for an hadron gas [27]. All these characteristics would favour the strangeness production.

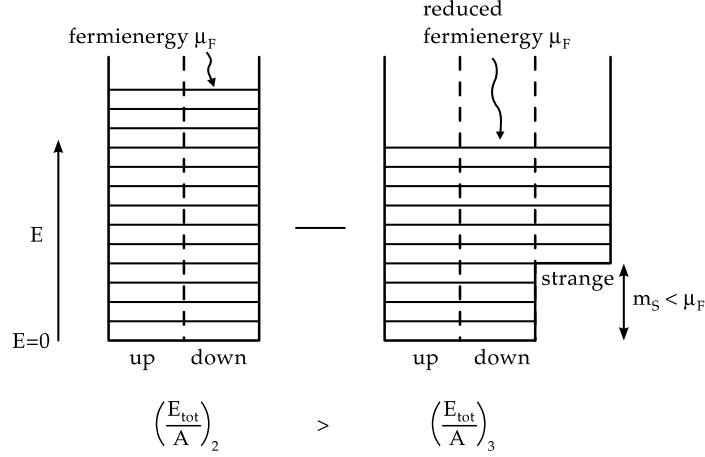


Figure 1.12: Schematic illustration of the energy levels inside a multi-quark bag with two or three flavours.

A. Shor[28] has applied this view to the ϕ production, predicting a possible enhancement of the ratio ϕ/ω , up to a factor of about 20. Observed increase of the strangeness production was also interpreted as possible effect of the rescattering [29].

In the second half of the nineties, the global description of the hadronic production has been improved by the development of thermal models [30]. Nevertheless several interpretations remain.

1.3.1 Thermal models

A flat rapidity distribution is a simplified case for the description of the system, which has been used by Bjorken for deriving the energy density[6]. Even if this condition is not fulfilled, the abundances of particle species will follow statistical Boltzman distributions [31] if the longitudinal flow can be considered as a superposition of fireballs. Following [31], in thermal model the density n_i of particle i can be approximated by a Boltzman distribution,

$$n_i = g \int \frac{d^3p}{(2\pi)^3} e^{-(E_i - \mu_i)/T} = \frac{gm_i^2 T}{2\pi^2} K_2(m_i/T) e^{\mu_i/T},$$

where the index i refers to the type of hadrons, e.g., $i = \pi^+, K^+, \dots$ etc, g is the spin-isospin-degeneracy factor for the particle species.

For small systems with few elements, the thermodynamical canonical description is necessary, where quantum numbers (like baryonic number, electric charge, strangeness number) are conserved exactly and on an event by event basis. Typically this description has to be used for pp collisions. In nucleus-nucleus collisions, the high number of elements leads to consider a conservation on the average, through chemical potentials or chemical factors, in a grand canonical description. The change from canonical to grand canonical has been interpreted as the origin of the strangeness enhancement predicted and observed in A–A collisions [32].

Another additional question could even be to consider a local equilibrium, a micro-canonical description. There is a consensus for considering complete production yields in order to avoid local (y or M_T) biases. Nevertheless a global equilibration and existence of an important correlation between all rapidity domains are not obvious. Important conditions like the baryonic density, and then the chemical potential, and more generally all the observable (M_T distribution, freeze-out radius) vary with y , raising doubts about the validity of a universal condition. The influence of baryon density, in a mechanism favouring for instance Λ and then K^+ production, should be more relevant in a unit rapidity than that in average. For heavy particles, rapidity distributions are influenced by energy conservation, and it is not clear how a thermal model could account for that. U.Heinz[37] indicates arguments against the global thermal state, but finally concludes that mainly because of differences in rapidity distributions and flow effect, a full phase space is required.

Similarly to questions about the homogeneity of conditions along rapidity axis, one can wonder about the effects of time evolution and introduce a continuous emission of particles [38].

For years, since pioneering work of Hagedorn [39], and the observation of a transverse energy scaling [40] the fact that a thermal description can be successful in pp collisions had often been the source of wondering, since the equilibrium is not supposed to be reached in pp collisions. Actually the mystery can be solved by considering that the population of the various final states available for the important number of collisions studied (which is the high number apparently missing) has to be statistically populated, according to energy and charge conservation. As a consequence, the microscopical model lead to statistical population. Beside of this statistical sharing, reinteractions in each A–A collisions[37] lead to a local equilibrium: a chemical one (particle species) thanks to inelastic collisions, and a (kinetic) thermal one thanks to the total cross section of collisions.

Fluctuations (once the fluctuations due to N–N collisions between the wounded nucleons are removed) are also interesting as a test of thermalization.

1.3.2 Some applications and strangeness saturation at 40 GeV per nucleon

Figure 1.13 displays a striking consistency between experimental results and a thermal fit [36]. It is noteworthy that here strangeness is assumed to be saturated.

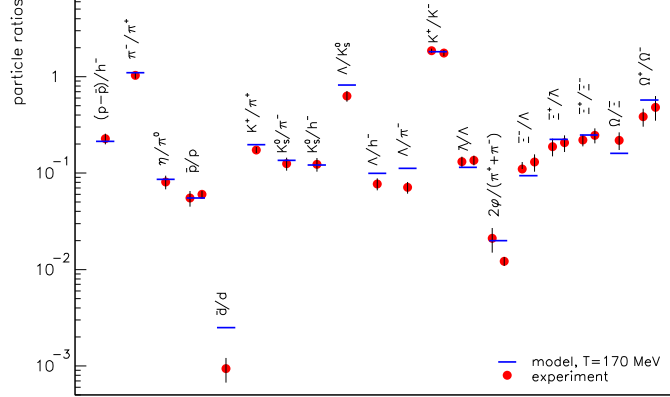


Figure 1.13: Comparison between thermal model predictions and experimental particle ratios for Pb–Pb collisions at 158 GeV/nucleon. The thermal model calculations are obtained with $T = 170$ MeV and $\mu_B = 255$ MeV.

Such fits to the populations lead to thermal parameters, whose evolutions are particularly important for the understanding of the characteristics of the matter created in the collisions. Figure 1.14 presents the Wroblewski factor[41] at the primary particles level, where $\lambda_s = 2s\bar{s}/(u\bar{u} + d\bar{d})$. This factor presents a maximum around 40 GeV/nucleon.

The eventuality of this peculiar pattern has been the origin of a ion beam energy scan at CERN performed recently to study the transition region [46].

The data on A–A collisions show that there is a significant change in the energy dependence of strangeness yields which is located between the top AGS and SPS energies. Based on the statistical approach it was speculated that this change is related to the onset of deconfinement at the early stage of the A–A collisions. Following this physical idea, a quantitative model has been developed, the Statistical Model of the Early Stage (SMES) [47]. It assumes that the early stage matter is created according to the principle of

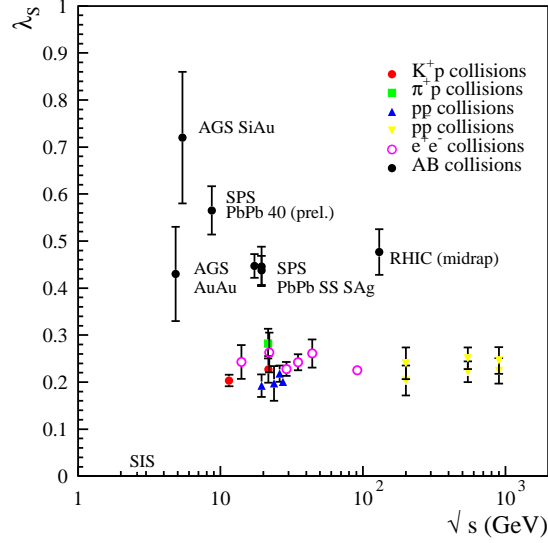


Figure 1.14: Wroblewski factor λ_S determined within the statistical model in several elementary [42, 43] and heavy ion collisions [44, 45] as a function of (nucleon-nucleon) centre-of-mass energy. Unlike all other points, the RHIC value has been obtained by using mid-rapidity hadron yields.

maximum entropy. Depending on the collision energy, the matter is in the confined phase ($E < 30$ A·GeV), mixed phase ($30 < E < 60$ A·GeV) or deconfined phase ($E > 60$ A·GeV). The phase transition is assumed to be of the first order.

Within SMES model at low collision energies, when confined matter is produced, the strangeness to entropy ratio steeply increases with the collision energy, due to the low temperature at the early stage ($T < T_C$) and the high mass of the carriers of strangeness ($m_S \cong 500$ MeV, the kaon mass). When the transition to deconfined matter is crossed ($T > T_C$), the mass of the strangeness carriers is significantly reduced ($m_S \cong 170$ MeV, the strange quark mass). Due to the low mass ($m_S < T$), the strangeness yield becomes (approximately) proportional to the entropy, and the strangeness to entropy (or pion³) ratio is independent of energy. This leads to a change of shape from the larger value for confined matter to the value for deconfined matter at T_C . Thus, within the SMES,

³The major particles produced in high energy interactions are pions. Pions carry basic information on entropy created in the collisions.

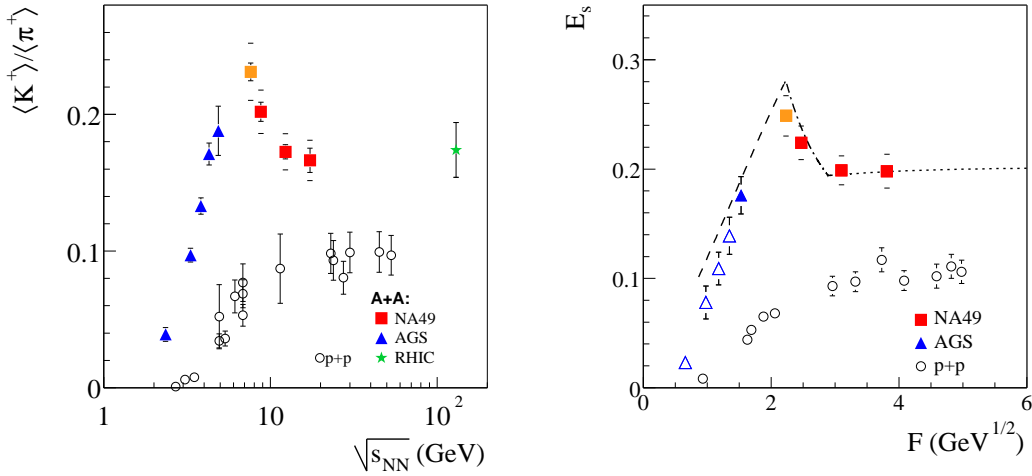


Figure 1.15: The dependence of the $\langle K^+ \rangle / \langle \pi^+ \rangle$ (left) and E_S (right) ratios on the collision energy for central A–A collisions (closed symbols) and inelastic p–p interactions (open symbols). The predictions of SMES for the E_S ratio are shown by a line. Different line styles indicate predictions in the energy domains in which confined matter (dashed line), mixed phase (dashed–dotted line) and deconfined matter (dotted line) are created at the early stage of the collisions (Where $F = (\sqrt{s_{NN}} - 2m_N)^{3/4} / \sqrt{s_{NN}}^{1/4}$).

the measured non-monotonic energy dependence of the strangeness to entropy ratio is followed by a saturation behavior in the deconfined phase which is a direct consequence of the onset of deconfinement taking place at about 30 AGeV.

Experimentally, the strangeness to entropy ratio is closely proportional to the two ratios directly measured through experiments: the $\langle K^+ \rangle / \langle \pi^+ \rangle$ ratio and the $E_S = (\langle \Lambda \rangle + \langle K + \bar{K} \rangle) / \langle \pi \rangle$ ratio. The energy dependence of both ratios is plotted in Fig. 1.15 for central Pb+Pb (Au+Au) collisions and p–p interactions. As seen in this figure the measured dependence is consistent with that expected within the SMES.

Reinforcing the picture of a phase transition, another striking piece of evidence is obtained. The energy dependence of the inverse slope parameter fitted to the K^+ (left) and K^- (right) transverse mass spectra at mid-rapidity for central Pb+Pb (Au+Au) collisions is shown in Fig. 1.16 [48]. The striking features of the data can be summarized and interpreted within the statistical model of the early stages as follows. (1) The T^*

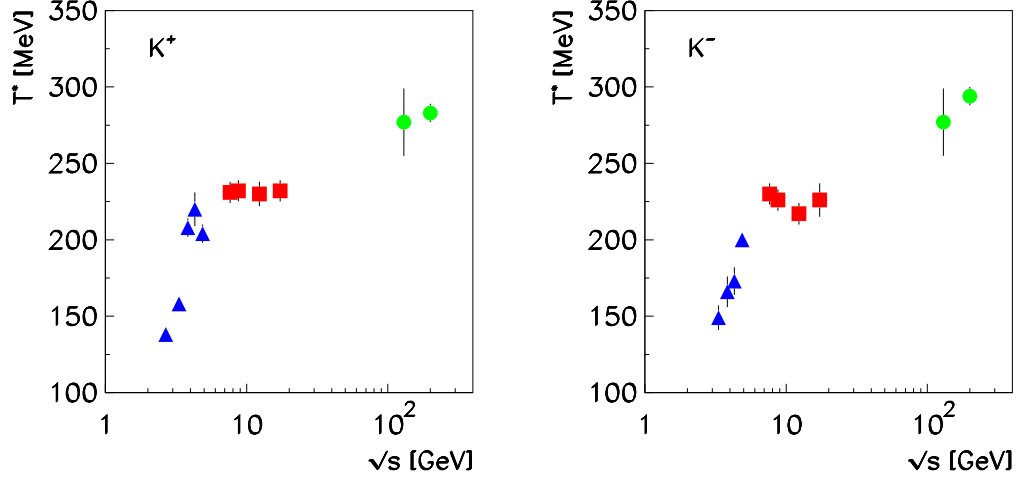


Figure 1.16: The energy dependence of the inverse slope parameter T^* for K^+ mesons produced at mid-rapidity in central Pb+Pb (Au+Au) collisions at AGS (triangles), SPS (squares) and RHIC (circles) energies.

parameter increases strongly with collision energy up to the lowest (30 A·GeV) SPS energy point. This is an energy region where the creation of confined matter at the early stage of the collisions is expected. Increasing collision energy leads to an increase of the early stage temperature and pressure. (2) The T^* parameter is approximately independent of the collision energy in the SPS energy range. In this energy region the transition between confined and deconfined matter is expected to be located. The resulting modification of the equation of state “suppresses” the hydrodynamical transverse expansion and leads to the observed plateau structure in the energy dependence of the T^* parameter. (3) At higher energies (RHIC data), T^* again increases with collision energy. The equation of state at the early stage becomes again stiff, the early stage temperature and pressure increase with collision energy, resulting an increase of T^* with energy.

These predicted signals of the deconfinement phase transition, including anomalies in the energy dependence of hadron production (the strangeness and the step of temperature of kaons) are observed simultaneously at SPS energies. They indicate that the onset of deconfinement is located at about 30 A·GeV. It seems to have clear evidence for the existence of the deconfined state of matter in nature within this SMES.

It is noteworthy also that at 40 GeV, 3/4 of the K^+ are associated with a Λ production.

The peak observed for K^+ should then also reflect an effect of the baryonic density, which is high in the central rapidity at 40 GeV/nucleon but very weak at RHIC (as a consequence particle/antiparticle ratios are close to 1, whereas at 40 GeV/nucleon $\bar{\Lambda}/\Lambda = 2.5\%$). The figure 1.15 left illustrates that particles and antiparticles display very different behavior in this energy domain.

The peculiar role of Λ is due to that the lowest threshold is through $p + n \rightarrow \Lambda + K + n$ for strangeness production, requiring a minimal energy of 671 MeV. In a medium with non-zero chemical potential $\mu_{u,d}$, because densities of u and d quarks are greater than the ones of \bar{u} and \bar{d} quarks, it is much more likely for \bar{s} anti-quark to combine with a u or d quark to form $K^+(u\bar{s})$ or $K^0(d\bar{s})$, than it is for the strange quark s to combine a \bar{u} or \bar{d} to form $\bar{K}^0(\bar{u}s)$ and $K^-(\bar{d}s)$. For the strange quark s , a more likely outcome is to combine with u and d quarks to form $\Lambda(uds)$, $\Sigma^+(uus)$, $\Sigma^0(uds)$ or $\Sigma^-(dds)$, instead of combining with \bar{u} and \bar{d} to produce \bar{K}^0 and K^- .

Calculations based on thermal models account for the maximum observed in the Wroblewski factor at 40 GeV/nucleon by the combined effect of the decrease of the baryonic potential and the increase of temperature with energy. The peak should then mostly be associated with baryonic production [36] (see figure 1.17).

1.3.3 Strangeness saturation

Equilibration time for the strangeness in a hadron gas should be of the order of 40 fm/c, for instance for Kaons in RQMD model [49]. It is higher than the 10 fm/c duration time of the collision, and the thermalization of strangeness is very likely not being complete, but only partial, except if a high level of strangeness is kept in the hadronization process after complete saturation in the QGP phase.

Introducing a factor γ_S is a phenomenological way to account for this incomplete strangeness equilibration, by J. Rafelski [50] in the early nineties through a phase space occupancy factor γ_S , and by the strangeness saturation factor γ_S used by other authors [51]. In the latter case at least, this factor, the probability that a strange quark occupy the cell of phase space and which is multiplying the thermal partition function, is estimated at the primary production stage, before effects of the hadron gas. Strangeness population plausibly evolves through the life time of the system, reaching a high relative value during the QGP eventual phase, changing during hadronization in particular thanks to gluons, and finally influenced by the reinteractions in hadronic gas. One should consider different values of γ_S for these different phases[52].

The Wroblewski ratio $\lambda_S = 2s\bar{s}/(u\bar{u} + d\bar{d})$ is sometime considered to be proportional to

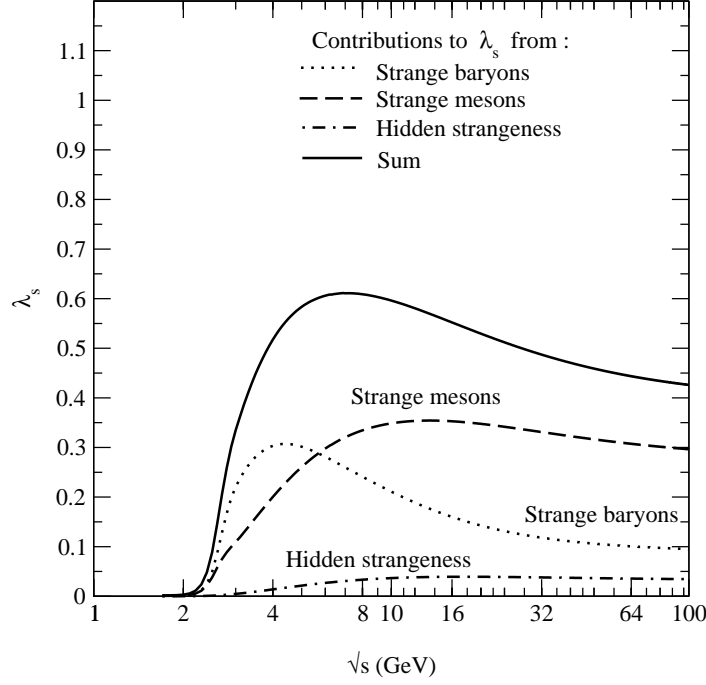


Figure 1.17: Contributions to the Wróblewski factor from strange baryons, strange mesons and hidden strange particles. Full line is a sum of all these contributions.

γ_s [52], but the later could be too sensitive to considered particles and misleading in the ee to A–A comparison [53].

1.3.4 Multiple strange baryons

The relative production of baryons and anti-baryons with strangeness content is also a good signature for the quark-gluon plasma. The direct production of these particles in an hadron collision requires high energy and long time, thus the production of strange baryons in an hadronic gas is less probable, decreasing their content in s quarks. On the contrary, the quark-gluon plasma is abundant in s quarks, so that after the phase transition into an hadron gas, one expects to observe the hierarchy :

$$\frac{(\Lambda)_{QGP}}{(\Lambda)_{HG}} < \frac{(\Xi)_{QGP}}{(\Xi)_{HG}} < \frac{(\Omega)_{QGP}}{(\Omega)_{HG}} , \quad (1.5)$$

since their strangeness quantum numbers are $S_\Lambda = -1$, $S_\Xi = -2$ and $S_\Omega = -3$.

The multiple strange baryon production has been studied by NA57/WA97 experiment in Pb-Pb collisions at 158 A GeV. The results show in agreement with the prediction of the hierarchy Equation 1.5 [54]. In figure 1.18, the results are shown, as a function of mean number of participant nucleon [55]. Figure 1.18 shows that the production of Ω baryon in Pb-Pb collisions at 158 A GeV is increased by a factor of 15, compared to its production in the proton induced collisions. Furthermore, these multiple strange baryon productions in Pb-Pb collisions remains constant, independent of the centrality, for a number of participant higher than 100. These hyperons productions require about 100 fm/c to equilibrate, whereas the life-time of hadronic system is only about 10 fm/c. This hyperon enhancement result can not be explained by interactions in hadronic system.

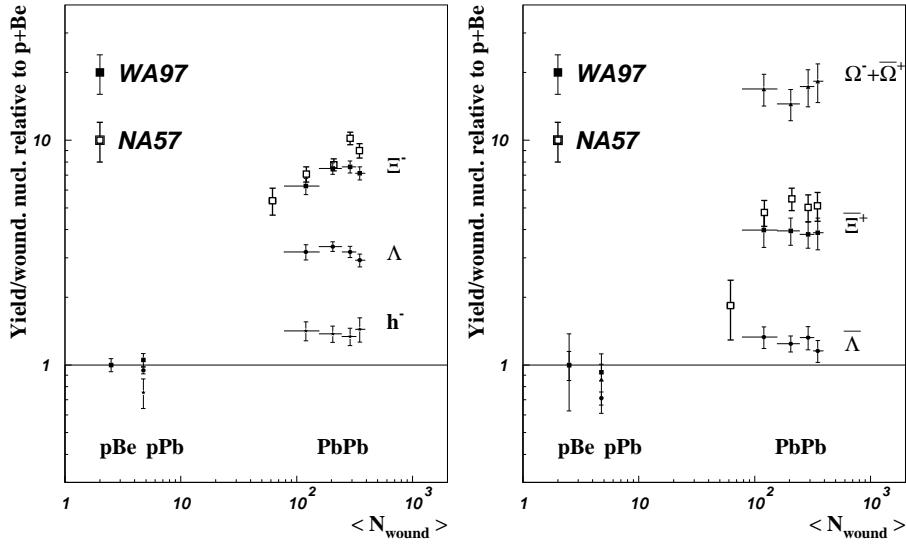


Figure 1.18: The multiple strange baryon production in Pb-Pb collisions at 158 A GeV compared to the corresponding yields in proton induced collisions as measured by NA57/WA97 experiment.

1.4 The ϕ production

The ϕ meson, which is the mainly subject of this study, is a bound state of $s\bar{s}$. Its properties of mass, width and main decay modes are listed in Table 1.1. The production of ϕ has been proposed by A. Shor [28] as a probe to detect the strangeness enhancement due to QGP formation. Firstly, an enhancement of $s\bar{s}$ pairs in the QGP phase should

Quantum Number	$I^G(J^{PC}) = 0^-(1^{--})$
Mass	$1019.456 \pm 0.020 \text{ GeV}/c^2$
Full width Γ	$4.26 \pm 0.05 \text{ GeV}/c^2$
Decay channels	Branching Ratio
$\phi \rightarrow K^+ K^-$	$(49.2^{+0.6}_{-0.7})\%$
$\phi \rightarrow e^+ e^-$	$(2.96 \pm 0.04) \times 10^{-3}\%$
$\phi \rightarrow \mu^+ \mu^-$	$(2.87^{+0.18}_{-0.22}) \times 10^{-4} \%$

Table 1.1: ϕ meson properties (Particle Data Booklet 2002)

lead to an enhancement of ϕ mesons. Secondly, the rescattering of ϕ meson with nucleons and other hadrons in the expanding hadronic phase is insignificant, so the ϕ would retain information on the conditions of the plasma. The ϕ production is studied through a relative production with respect to the non-strange mesons, i.e. the ratio ϕ/ω , related to the ratio $s\bar{s}/u\bar{u}$. This ratio in NN collisions could increase by a factor of 20 in QGP prediction, as compared to the one for hadronic production, if the $s\bar{s}$ and $u\bar{u}$ would be produced at the same level. The ratio ϕ/ω should be close 1 in this QGP occurrence since ϕ and ω have the same net quantum numbers. A special interest of this ratio is that their masses being very close, the potential effects of kinematical biases, for instance linked to the flow, are reduced. Apart from the effects linked to the wider mass domain concerned (see for instance below), the ρ is in a similar situation, except that it has a isospin 1 instead of 0. Then ρ should be 3 times more produced, but this is not holding in the dimuon decay channel since we only detect the ρ^0 state. Usually one considers that the cross section production of ρ^0 is the same as the ω one. This is supported by the experimental measurements [56]. However this similarity of the production is probably restricted to the similar mass domains and exclude eventual low mass tails.

1.4.1 Strangeness saturation factor and ϕ/ω ratio

In thermal models the production is equiprobable for phase space cells corresponding to the same energy. In heavy ion collisions, this corresponds to productions with the same transverse mass M_T . If the production is mainly driven by thermal effects, then the ratio $\phi/\omega(M_T)$ should be directly related to $s\bar{s}/u\bar{u}$. The production of strangeness can also be increased in A–A collisions with respect to p–p collisions but not yet reach the saturation level. Some thermal models introduce this characteristic through the strangeness satura-

tion factor [52, 51, 57], γ_S . In such models the probability to produce a ϕ is proportional to the square of γ_S [58].

The figure in [59] displays the value of $(\phi/\omega)_{\mu\mu}$. A ϕ/ω ratio before decay of about 0.5 should lead, considering the electron pairs branching ratios, to a $(\phi/(\rho + \omega))_{\mu\mu}$ of 1.2. The ratio ϕ/ω of 0.5 corresponds to $\gamma_S \sim 0.7$. Of course the picture has to be improved by taking into account secondary production ⁴, hadronization effects, and eventually flow effects, if one wants a closer estimate of the γ_S at the “primary” stage.

1.4.2 Studies as a function of $p_T^{\mu\mu}$ or $M_T^{\mu\mu}$?

In order to have a direct access to the relative effects acting on the M_T slope or to the estimate of the strangeness saturation factor γ_S , one [60, 61, 62] has considered experimental mass spectra obtained in M_T domains. This is in principle equivalent to the study performed in p_T domains. Only the method biases could be different, allowing an eventual cross check. Also the effective γ_S ⁵ is obtained directly from the ratio ϕ/ω .

Another important difference in the two types of analyses is the way of the smearing and acceptance corrections are done in the treatment. In this analysis, the extraction of the components ϕ , ω is done by a fit of experimental dimuons mass spectra, using components taking into account smearing and acceptance correction. The p_T analysis are performed by another choice (which is independent of the use of p_T bins): the experimental spectrum is corrected for acceptance and smearing [63], and then fitted by using physical distributions (Figure 1.19). The same Monte-Carlo programs are used for both analysis. Finally one observes that the obtained results are very compatible between these two types of analyses.

1.4.3 ϕ/ω or $\phi/(\rho + \omega)$?

Experimentally the dimuon production measured in the NA50 experiment gives access to the ratio $(\phi/(\rho + \omega))_{\mu\mu}$, uncorrected for acceptance. Due to the experimental mass resolution of about 70 MeV, the extraction of $\rho + \omega$ relies on an hypothesis made on the ratio between ω and ρ . Practically this ratio could be changed by a factor of 3, without changing the number of dimuons in the $\rho + \omega$ *uncorrected for acceptance* spectrum by a comparable amount, for instance in this example 30%. This is due to the fact that given the negligible acceptance for very low masses and the large mass spreading, the ρ and ω

⁴This is, for instance, lower by 32% the ω yield (F. Beccatini, private communication)

⁵In fact it is γ_S/γ_q .

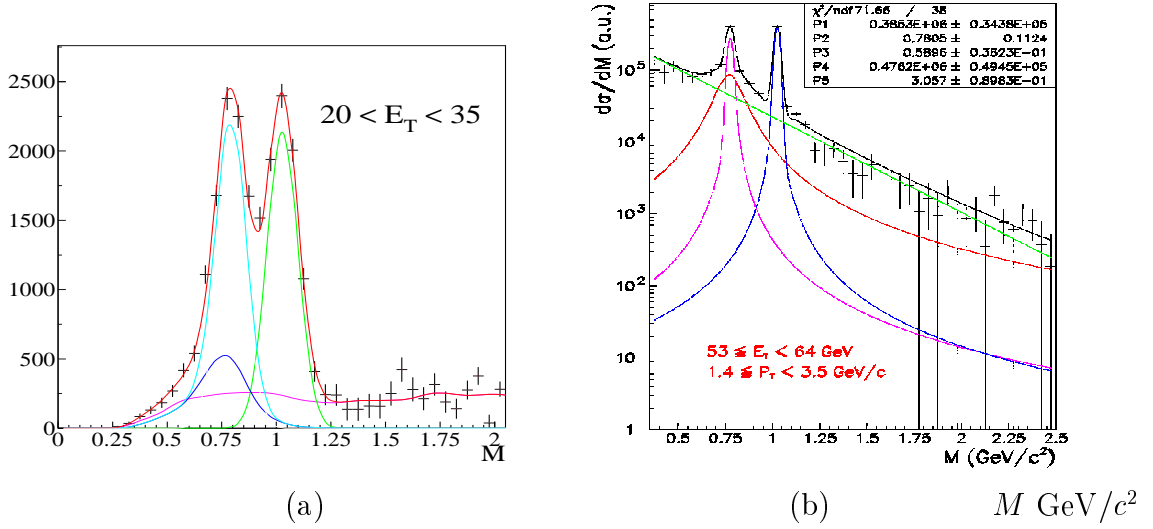


Figure 1.19: The various analysis methods : (a) a fit of the experimental invariant mass spectrum with simulated components taking into account smearing and acceptance effects, (b) a fit with physical components of a mass invariant spectrum corrected for smearing and acceptance. In both cases the same simulation program is used.

uncorrected for acceptance mass distribution have limited differences. On the other hand, the effective ρ mass spectrum is not very well defined. It is not a simple Breit-Wigner distribution. The “phase space” availability [64], i.e. the distribution of the available energy in the primary collisions of partons, is not negligible, and should favour the low masses, as complementarily it should prevent a ρ tail from lying above the upsilon (Υ) production if the Breit-Wigner shape would be directly applied. The ρ is also expected to possibly change its shape due to various effects in heavy ion collisions [65]. All these effects are more specific of the ρ than of the ω , which is less affected by the low mass acceptance. So dealing with *acceptance corrected* results, the ϕ/ω ratio should turn out to be less model dependent than the $\phi/(\rho + \omega)$ one. Anyway in our treatment, the $\phi/(\rho + \omega)$ and the ϕ/ω are directly proportional, i.e, going from one to the other is only multiplied by factor 1.6⁶, and any change in the hypothesis done in the extraction or the acceptance correction process should lead to a new determination. The only difference is that the ϕ/ω ratio is less sensitive than the $\phi/(\rho + \omega)$ to the changes in the hypothesis occurring

⁶With the assumption $\sigma_\rho = \sigma_\omega$, then $\left(\frac{\phi}{\omega}\right)_{\mu\mu} = (BR_\rho + BR_\omega)/BR_\omega \times \left(\frac{\phi}{(\rho + \omega)}\right)_{\mu\mu}$.

outside the NA50 acceptance.

1.4.4 Effective temperature

The dense system created in heavy ion collisions can be described hydrodynamically, i.e., all the produced matter (particles) flow with the same collective velocity. The cross section production for each particle as a function of its transverse momentum or transverse mass ($M_T = \sqrt{M^2 + p_T^2}$) gives information relative to the thermalization of the system and its collective expansion.

From transverse mass distribution one can extract the “effective temperature” that characterizes each particle, i.e. the inverse slope of the distribution. This scaling with M_T is described by a Bessel function $K_1(M_T/T)$ [66]:

$$\frac{d\sigma}{dM_T} = M_T^2 K_1(M_T/T) . \quad (1.6)$$

The effective temperature T only depends on two parameters: the temperature of thermal freeze-out $T_{thermal}$ at which the hadronized system stops interacting, and the mean velocity $\langle v_T \rangle$ of the collective expansion (the flow) in the transverse plane.

In a non-relativistic regime (i.e. if the particle’s mass is not negligible, $M \gg p_T$), one has [66]:

$$T = T_{thermal} + \frac{1}{2} M \langle v_T \rangle^2 , \quad (1.7)$$

and so it is possible to know separately $T_{thermal}$ and $\langle v_T \rangle$, and the effective temperature is observed to vary linearly with the particle’s mass.

In the relativistic regime, when the particle’s transverse momentum is very high ($p_T \gg M$), the mass can be neglected and the observed effective temperature is the same for all the particles. In this case, it is impossible to distinguish T and $\langle v_T \rangle$ [66]:

$$T = T_{thermal} \sqrt{\frac{1 + \langle v_T \rangle}{1 - \langle v_T \rangle}} . \quad (1.8)$$

1.4.5 Experimental results of ϕ yield

The ϕ meson yield is measured through K^+K^- [67] and $\mu^+\mu^-$ [59] decays. It was found that the ϕ multiplicity extracted from the K^+K^- data is significantly smaller than that obtained from the dimuon results [68]. A similar effect has been observed recently by PHENIX results [69] in Au–Au collisions at RHIC. A possible interpretation of this puzzle is the scattering of at least one of the daughter kaons in the nuclear medium [70] accompanied by the in-medium modifications of kaons and ϕ masses (see chapter 6).

1.5 Future searches

The situation of exploring the QGP will change at RHIC and LHC. Future searches for QGP are aiming at accessing higher temperature and higher densities.

The RHIC collider experiments in USA, including PHENIX, STAR, BRAHMS and PHOBOS ([71, 72] etc.), are taking data with gold collisions at $\sqrt{s} = 130$ GeV and 200 GeV. The temperature reached in the early stage of the collision system is clearly higher than the critical temperature needed for the phase transition. Some new signatures are proposed and studied for QGP formation in heavy ion collisions, like jets physics and high p_T distribution, Jet quenching has probably been observed.

The LHC collider at CERN is supposed to run in a few years. The ALICE, ATLAS and CMS experiments are planning to run at $\sqrt{s} = 5.5$ TeV. With so big and long life-time system, and much larger temperature, the multiplicity of produced particles will be very large. With high statistics, it is possible to study the abundant production of thermal photons and dileptons, jets, in particular study the bottomonia states particles.

Finally, another condition of the phase transition is sufficiently high baryonic density. The future experiments at SIS synchrotron from GSI are following this way, to reach very high densities similar to the core of the neutron stars, several times higher than the normal nuclear matter density (see Figure 1.20).

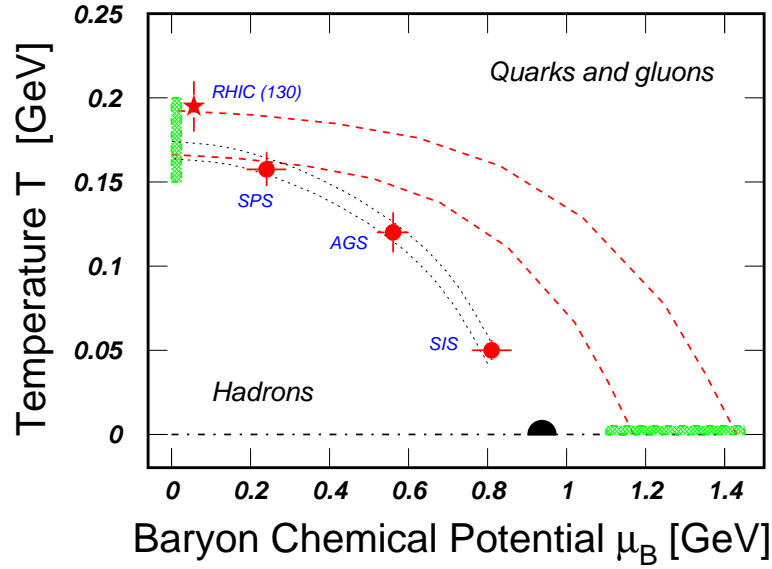


Figure 1.20: Phase diagram of strongly interacting matter in the temperature T and baryonic chemical potential μ_B . The points indicate $T-\mu_B$ values extracted from analysis of hadron multiplicities in central nucleus–nucleus collisions.

Chapter 2

Experimental apparatus

The NA50 experiment is a fixed target experiment using a lead ^{208}Pb ion beam accelerated at an ultra-relativistic energy of 158 GeV/nucleon, obtained from the proton synchrotron SPS at CERN. The accelerator has a 20 s cycle, with a 4.5 s spill. The beam Lorentz contraction effect is $\gamma = 10$.

The NA50 experimental apparatus consists of a muon spectrometer, complemented by an electromagnetic calorimeter, an hadronic calorimeter, a multiplicity detector, an absorber and several detectors for beam control [8]. The correlated muon pairs are detected at rather small angles in the laboratory reference frame, but correspond to an emission from 90° in the collision's center-of-mass reference frame). Figure 2.1 gives a schematic view of the apparatus.

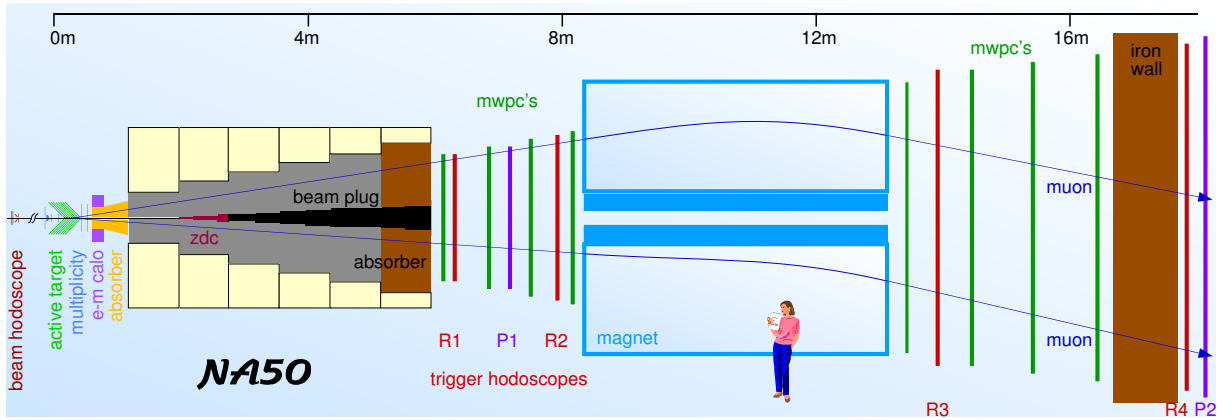


Figure 2.1: The NA50 experimental apparatus in the configuration used for the study of Pb–Pb collisions.

2.1 Beam detectors

The Beam Hodoscope (BH) and its associated detectors are located 22 m upstream from the target, where the beam transverse dispersion allows for the counting of the incoming beam ions.

2.1.1 BH detector

The Beam Hodoscope is made of two planes of quartz blades, transversal to the beam direction. Only the first one is actually used during the data taking. The 16 constituent blades of the first plane are 0.7 mm thick, corresponding to 2.2% interaction length ($\lambda_{int}(\text{quartz})=3.2$ cm for Pb ions) [61]. Quartz blades are resisting to the high radiation dose due to the huge beam intensity, up to the order 7×10^7 .

The Pb ions, when crossing the quartz blades, produce Čerenkov radiation, captured by the optical fibers connected to the blades up to the photomultipliers (one photomultiplier per blade).

The detector is used for several purposes. It counts the incoming ions on the Pb beam, a very important measurement for the luminosity calculation. It also allows to identify pile-up in the beam – a situation where every time there are two or more ions seen by the detector in the same window of 20 ns. The BH also used to stabilize the trigger of the experiment, giving a time reference for the arrival of the incoming ions, with less than 1 ns jitter¹.

2.1.2 Interaction detectors

The interaction detectors BHI and BHI-New are located next to the beam hodoscope, in order to identify any possible interactions in the BH itself, whose fragments may interact on the target, thus producing “parasite” events. There are two BHI detectors and four BHI-New, each one having a scintillator blade plus a Pb blade.

The BHI are placed 17 cm downstream from the second BH plane, on both sides of the beam, and have a rectangular geometry. The BHI-New shape is as quarters of ring centered on the beam line, located 1 m after the BHI detectors and cover complementary rapidity regions.

Pb ion interactions on the BH produce mainly pions. These decay into photon pairs when crossing the lead blades, producing a signal that allows for the detection of parasite

¹The term jitter refers to the small fluctuation on the time measurement

events. The efficiency study of these event will show that the fragments produced have quite 100% probability to interact in the preabsorber, producing about 5% of the measured muon pairs.

2.1.3 Anti-halo detectors

The two anti-halo detectors (BAH and BAH-New) are located 51 cm and 19cm upstream from the target. Each of them consists of a quartz blade with central hole 3 mm in diameter, crossed by the collimated ion beam. These detectors identify events whose originating ion was not collimated, or originating on charged fragments from previous parastic interactions occured upstream from the target. They are then very sensitive to the previous fragments.

2.2 The target region

The data analysed here was obtained with a single lead target 4 mm thick put in the vaccum and 1 cm² transverse dimension. The target frame can accommodate up to 7 sub-targets aligned with the beam. In the year-2000 data taking only position 4 was occupied. Next to each sub-target position, there are two quartz blades (on the left and on the right sides of each sub-target and immediately downstream from it). The blades emit Čerenkov radiation when crossed by charged particles (mostly π and K) originating from in-target interactions. In addition to this signal, δ electrons are produced simply when the beam crosses the target, independently of nuclear collisions, and this creates a noise which is also seen by the quartz blades. There is then a minimal threshold below which the detector cannot be used. (see Figure 2.2).

The two quartz blades are located before the first sub-target position, to detect lead-air interactions upstream from the target. Figure 2.3 shows the target region, together with the centrality detectors.

2.3 Detectors for the centrality measurements

In order to determine the centrality of the Pb-Pb collisions, two calorimeters and a multiplicity detector are invited. The electromagnetic calorimeter (EMC) and the zero degree calorimeter (ZDC) are constructed to measure the neutral transverse energy of the produced particles and the energy of the spectator nucleons and the fragments of the collision,

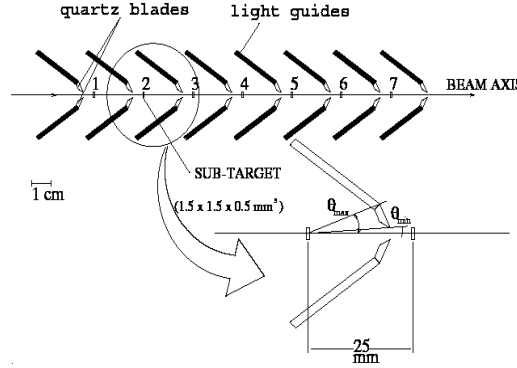


Figure 2.2: The layout of the active target (in 2000 data runs, only 1 sub-target located at position 4) region.

respectively. The multiplicity detector measures the multiplicity of charged particles produced.

2.3.1 The multiplicity detector

The multiplicity detector (see Figure 2.4) is placed downstream from the target and before the preabsorber. It is made of two planes (MD1 and MD2) with about 7000 silicon microstrips for each, in a ring shape [73]. Since silicon is a hard radiation material, the detector can be put right next to the interaction region. The two planes allow for the muon tracking and identification of the sub-target, where the collision occurred. The multiplicity of the charged particles produced is measured from the strip occupancy. The superposition of the two planes covers the pseudo-rapidity region $\eta \in (1.9, 4.2)$ [74].

2.3.2 The electromagnetic calorimeter

The electromagnetic calorimeter is located after the multiplicity detector. Its inner region is filled by the preabsorber. The EMC is made of four concentric hexagonal “rings” with six sextants for each, and detects the neutral particles in the pseudo-rapidity interval $1.1 \leq \eta \leq 2.3$, out of the spectrometer acceptance.

The calorimeter is made of lead and scintillating fibers. There are many π^0 s produced in Pb-Pb collisions, they have a short lifetime, decaying into the photon pairs. The Electromagnetic cascades begin in the lead, and encounter the scintillating fibers. The fibers are active and sensitive elements of the calorimeter, and transport the signal up

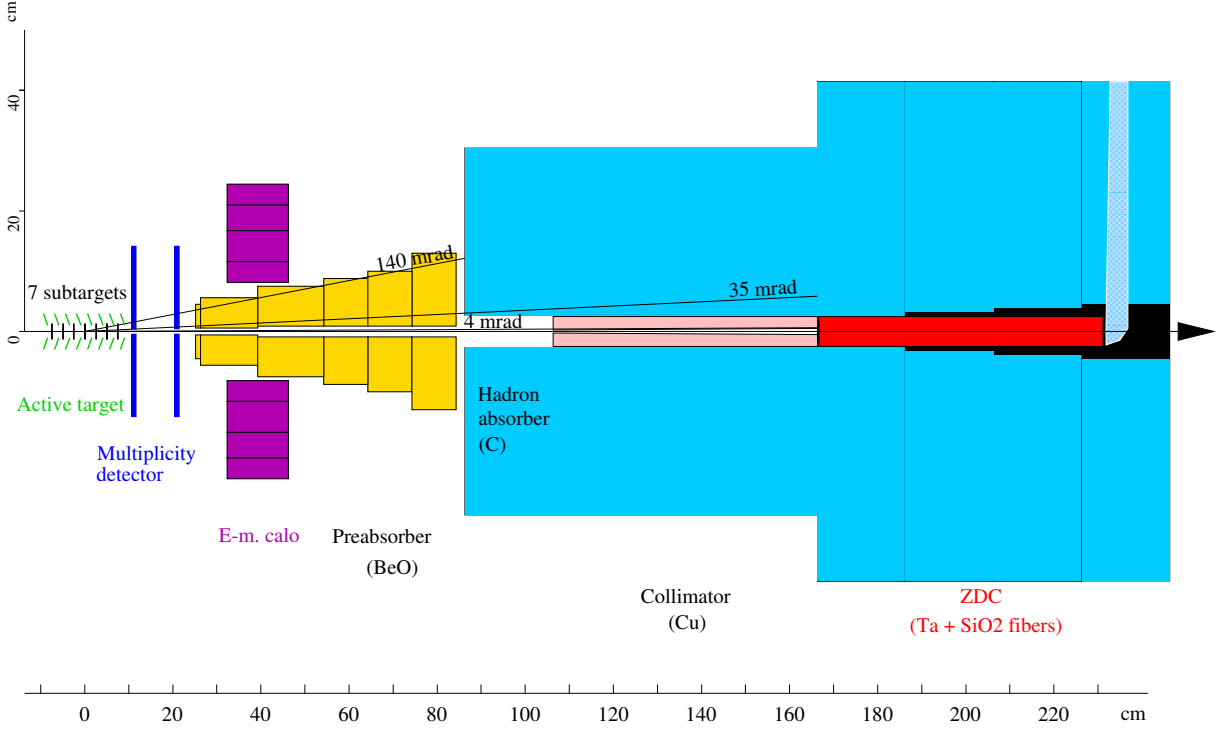


Figure 2.3: A schematic view of the NA50 apparatus in target region.

to the photomultipliers. The neutral transverse energy produced is calculated from the expression :

$$E_T = C_N \sum_{i=1}^4 E_i \sin \theta_i \quad , \quad (2.1)$$

where C_N is the normalization constant, depending on the sub-target position where the interaction occurred, and the variable i is for the four calorimeter rings. The angle θ_i is the angle defined by the i^{th} ring and the beam line from the sub-target position N .

The neutral transverse energy resolution [75] for the NA50 experiment is ,

$$\frac{\sigma(E_T)}{E_T} = \frac{0.62}{\sqrt{E_T(\text{GeV})}} \quad , \quad (2.2)$$

i.e., about 14% at $E_T=20$ GeV, and about 6.2% at $E_T=100$ GeV.

2.3.3 The Zero Degree Calorimeter

The zero degree calorimeter is placed inside of the absorber, along the beam line. It is made of tantalum conversion plates, with silicon optical fibers inserted. Measurements

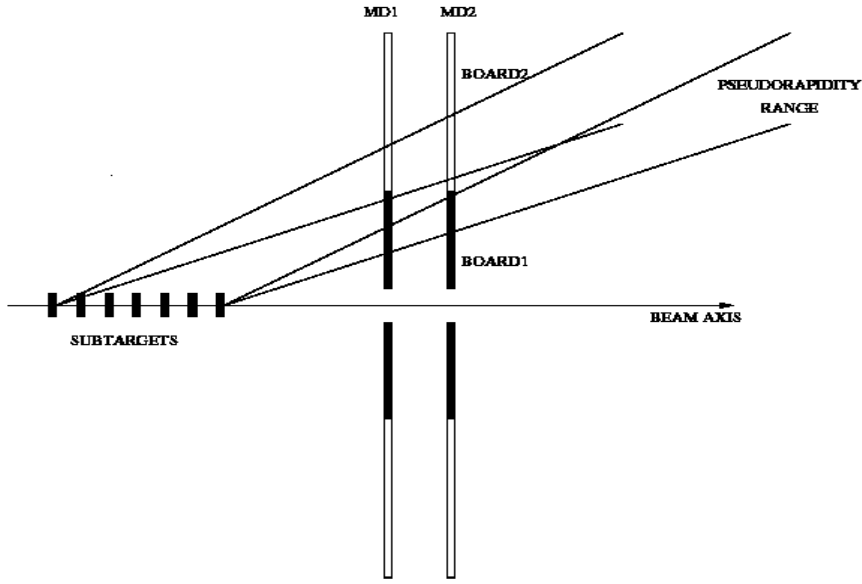


Figure 2.4: The multiplicity detector planes MD1 and MD2.

are based on the Čerenkov effect. The detector is preceded by a copper collimator 60 cm long, with central conical shaped hole whose diameter is only slightly larger than the beam transversal dispersion, in order to prevent the ZDC from counting deposited energy by the produced particles (see Figure 2.5) .

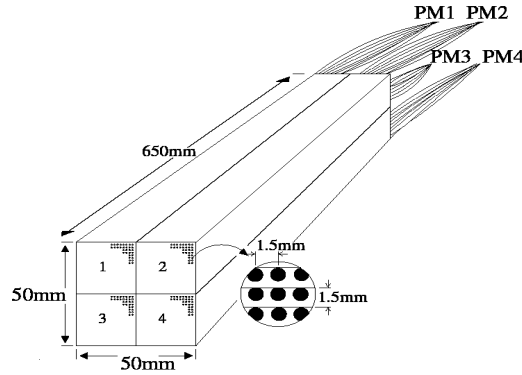


Figure 2.5: The zero degree calorimeter

In the detector's active region the quartz fibers are oriented parallel to the beam, along 65 cm ($\approx 20\lambda_I$). They are then curved at 90° , working as light-guides up to

the photomultipliers. The ZDC measures the particles' deposited energy in the pseudo-rapidity region $\eta \geq 6.3$.

The energy resolution of this detector when using lead beam at 158 GeV/c per nucleon is [75, 76, 77]:

$$\frac{\sigma(E_{ZDC})}{E_{ZDC}} = \frac{3.39}{\sqrt{E_{ZDC}}(\text{GeV})} + 0.062 + \frac{1227}{E_{ZDC}(\text{GeV})} \quad , \quad (2.3)$$

i.e., 12% for $E_T \approx 20$ GeV ($E_{ZDC} \approx 28$ TeV) and 25% for $E_T \approx 100$ GeV ($E_{ZDC} \approx 8$ TeV) .

Besides the measurement of the non-participant particles energy, the ZDC also allows for pile-up beam identification, completely independent from the beam hodoscope BH. The two detectors together accomplish an efficiency for the beam pile-up rejection higher than 99% .

2.4 The Muon spectrometer

The NA50 muon spectrometer, made of absorbers, multiwire chambers, scintillating hodoscope and a deflector magnet, was conceived and previously used by the past experiment NA10 and NA38. It selects correlated muons, allowing to reconstruct muon tracks and identify the production vertexes.

The spectrometer consists of two telescopes (sets of multiwire chambers and hodoscopes) [8], with a magnet in between, covering the pseudo-acceptance region $2.8 \leq \eta \leq 4.0$ (see Figure 2.6).

2.4.1 Absorbers

Lead ion collisions produce a huge amount of particles, mainly pions and kaons that have a large probability to decay into muons, thus leading to a large background to the dimuon signal detection. The absorbers minimize this background, otherwise this large background would saturate the multiwire chambers and hodoscope.

In NA50 there is a beryllium oxide (BeO) pre-absorber filling the inner region of the electromagnetic calorimeter and extending as a cone up to the main absorber of the experiment. It is basically a block of material 60 cm long, with a certain hole for the non-interacting beam to pass through.

The main absorber of the experiment, shown in Figure 2.7, is 4.8 m in length and made of uranium blocks for the most central part, iron and carbon blocks next, and concrete

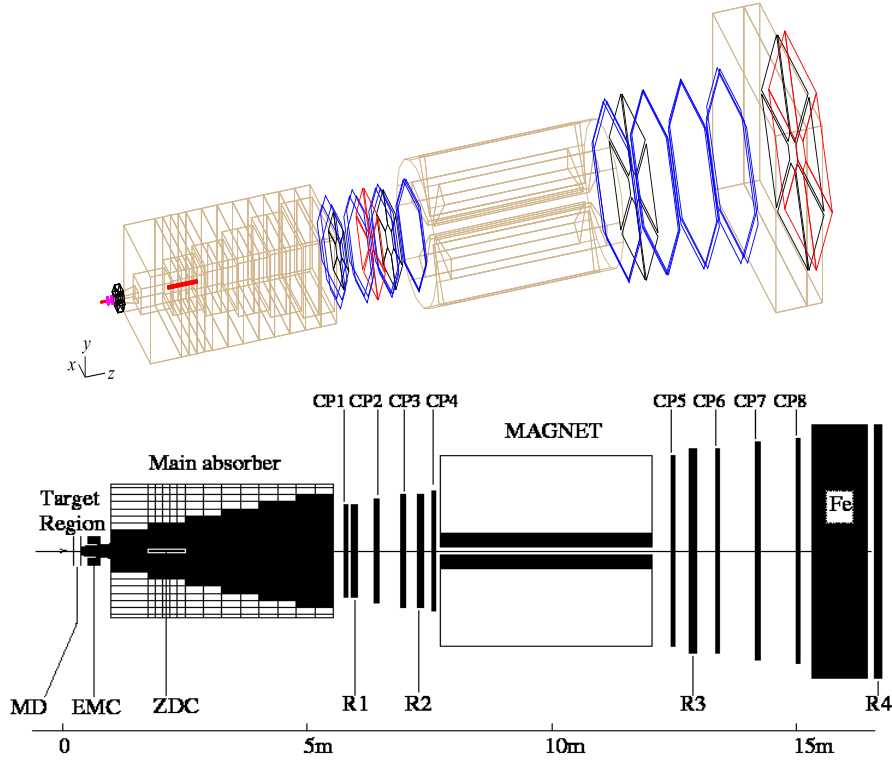


Figure 2.6: The muon spectrometer

in the more exterior layer, covering an angular acceptance for in-target events from 32 to 116 mrad.

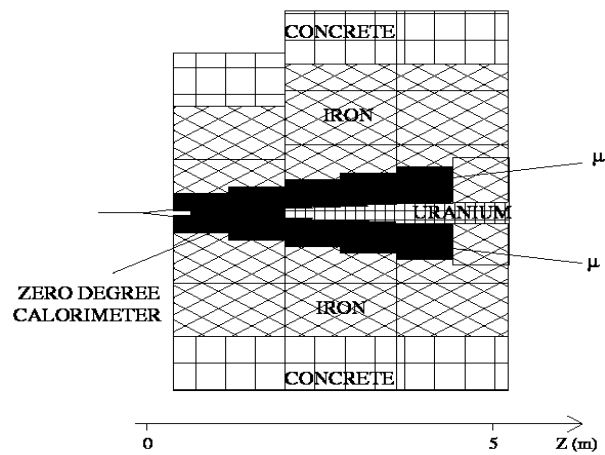


Figure 2.7: The absorber

The absorbers stop the produced hadrons, but on the other hand, they are a source of multi-scattering for the muons. So the choice of materials when building an absorber is done by maximizing the interaction length λ_I ($\lambda_I \propto A^{1/3}$), so that the produced hadrons are absorbed, while minimizing the radiation length X_0 ($X_0 \propto A/Z^2$), so that the energy loss of muons is as less as possible ($-\frac{dE}{dx} \propto \frac{Z}{A}$), as well as the multi-scattering (the scattering angle being $\theta_0 \propto \sqrt{l/X_0}$).

The last absorber, an iron wall 1.2 m thick, is placed before the fourth scintillating hodoscope. From all the in-target produced particles, only the muons can survive crossing this last absorber.

2.4.2 Scintillating hodoscopes

The four scintillating hodoscopes, two per telescope, give the time coincidences that produce the dimuon trigger of the experiment. They have an hexagonal symmetry, each sextant being made of scintillators (30 for R1 and R2, 24 for R3 and 32 for R4), placed parallel to the exterior border of sextant. Scintillators R1 and R2 are homothetic with respect to the target, so that the coincidence $V^i = R1^i \times R2^i$ (or $\times R2^{i-1}$) between two i Scintillators of R1 and R2 is defined when a particle coming from the target region crosses them (see Figure 2.8).

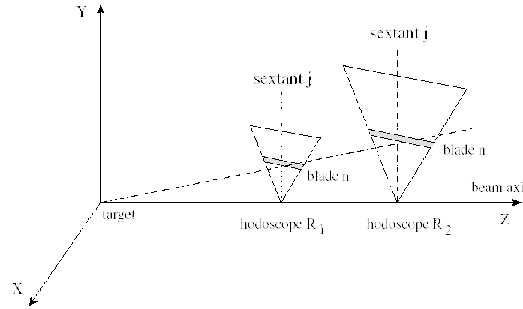


Figure 2.8: A schematic view of the scintillating hodoscopes

The trigger hodoscope efficiency is controlled by two other hodoscopes, P1 and P2, placed before and after the magnet (see in Figure 2.1), during dedicated special runs.

2.4.3 Multiwire proportional chambers

The eight multiwire proportional chambers from PC1 to PC8, four per telescope, are used for tracking of the muon trajectory, from the physical address of touched wires. They have

hexagonal symmetry, each chamber having three independent wire planes, spaced 2.2 cm apart and rotated by 60° with respect to each other (in Figure 2.9).

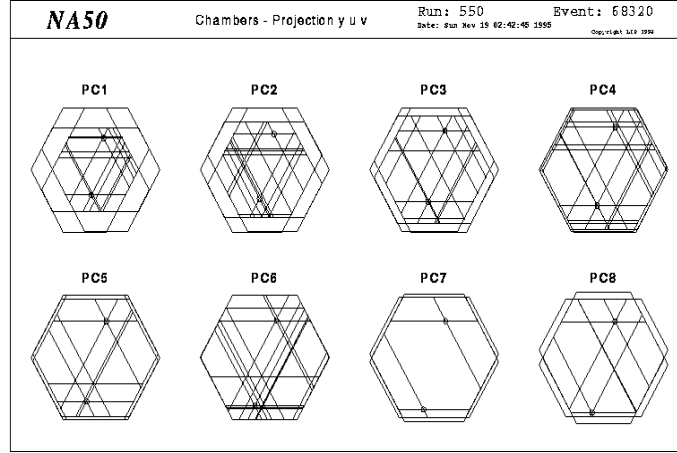


Figure 2.9: The Multiwire proportional chambers PC1 to PC8.

Spacing between wires is 0.3 cm, thus having a spacial resolution of $0.3/\sqrt{12}$ cm. The inside volume of the chambers, in between cathodes and in the wires (anodes) is filled with a gas mixture at atmospheric pressure. When a muon crosses the chamber, electrons are emitted due to the gas ionization, and these are attracted to the wires because of the applied magnetic field.

2.4.4 The Magnet

The detector magnet ACM (from Air-Core Magnet) between the two telescopes is an iron and air magnet with hexagonal symmetry, where the iron sectors represent only 30% of the total region. With a length of 4.8 m and a maximum radius of 2 m, it defines an acceptance for the spectrometer that is corresponding to the air sectors in between coils.

The current on the coils is AC with a value of 7000 A, synchronized with the SPS cycle, creating a toroidal magnetic field of $B_0 = 0.4$ Tm :

$$\vec{B}(r) = \frac{B_0}{r} \vec{u}_\phi \quad , \quad (2.4)$$

where r is the distance from the beam axis and \vec{u}_ϕ is the azimuthal unitary vector. When crossing the magnet, the muon's trajectory is deflected, but keeping the same azimuthal plane. The bending angle is inversely proportional to the muon transverse momentum.

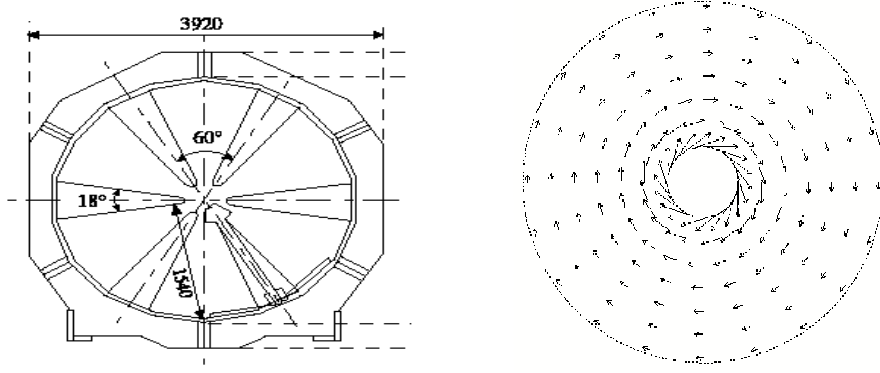


Figure 2.10: The magnet and the shape of magnetic field.

The 7000 A current on the coils is chosen such that the mass resolution is optimized for the J/ψ – the NA38 experiment used a 4000 A current, obtaining a resolution of $\sigma_{J/\psi} = 145 \text{ GeV}/c^2$, while when using 7000 A the mass resolution is $\sigma_{J/\psi} = 96 \text{ GeV}/c^2$. But this strong magnetic field effect causes the drawback of low M_T acceptances for low mass dimuons.

2.5 The trigger system

1. Dimuon Trigger

Four hodoscopes (R1 to R4) provide the muon pair trigger. The first two hodoscopes R1 and R2 are placed between the main absorber and the magnet, the other two R3 and R4 are placed after the magnet, one before and the other after the iron wall. The trigger efficiency is measured with a new system of two hodoscopes P1 and P2, especially designed and adapted for this purpose (see Figure 2.1).

The dimuon trigger select events in which dimuons are produced by interaction in the target, and reject muons from interactions in the beam absorber. Dimuon trigger firstly selects events in which the 2 tracks of a dimuon candidate originated in the target have crossed the spectrometer in 2 different sextants. This trigger is based on the coincidence between the scintillators of R1 and R2 hodoscopes. Thus the muons that have been strongly deflected in the absorber because of the multiple scattering are eliminated. Then the obtained signal is put in coincidence with the R3 and R4 hodoscopes. The trigger system also provides a rough value of the deflection angle, the transverse momentum p_T of each muon.

In order to get a better precision on the timing of the dimuon trigger, which is opening the ADC, starting the TDC, and then in particular a better stability for the studies of the shape of the signals from the calorimeter, the dimuon trigger is used as a 5ns gate for the BH signals. The output of this coincidence is used as dimuon trigger, and has a much better precision (roughly from 6ns FWHM to 0.3). In 2000, this procedure has been extended to all trigger, in order to avoid any bias in the comparisons (especially critical after the E_T knee)

2. Minimum Bias ZDC Trigger

The trigger signal is recorded each time when the ZDC signal is higher than a fixed threshold. A very low threshold value has been chosen in order to have a signal each time whenever something comes into the ZDC. Most of the triggers are events that a Pb ion did not interact in the target and thus deposited all its energy in the calorimeter.

3. Minimum Bias BH Trigger

The 16 constituent quartz blades of the Beam Hodoscope (BH) are used to count the incoming ions on the Pb beam. one of the 16 blades, the 4th, is used for a new minimum bias trigger. In order to cope with the acquisition rate, it is prescaled. The interest of this minimum bias trigger is that it is a priori independent of the transverse energy, which is important in particular regarding the high E_T behaviour.

2.6 The data acquisition system and the reconstruction of tracks

Normal data taking conditions mean a lean ion beam with a nominal data acquisition rate of 1.5 Mby/s [8]. In order to process the data as the fastest way as possible, minimizing the dead time, each sub-detector acquisition (partition) is processed in parallel.

During the 4.5 s spill each sub-detector information is stored in a temporary memory, through a network of 24 transputers, with maximum storage of 5000 events per burst, up to ~ 20 Mega bytes of the data.

The burst information is then transferred to a memory located in the acquisition unit. During the inter-burst, for each event a microprocessor reads all the partitions, and verifies the presence of the information from all the detectors, and its coherence. After validation, the data corresponding to all the events of the burst are recorded in magnetic tape.

The reconstruction of the muon trajectories is done off-line, by the program DIMUREC. The reconstruction of tracks is sketched in Figure 2.11.

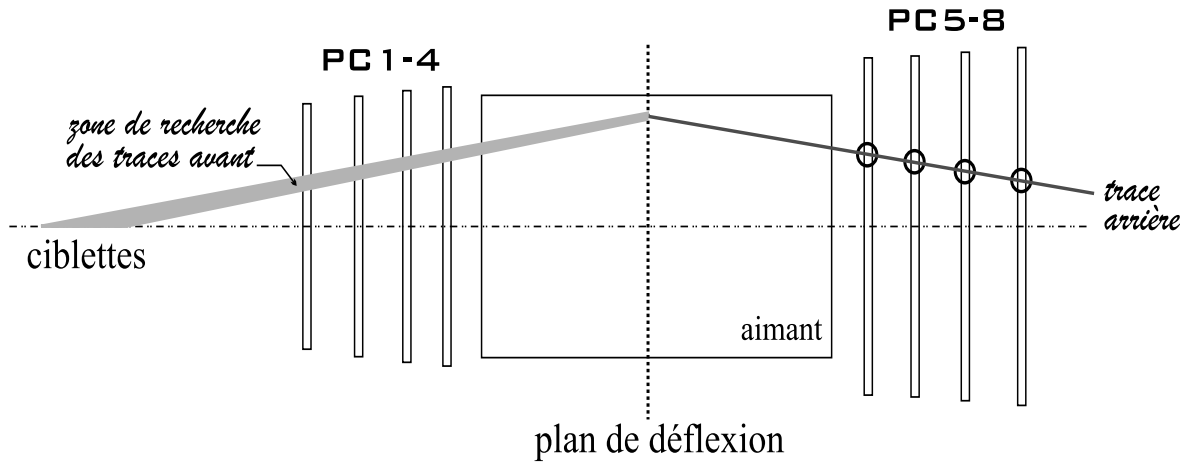


Figure 2.11: The schematic view of the reconstruction of tracks.

2.7 Experimental improvements for 2000 runs

In summary, for 2000 data taking, there are several improvements of experimental conditions, including

1. Only 1 sub-target is used and put in the vacuum up to the pre-absorber, in order to remove the air in the target region ;
2. A new method to detect double interactions is developed, based on the EMC detector ;
3. A new target identification method is used, based on the better correlation between the number of hits on the two MD planes ;
4. Minimum bias trigger is improved in two ways: the timing of all triggers is improved by using a coincidence with BH blades; and a new minimum bias trigger is built, based on beam hodoscope (BH)

These improvements are aiming at detecting the peripheral collisions for Pb-Pb. As a consequence, the minimum bias can go up to $E_T = 3$ GeV, and reach full efficiency at $E_T = 15$ GeV.

Chapter 3

Data Selection and Analysis Treatment

The raw experimental data recorded in the magnetic tapes consists of information of fired wires in the chambers, signal amplitudes in the calorimeter rings, hodoscope and sub-detectors. After the track reconstruction done off-line, the compressed information of the kinematic variables of the two muons, and of the sub-detectors of each event is kept in μ DST (Micro Data Storage Tapes). More detailed raw information is available at the μ DST stage thanks to several sets of additional μ DST.

For Pb-Pb 2000 data runs, two successive productions of standard and additional μ DSTs have been completed at CERN. In this analysis, it is referred to the 2nd (final) version production of μ DSTs, including in particular a new reconstruction method [78], leading to 10% more reconstructed muon pairs before cuts.

The RELMIC program reads the μ DSTs and provides the physical information. The event selection is done at this stage. All the tracks passing outside the fiducial region of the detector are rejected, as well as the image cut is performed (see below). These primary event selections are done in RELMIC program.

The information used for the event selection :

1. the beam pileup : *NIBHTD*, *NIBHAD*, *NIZDC*;
2. the interaction pileup : *NICALO* ($T0J^1$);
3. the upstream interaction in the target : *NPARAS*;
4. the target identification : *NOCIBI*, *NOCIMD*;

¹It is the trigger timing with respect to the incoming ions with a time instability about 1ns.

5. the beam quality : *NOHALO* ² ;
6. the reconstruction quality of the tracks : P^*Dtarg , Global cuts ;
7. the centrality correlation: $E_T - E_{ZDC}$ Diagonal (*Banana*) cut ;

The meaning of these variables will be precised in the following.

The data production of μ DST tapes are separated into four parts: runs 9199-9558, runs 9559-9827, runs 9115-9197 and runs 9718-9757. These runs correspond respectively to the tapes NV0400-NV0407 and NV0408-NV0415 (the last part is corresponding to Low Intensity runs).

3.1 The image cut

In a given magnetic field, the spectrometer acceptance is not the same for positive and negative charged muons. This could be a problem for the combinatorial background determination [80]. The image cut is aiming at symmetrizing these acceptances.

The image track is a simulated track obtained by considering the same momentum than the original track, but with an opposite muon charge. The image cut is rejecting the original track whose image is not accepted by the detector geometry or by the reconstruction criteria or cuts.

3.2 The Pileup cut

The Pileup events are referring to either beam pileup in the BH, or interaction pileup events in EMC detectors.

BH detector's purposes is to identify the beam pileup when two or more incoming ions are seen by the detector in a ~ 20 ns time window. This cut is done through *NIBHTD* by using the BH TDCs and BH ADC information. The cut effect of pileup is seen in Figure 3.1.

Another beam pileup rejection is identified by the ZDC through the variable *NIZDC*. ZDC is used to measure the non-participant fragment energy. It also allows for pileup rejection, and its inefficiency is independent from the BH one. So the BH and ZDC detectors together efficiently reject the beam pileup events up to higher than 96%.

²For 2000 data, the cut *NOHALO* from the anti-halo detector was not used, since it was observed to bias transverse energy (E_T) spectrum for central Pb-Pb collisions, probably because of the back-scattering from the target.[79]. Anyway it was mostly redundant with *NPARAS*.

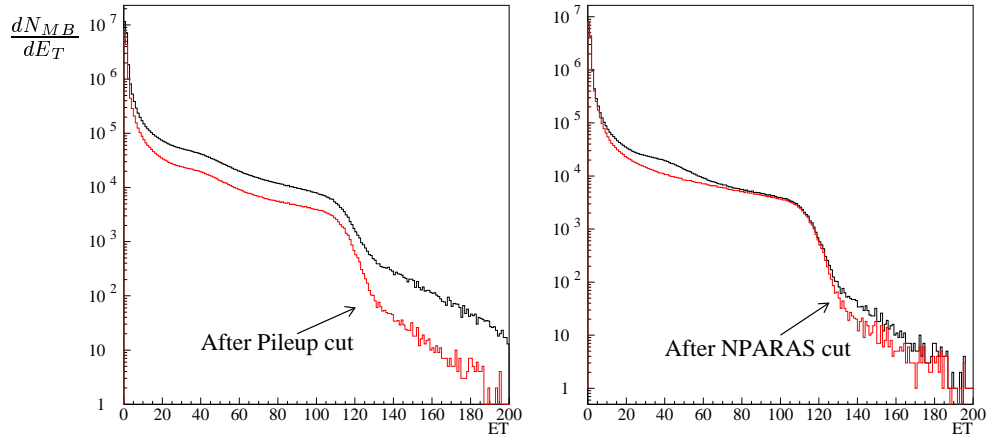


Figure 3.1: *Pile-up* (left) and *NPARAS* (right) cut effects on minimum bias E_T spectrum.

The interaction detectors can identify any possible interactions having taken place in the BH itself. These upstream interactions introduce in the target region some “parasite” events, as described in section 2.1.2. Scintillators of BHI and BHI-New can detect interactions in BH (variable *NPARAS*). The effect of *NPARAS* cut is plotted in Figure 3.1.

Interaction pileup events are identified by the variable *NICALO*. *NICALO* information rejects the pileup of interacting events. This is seen by the EMC detector, through an analysis of the time shape of the signal, and it has been verified to be reliable except for very low E_T , due to the fluctuations of small signals in the calorimeter. Other parasite events are also rejected by this cut (see Figure 3.2). So in this study, we consider *NICALO* and BH *PILEUP* cuts in order to have the cleanest minimum bias sample achievable.

3.3 The target identification (*NOCIBI* and *NOCIMD*)

The target selection is to accept only events for which the active target system identifies an interaction in the position where the lead sub-target is located (for 2000 data, only *NOCIBI*=4).

An event selection based on a target identification using the multiplicity detector has also been studied in [63]. The tracks from secondary particles detected by the two multiplicity detector planes are extrapolated to the target region, pointing to the sub-target region where the interaction occurred (the variable *NOCIMD*). With respect to

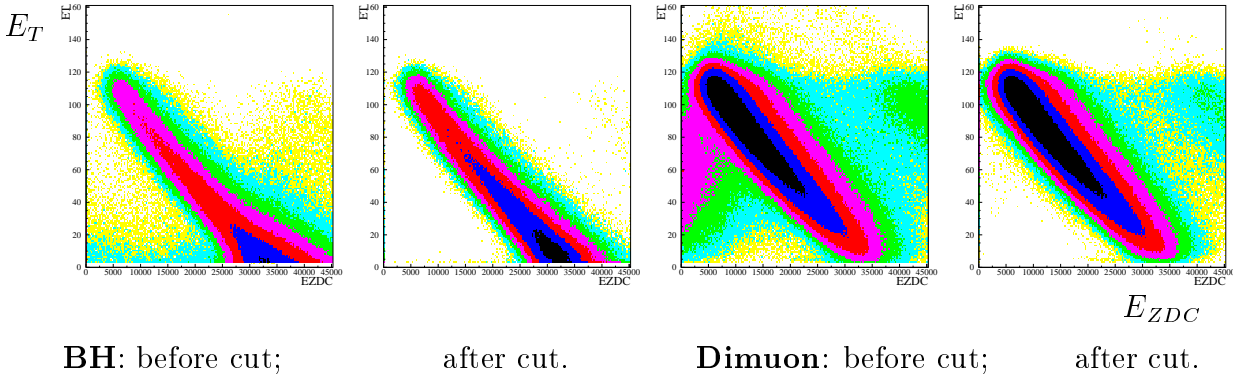


Figure 3.2: *NICALO* cut influence on minimum bias (BH) and Dimuon trigger events in $E_T - E_{ZDC}$ plane.

1996 and 1998 data, a better correlation between the number of hits on the two MD planes (MD1 and MD2) is obtained in 2000 as a consequence of the vacuum up to the pre-absorber, removing the air in the region of the only target used. *NOCIMD* has a better efficiency than *NOCIBI* in peripheral interactions, it is even sensitive enough to reject the low E_T background (see in [74]). In figure 3.3, the minimum bias (BH Trigger) E_T spectrum cut with *NOCIMD*=4 displays that a low E_T dip is strongly reduced with respect to the one obtained with *NOCIBI*=4. For dimuon trigger, the effect is very similar. In the following analysis the cut *NOCIMD*=4 is used.

3.4 P^*Dtarg cut on tracks

The geometrical parameters for the reconstruction are studied so as to eliminate the tracks whose production is out of the interaction region or whose tracks have been considered to be damaged.

The event selection is improved with the P^*Dtarg cut variable, where the distance $Dtarg$ is the distance, in the transverse plane for the axis z , between the position $N(0, 0, z_{Target})$ and the reconstructed track position $M(dx, dy, z_{Target})$, seen in Figure 3.4. The distance $Dtarg$ is calculated as :

$$Dtarg = \sqrt{(dx)^2 + (dy)^2}. \quad (3.1)$$

On the target plane, the tracks whose extrapolation is too far from the vertex in the beam line are rejected. P^*Dtarg are tuned to take into account the fact that there is a different behavior for convergent or divergent tracks. Being due to multiple scattering in

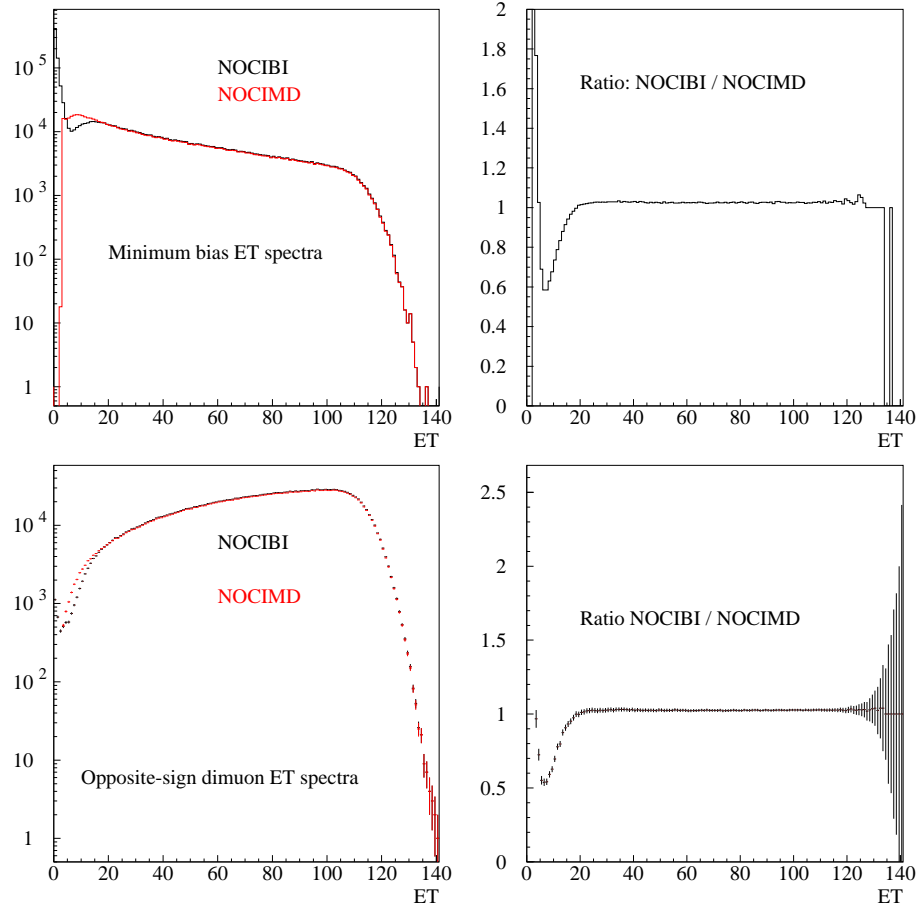


Figure 3.3: A comparison of the E_T spectra with *NOCIBI* and *NOCIMD* cuts. Top plots show the spectra obtained using BH trigger, whereas the bottom plots are the spectra obtained using dimuon trigger.

the absorber, the distance $Dtarg$ varies inversely with the track's momentum, so that the quantity P^*Dtarg is approximately independent of the momentum, and has a gaussian distribution shape. Therefore, $(P^*Dtarg)^2$ shows a χ^2 probability distribution. χ^2 probability is used as the cut variable instead but equivalently to P^*Dtarg , at 2% level for 2000 data.

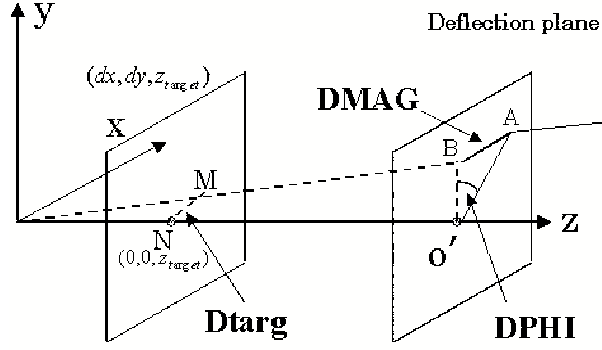


Figure 3.4: Definitions of $P \cdot Dtarg$, $DMAG$ and $DPHI$ variables.

3.5 The Minimum bias spectra analysis

Selected variables from μ DST are recorded into NTuples, corresponding to 4 periods:

- (Low Intensity runs) **part 1** 9718 – 9757 ;
- (Other runs) **part 2** *other runs* ;
- (Beginning runs) **part 3** 9115 – 9197 ;
- (End runs) **part 4** 9760 – 9827 ;

Figure 3.5 shows the Minimum Bias (BH Trigger) E_T spectra for the four periods. One can see in the figure 3.5 the difference at low E_T region for the runs part3, due to the lack of EMC *NICALO* information for these runs. This period is not kept in the analysis.

In order to compare the E_T spectra behaviors with respect to different periods, the ratios of part1, part3 and part4 to part2 are plotted in figure 3.7.

The same work is done for ZDC Trigger and Dimuon Trigger, as shown in figure 3.6 for the E_T spectra (part2). The ratios of ZDC Trigger E_T spectra during different periods are plotted in figure 3.8. Through comparing the plots between figure 3.7 and figure 3.8, one can conclude that, for this data-taking, the BH Trigger is more stable than the ZDC Trigger. So in the following analysis, we consider only the BH trigger minimum bias.

3.6 Study of E_T as a function of E_{ZDC}

After the pileup cuts, the interaction cuts, and the geometrical cuts for tracks, there are still some background events left, as seen from the figure 3.9 for Dimuon trigger and BH

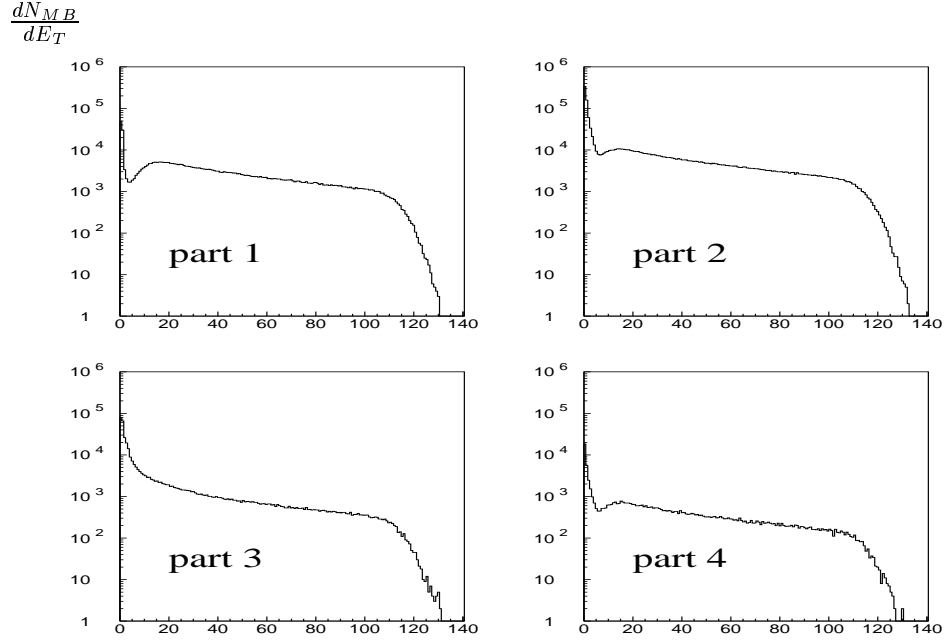


Figure 3.5: Minimum bias BH Trigger E_T spectra for four data taking periods.

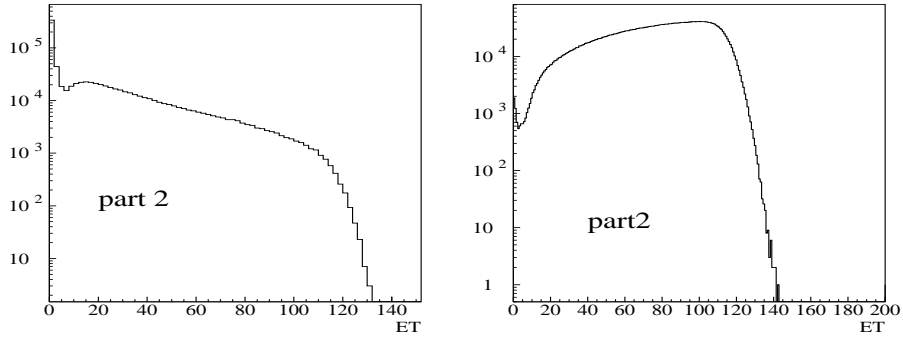


Figure 3.6: Minimum bias ZDC Trigger (left) and Dimuon Trigger (right) E_T spectra (any dimuons) for the data part 2

trigger. A diagonal cut (simplest “*Banana*” cut) is the selection of the events within a $E_T - E_{ZDC}$ band (corresponding to the approximate linear shape correlation between the NA50 electromagnetic and zero degree calorimeters).

This diagonal cut should not introduce any bias in the results, in particular:

- no effect on the ratio of dimuons to minimum bias, in particular at high E_T ;

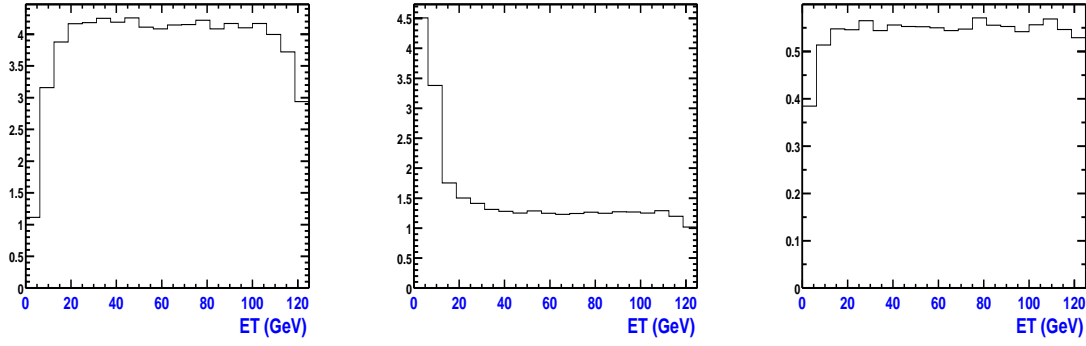


Figure 3.7: Ratios of E_T spectra (BH trigger) obtained from different data taking periods: Ratios of Part1(left), Part3(middle) and Part4(right) to Part2 .

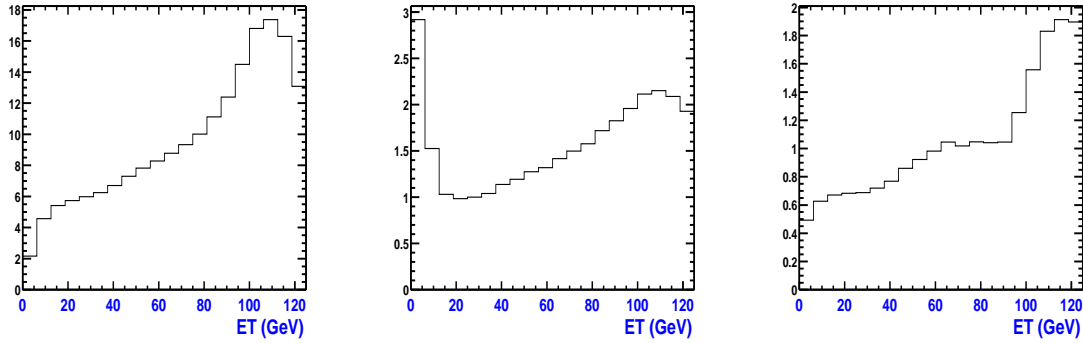


Figure 3.8: Ratios of E_T spectra (ZDC trigger) obtained from different data taking periods: Ratios of Part1(left), Part3(middle) and Part4(right) to Part2 .

- no effect on the shape of the minimum bias spectrum;

The first condition is a more critical question that will be addressed in the following section, where it will be verified that the banana cut does not introduce visible effect. For the second one we study the correlation between E_T and E_{ZDC} .

For this we perform a rotation in the $E_T - E_{ZDC}$ plane toward new variables $E'_T - E'_{ZDC}$ (figure 3.10). In each E'_T slice, the E'_{ZDC} spectrum can be approximated by a gaussian function. The mean and width values are extracted by fits and are plotted in Figure 3.11.

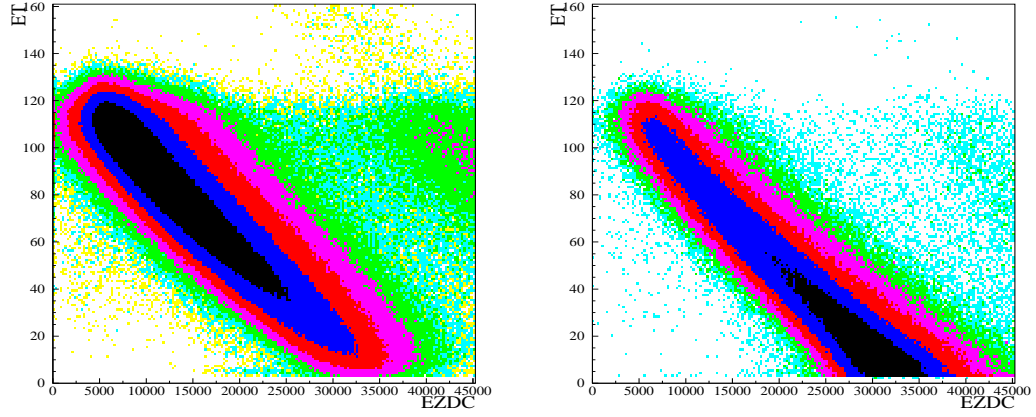
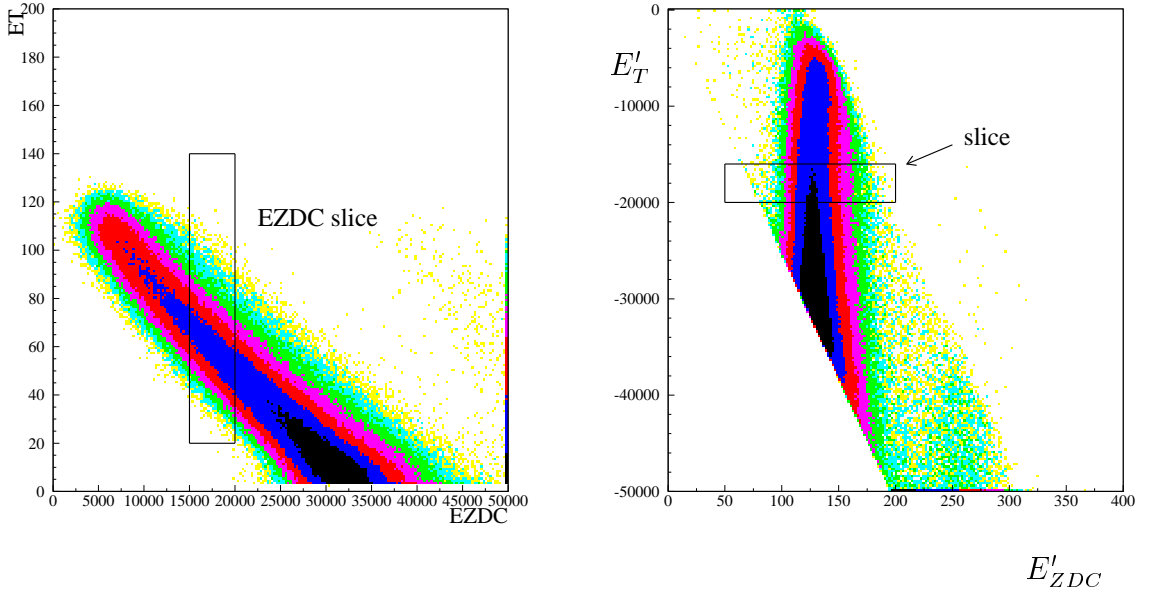


Figure 3.9: E_T - E_{ZDC} correlation for Dimuon trigger (left) and for BH trigger (right) with minimal event level ≥ 1 .



(a): before rotation

(b): after rotation

Figure 3.10: The illustration of the transformation procedure from E_T - E_{ZDC} plane (left) to E'_T - E'_{ZDC} plane (right).

From Figure 3.11, one can see that the E'_T - E'_{ZDC} correlation is wider at high intensity than at low intensity, furthermore the mean value is changing. This implies that a diagonal cut could create a bias in the minimum bias spectrum, if too strict.

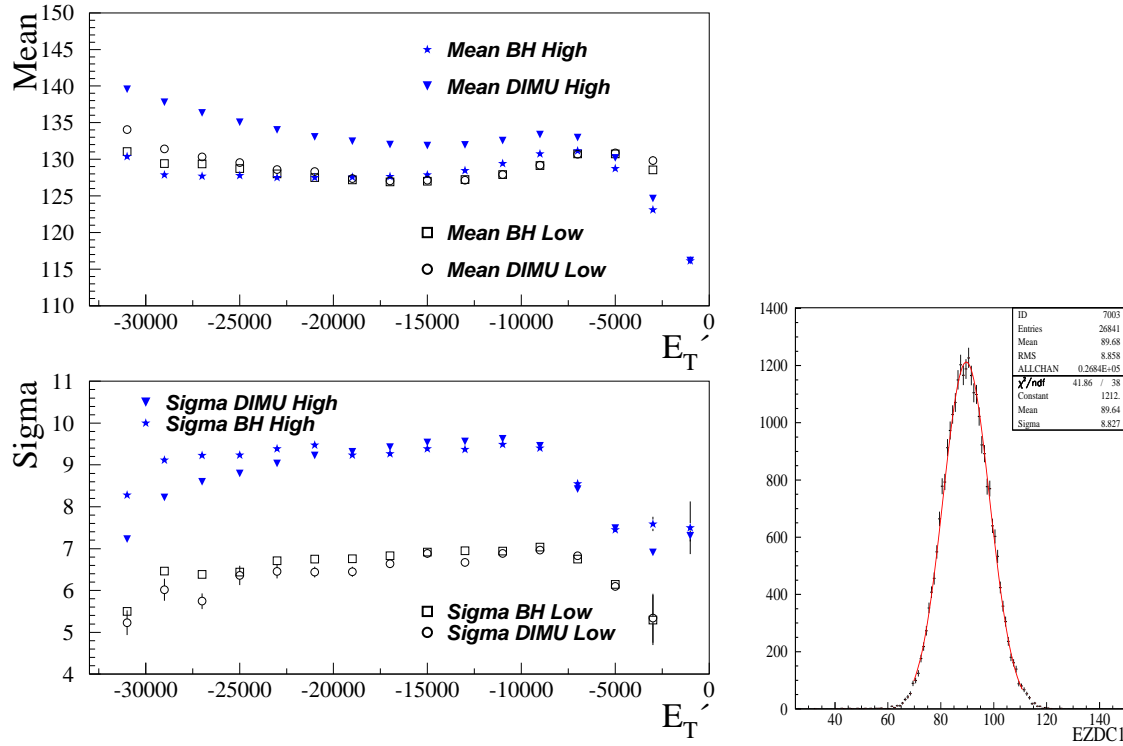


Figure 3.11: **Left:** The dependences on E'_T of the mean and the sigma of E'_{ZDC} spectrum for BH and Dimuon trigger of Low and High intensity runs separately. **Right:** A typical distribution of E'_{ZDC} .

After rotation E'_T is a mixture of E_T and E_{ZDC} , and this has the drawback of mixing different detector resolutions, so we go back to usual E_T . $\langle E_T \rangle$ and σ_{E_T} values extracted from fit to E_T spectra for various E_{ZDC} slices are presented in figure 3.12. Also in this view, except for most peripheral and central collisions where the edge effects occur, the apparent σ_{E_T} which is again a combined effect with E_{ZDC} , appears constant. A diagonal cut with parallel lines seems to be confirmed here to correspond to the E_T - E_{ZDC} correlation observed, with the condition of a loose cut in order not to significantly bias the minimum bias spectrum, since the E_T - E_{ZDC} correlation is not perfectly linear.

Finally, to determine the line of maximum correlation between the two variables E_T and E_{ZDC} , it is done with this rotation method. The variance of the values around the line of the maximum correlation is fitted with a gaussian function, the rotation angle is tuned by minimizing the gaussian width of the fit in the projection of the transverse axis.

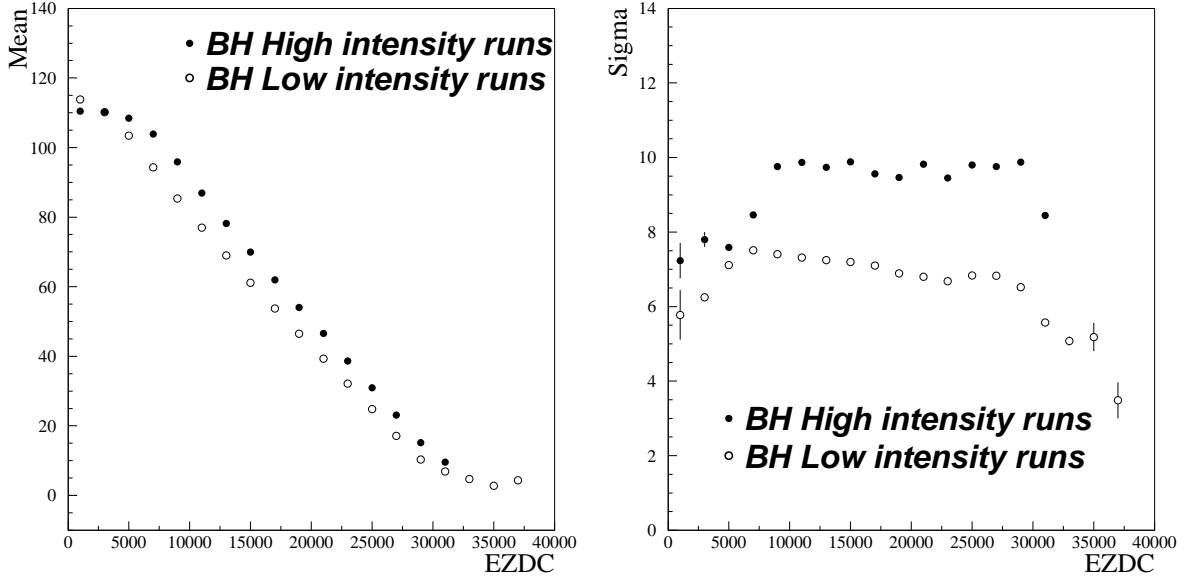


Figure 3.12: A dependence of $\langle E_T \rangle$ and σ_{E_T} on E_{ZDC} (minimum bias BH trigger) for low and high intensity runs.

Figure 3.13 shows the cut selected in the transverse axis of the E_T - E_{ZDC} correlation. The two lines are calculated to cut the gaussian tails with a 3σ in the E_T - E_{ZDC} plane, in order to determine the cut band. In this way, the relationship between the transverse neutral energy released E_T and the beam spectators energy E_{ZDC} in the acceptance window is expressed as [81]:

$$(102.2170 - 0.003693 \times E_{ZDC}) < E_T < (158.3892 - 0.003693 \times E_{ZDC}) . \quad (3.2)$$

3.7 Consistency of minimum bias analyses for dimuons

1996 and 1998 data have shown interesting suppression of the J/ψ production for very high E_T domain, above the knee. Reinteractions have been suspected of being the origin of the observation of an apparent rise of the ratio $J/\psi/MB$. This region is delicate since there is a strong exponential decrease, and that minimum bias trigger and muon pairs trigger could suffer different systematical effects (this is also true for other E_T regions). For the last data taken, in order to get a redundancy and to minimize potential differences between dimuon and minimum bias trigger, a second minimum bias trigger has been

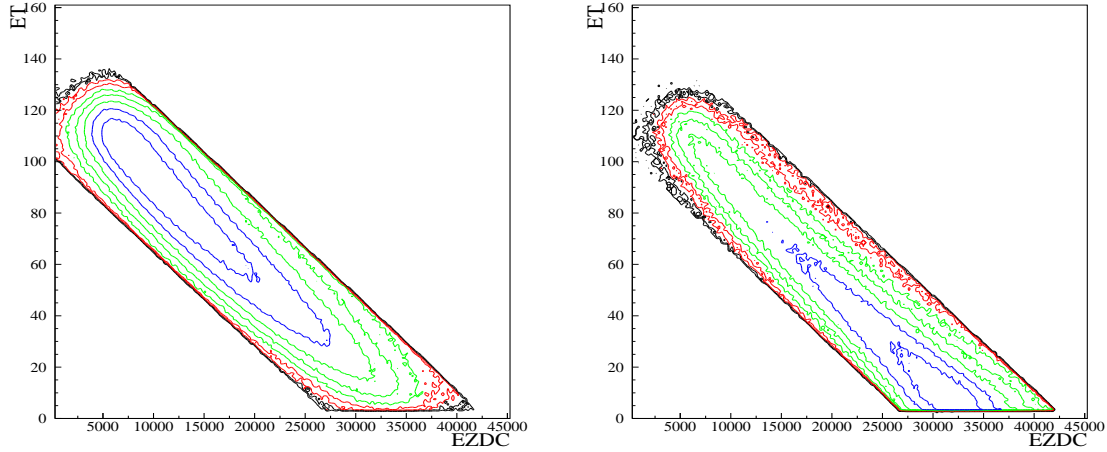


Figure 3.13: E_T - E_{ZDC} correlation after *Banana* cut, left Dimuon Trigger, right BH Trigger.

realized with the BH (beam hodoscope), and all the trigger have been re-timed thanks to the BH blades.

In order to track possible systematical effects between dimuons and minimum bias, we will perform an extensive comparison between the various muon pair productions divided by the minimum bias, as a function of E_T .

Such a consistency picture is a basic requirement for studying any multiplicity with respect to E_T . Every trend common to all muon pairs, independent of the muon sign or the pair mass, should indicate a potential bias in the minimum bias spectrum.

First we will look at this comparison, then to its sensitivity to cuts, then to run selection.

The ratios are studied for different events selection :

- *Banana* cuts presented in figure 3.14;
- $P^*Dtarg \leq 1.5 \sigma_{P^*Dtarg}$ cut;
- $Z_{vertex} \leq 50$ cm cut;

For convenience, the ratios considered here are $N_p/(MB * E_T^2)$, where N_p is the number of muon pairs (Like-Sign, Opposite-Sign and signal muon pairs of various masses), MB is the number of minimum bias events and E_T the average transverse energy.

The Figure 3.15 and Figure 3.16 show that after the knee ³, all the muon pairs including

³The edge of the resolution of E.M.C. and the same physical effects from the fluctuations of E_T at a given impact parameter b in NN collisions.

signal display similar behavior. It is independent of the low E_T behavior, since the Opposite-sign and Like-sign muon pairs have very different low E_T behaviors. Thus it is not linked to the re-interactions, which should otherwise introduce opposite effects in the high E_T behaviour.

So the only acceptable behavior here is the flatness. This is also consistent with a predominance of the E_T experimental resolution in the shape of the spectrum after the knee (see the section 3.11.1).

The observed increase for high E_T is not associated with banana cut: the same trend is visible for all considered cuts.

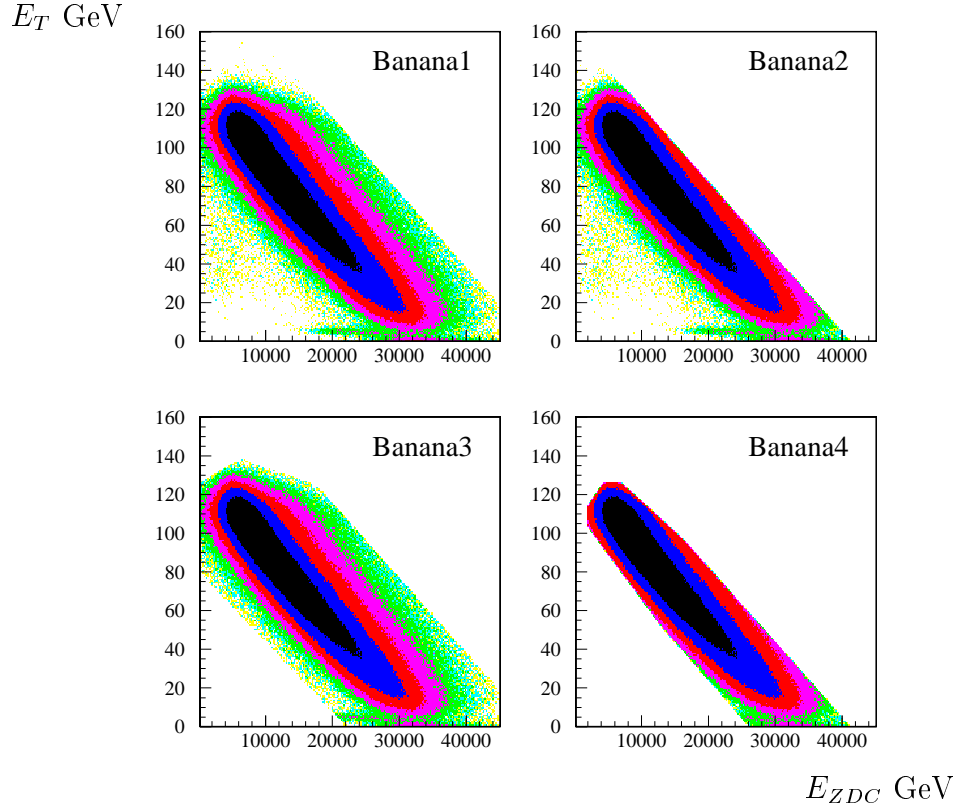


Figure 3.14: E_T - E_{ZDC} correlation for 4 different *Banana* cuts.

By using ONLY high intensity data of part2 and part4 (see figure 3.17 and 3.18), the Like-Sign dimuons, Opposite-Sign dimuons and Signal dimuons display a flat behavior after the knee. This shows that it is possible to select a subset of the runs in which the dimuon spectra display a regular flat tendency, and all the “multiplicities” – dimuon pairs from different sources divided by minimum bias have a reasonable regular shapes (see figure 3.17 and 3.18).

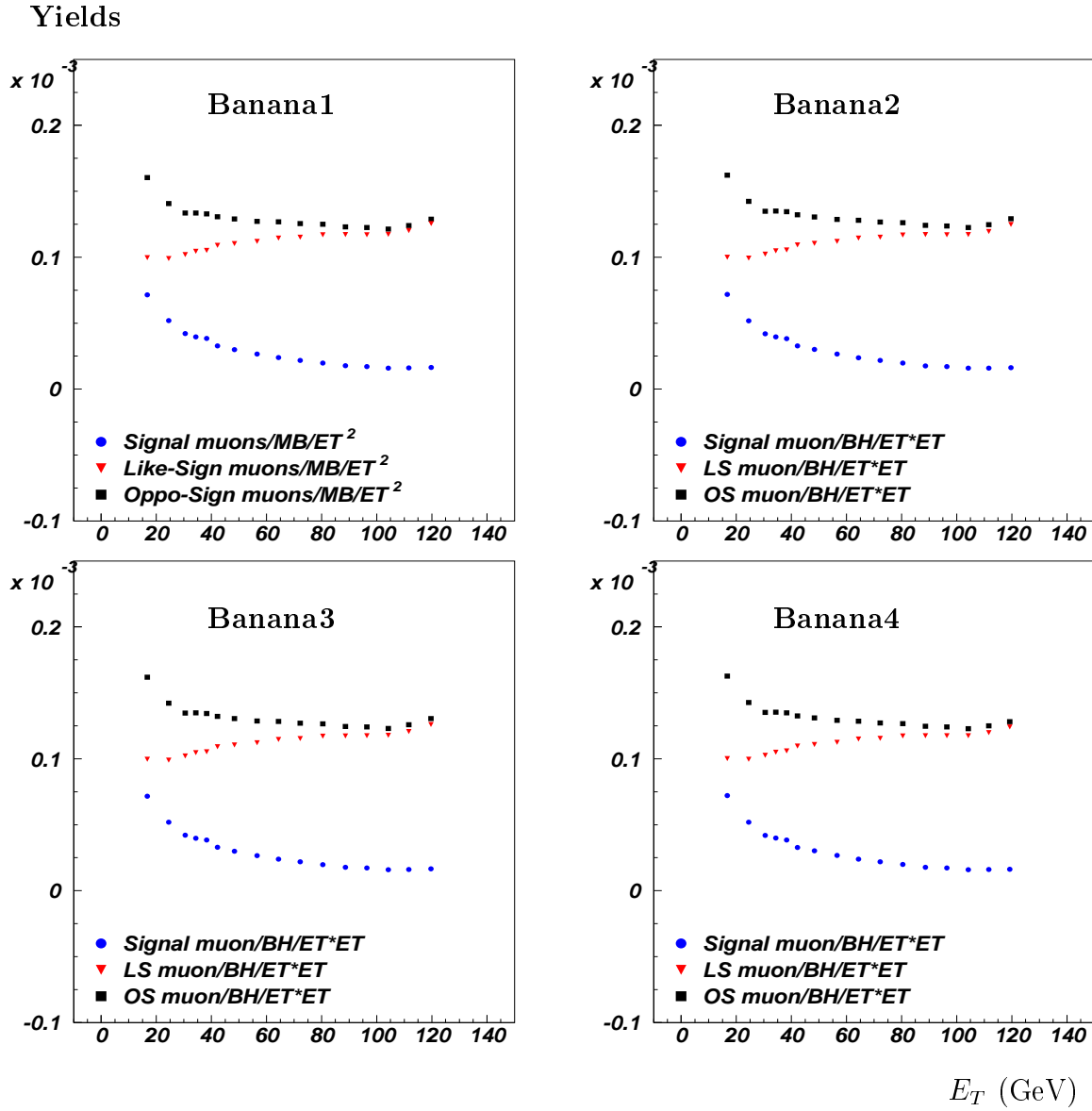


Figure 3.15: The yields of like-sign, opposite-sign and signal dimuon pairs as a function of E_T for four different *Banana* cuts (part 1,2,4 data).

From the analysis above, one can conclude that by using the data of part2 and part4, the ratio of dimuon to minimum bias display a regular flat tendency at high E_T . This is not sensitive to the different cuts. Finally, the data from part2 and part4 (high intensity) are chosen for the analysis.

Only dimuons without mass selection have been presented in the previous study, but

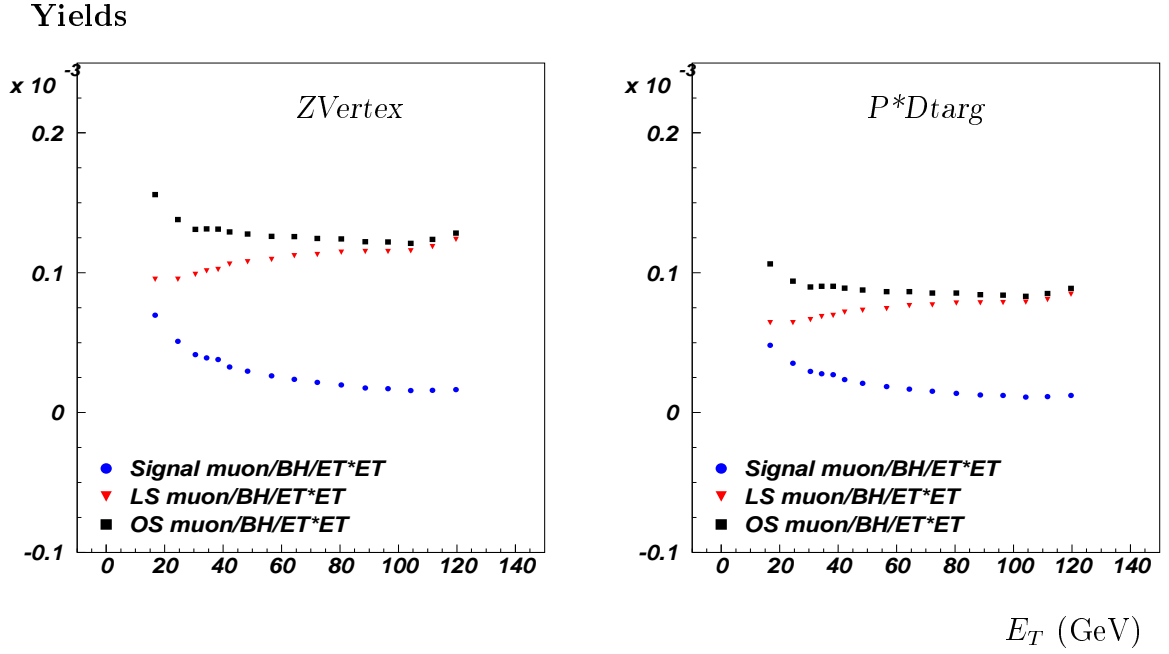


Figure 3.16: The yields of like-sign, opposite-sign and signal dimuon pairs as a function of E_T , after $ZVertex$ and P^*Dtarg cuts (part 1,2,4 data).

typical mass domains have also been considered, showing the same trend. Figure 3.19 shows the raw data results of ratios of J/ψ , ϕ and ω mass domains to minimum bias as a function of E_T for the chosen run selection. ω appears flat; ϕ shows a increase, and for J/ψ , an anomalous drop is seen for E_T around 50 GeV.

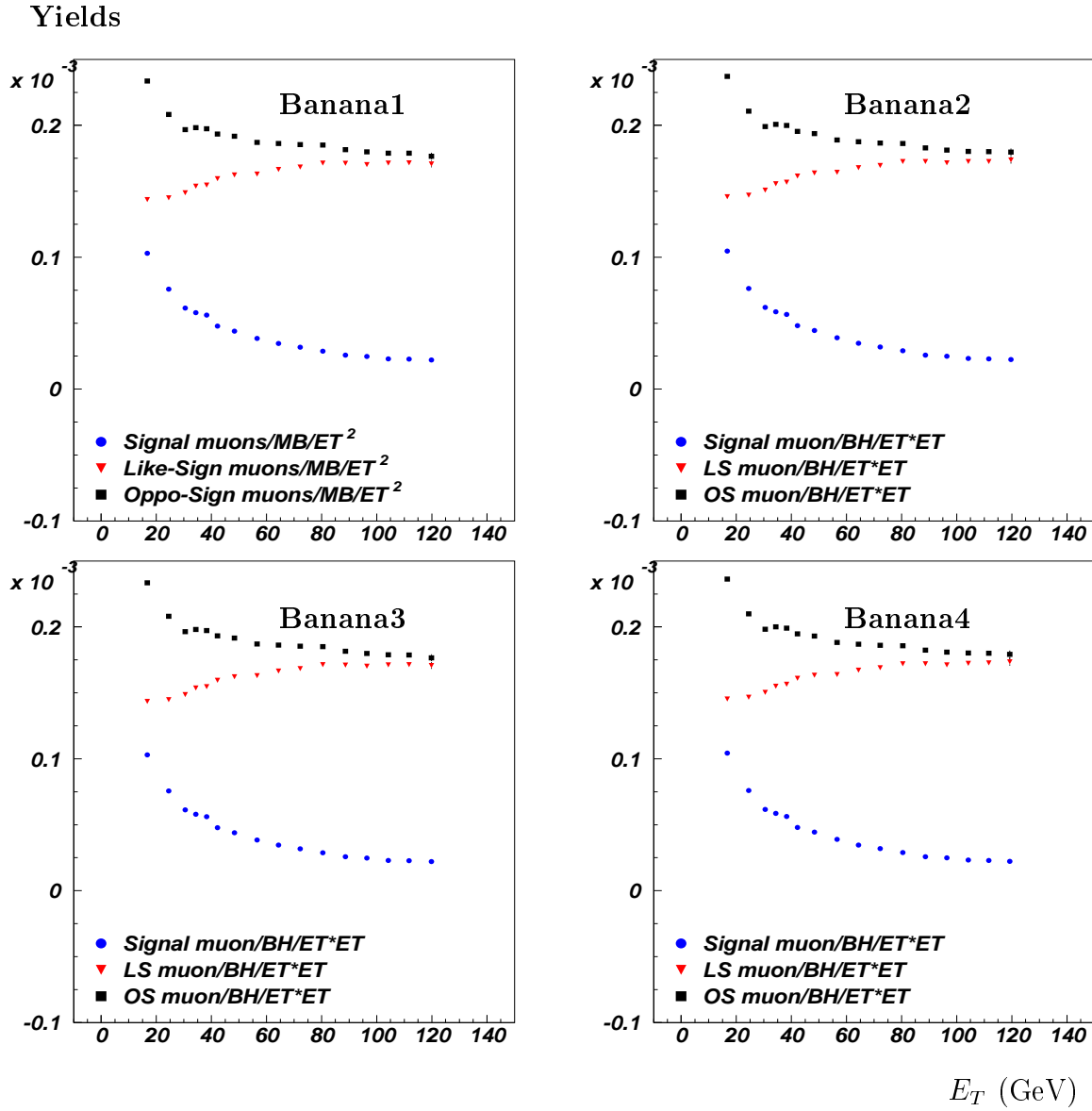


Figure 3.17: The yields of like-sign, opposite-sign and signal dimuon pairs as a function of E_T for four different *Banana* cuts (ONLY part 2,4 data).

3.8 Determination of efficiency corrections

The cuts on the data are performed in the order *PILEUP*, *NPARAS*, *NOCIMD*, *NICALO*, *T0J*, *NIZDC*, P^*D_{targ} (for Dimuon trigger) and *Banana*, as explained before. The different efficiency values calculated from the data are listed in the Table 3.1 for BH trigger

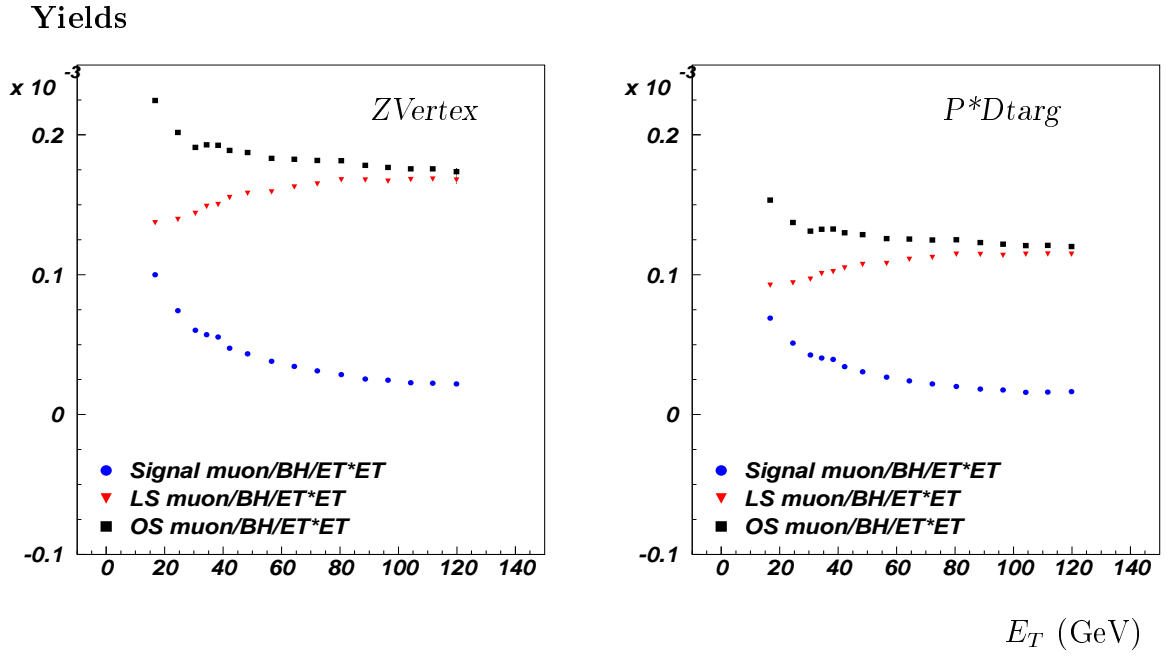


Figure 3.18: The yields of like-sign, opposite-sign and signal dimuon pairs as a function of E_T , after $ZVertex$ and P^*D_{targ} cuts (ONLY part 2,4 data).

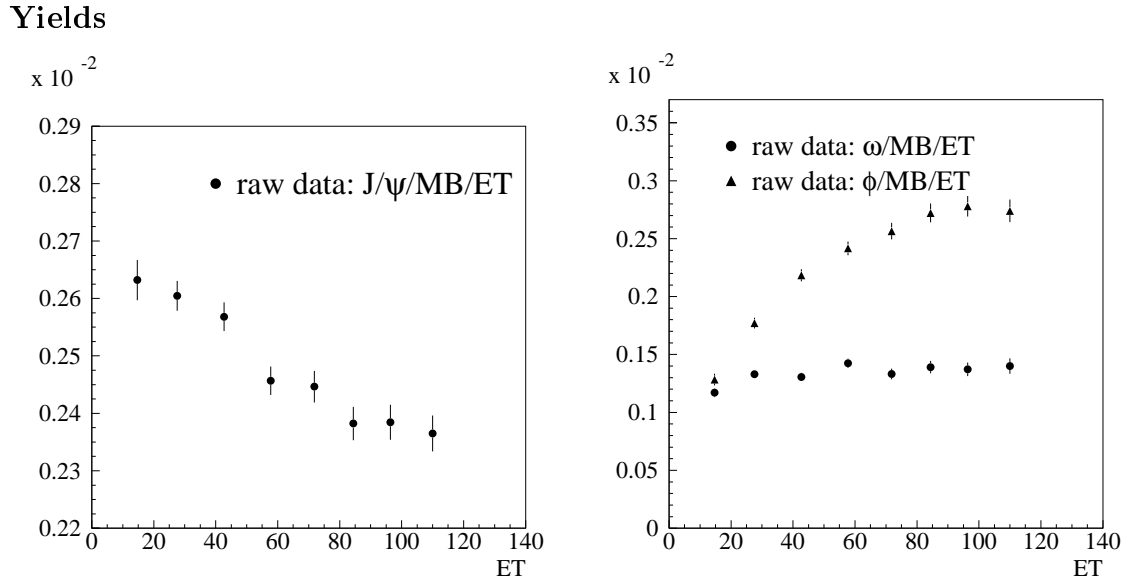


Figure 3.19: Raw yields of J/ψ , ϕ and ω (BH trigger minimum bias) as a function of E_T (GeV).

CUT	BH scaler	dimuons	minimum bias
ϵ_{DAQ}	0.96 ± 0.01		
ϵ_{PILEUP}	0.65 ± 0.02		
ϵ_{NPARAS}	0.964 ± 0.005		
ϵ_{NOCIMD}		0.97 ± 0.004	0.97 ± 0.004
ϵ_{NICALO}		0.864 ± 0.02	0.84 ± 0.02
ϵ_{T0J}		0.89 ± 0.02	0.97 ± 0.02
ϵ_{NIZDC}		0.998 ± 0.005	1.00 ± 0.005
ϵ_{Banana}		0.96 ± 0.005	0.96 ± 0.005
$\epsilon_{P*Dtarg}$		0.95 ± 0.005	
$\epsilon_{\mu\mu TRIG}$		0.92 ± 0.02	
ϵ_{Recons}		0.953 ± 0.013	

Table 3.1: Corrections applied to luminosity, dimuons or minimum bias, in order to take into account the signal rejection by background cuts.

and Dimuon trigger.

The various cuts used are aiming at removing backgrounds, like *NICALO*, *NOCIMD*, or removing biased events, like *PILEUP* or *NPARAS* cuts. But these cuts also reject part of the signal that we want to study, or modify the amount of incoming beam. Figure 3.20 displays the effect of these cuts on J/ψ events. For minimum bias triggers, the same quantity (fraction of remaining events after cut with respect to the number of events before the cut) is also displayed with *PILEUP* and *NPARAS* cuts. J/ψ mass domain is considered here as an attempt to estimate the effect of the cut on the signal, since some spurious sources as collisions in the entrance of the absorber does not lead to a dimuon signal with a correct mass, and inversely the J/ψ peak could be expected to contain mostly dimuons originating from the target.

The effect of *PILEUP* cut is very different for J/ψ and for minimum bias triggers. Minimum bias triggers display a 35% decrease in the lowest E_T bin, then a rather constant 53% decrease, for higher E_T . This peculiar trend is due to the fact that pile up events contains two incoming ions, and each of them has about 10% probability to interact in the target, producing a non “zero” transverse energy. So the effect on non interacting (zero) events is 35% whereas the effect on the interacting event is twice as important, i.e.,

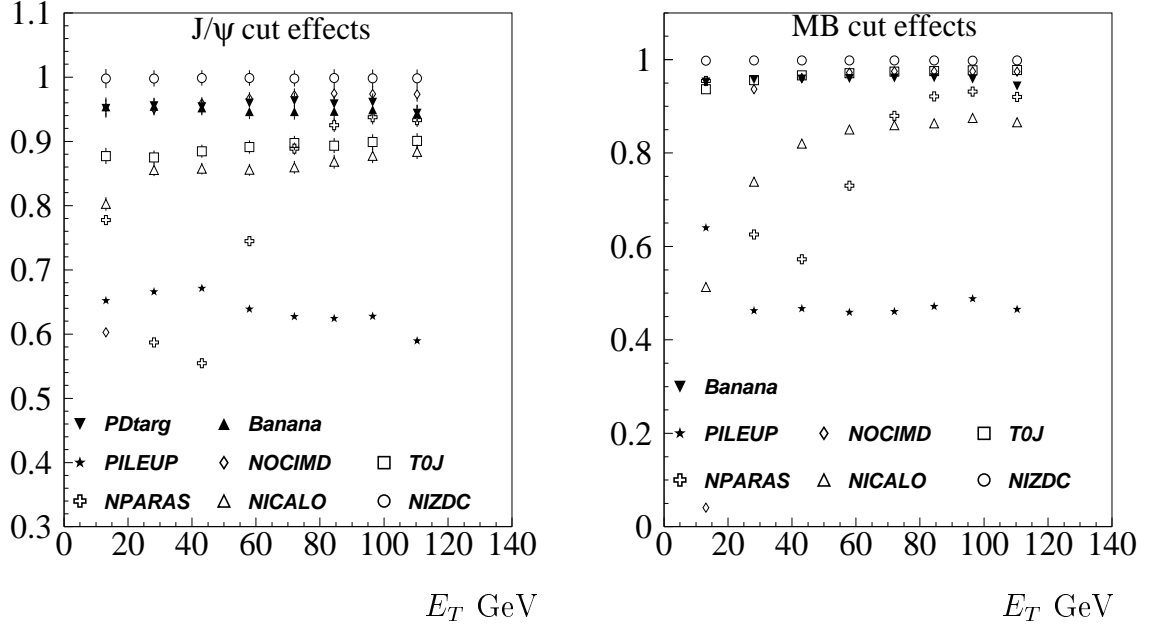


Figure 3.20: Left: the fraction of the raw J/ψ signal remaining after various cuts as a function of E_T ; Right: the fraction of minimum bias remaining after various cuts as a function of E_T .

$0.35 \times 2 / (0.35 \times 2 + 0.65) = 0.51$. This effect does not hold for J/ψ because it is a trigger.

Most of the cuts are weakly depending on the transverse energy, except for the *NPARAS* cut. These events, where only a fragment of Pb ion reaches the target region, must lead to lower average E_T , but what is seen here is not interaction in the target. The *NPARAS* events are associated to a bump in J/ψ E_T spectrum, visible in figure 3.21. What is the origin of this bump? One could imagine two possible origins: the E_T associated to particles produced in the BH, or associated to an interaction of the remaining fragment before the electromagnetic calorimeter. It is interesting to remark also that these events are associated with a E_T bump also for minimum bias events (see figure 3.1), so the “target” producing this transverse energy is not the normal target, which has only an interaction probability of 1/10. Looking at the figure 3.22 one observes that the J/ψ is displaced toward lower masses for the events cuts by *NPARAS*. This is the sign of an origin downstream from the target⁴. The fraction of events rejected by the *NPARAS* cut is 6.5% for the minimum bias, this shows that the threshold on the BHI

⁴In this case the dimuon is reconstructed with a vertex corresponding to the target, the opening angle of the muon pair is lowered with respect to the true value.

and BHI new used for this selection are very low, since only 2% interaction is expected in the 0.7 mm of quartz of the BH. The fraction of J/ψ rejected is much higher, 28%. This shows that the 2% interaction in the BH leads to a fragment that has quite 100% probability to interact, 10 times more than the non BH-interacted beam, leading to 20% of the J/ψ produced. Finally, there is no reason to take into account in the efficiency for the spurious J/ψ produced in the absorber, and we can check that at high E_T , rejection of J/ψ and minimum bias events are the same (see Figure 3.23), because they result from the random effect of this cut. The fraction of incoming ions rejected is then the only correction to apply, 6.5% on the total number of incoming ions (given by the scalers associated to each of the BH blades). The lifetime of the DAQ (4%) can also be taken into account as an effective decrease of the available beam.

NOCIMD cut is acting mostly at low E_T , for high E_T a 3% effect is observed, identical for J/ψ and minimum bias. *NICALO*, which is aiming at pile up of interaction in target, is in principle not useful here since full pile up rejection is performed. Nevertheless it can improve the BH efficiency for detecting pile up, and also reject additional background. In particular a background in the $E_T - E_{ZDC}$ region similar to the *NPARAS* spurious events, is rejected by *NICALO* (see Figure 3.2). The flatness of the *NICALO* rejection rate with E_T is indicating that this *NPARAS* contribution is not the dominant one, and the high E_T rejection rate is most probably a signal rejection, at the level of 12%.

Reconstruction efficiency, muon pair trigger efficiency and P^*Dtarg cut on muon track are only acting on dimuon trigger. The $T0J$ cut, rejecting events whose trigger signal has not been corrected by BH, has a more important effect for dimuon trigger than for minimum bias trigger. Figure 3.23 confirms that at high E_T , only the *PILEUP* and $T0J$ cuts lead to different results for J/ψ and for minimum bias.

Finally it is noteworthy that only these last four efficiencies will intervene in the multiplicities determinations, the others cancelling in the ratio between dimuon and minimum bias.

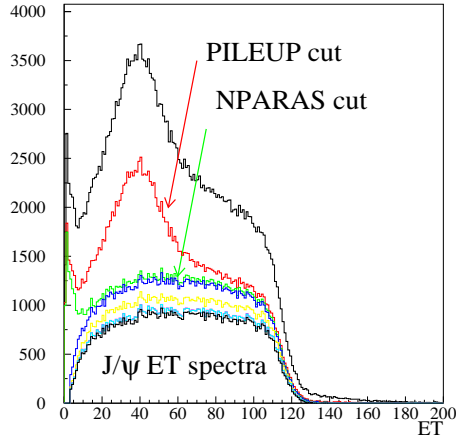


Figure 3.21: J/ψ transverse energy spectrum, before and after *PILEUP* and *NPARAS* cuts.

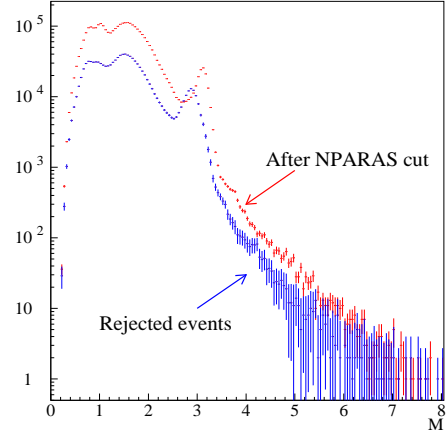


Figure 3.22: The dimuon mass spectrum rejected by the *NPARAS* cut and the remaining dimuons.

3.9 The prescaling of the minimum bias

In order to cope with the acquisition rate, the number of minimum bias events must be limited, to about 2×300 triggers per burst (~ 5 s). These triggers must then be prescaled by an important factor since the incoming Pb ion rate is about 8×10^6 incoming ions. For the BH triggers this is obtained in two complementary ways (see Figure 3.24):

- Only one BH blade is used in the BH trigger, this corresponds to typically 1/16 of the total intensity, with variations due to the beam profile at the BH level ;
- The BH blade logical signal is prescaled by an electronic module, typically 2^{14} (16384).

Finally the prescaling is nothing but the ratio between the sum of BH scalers, taking into account the lifetime of the acquisition, and the minimum bias triggers at the level of the micro-DST.

The efficiency of the prescaling electronic modules depends on the incoming intensity. The prescaling then has to take this into account, by an effective prescaling which is higher than the one chosen by the command. This is automatically taken into account by the ratio BH luminosity to BH minimum bias triggers when entering into RELMIC.

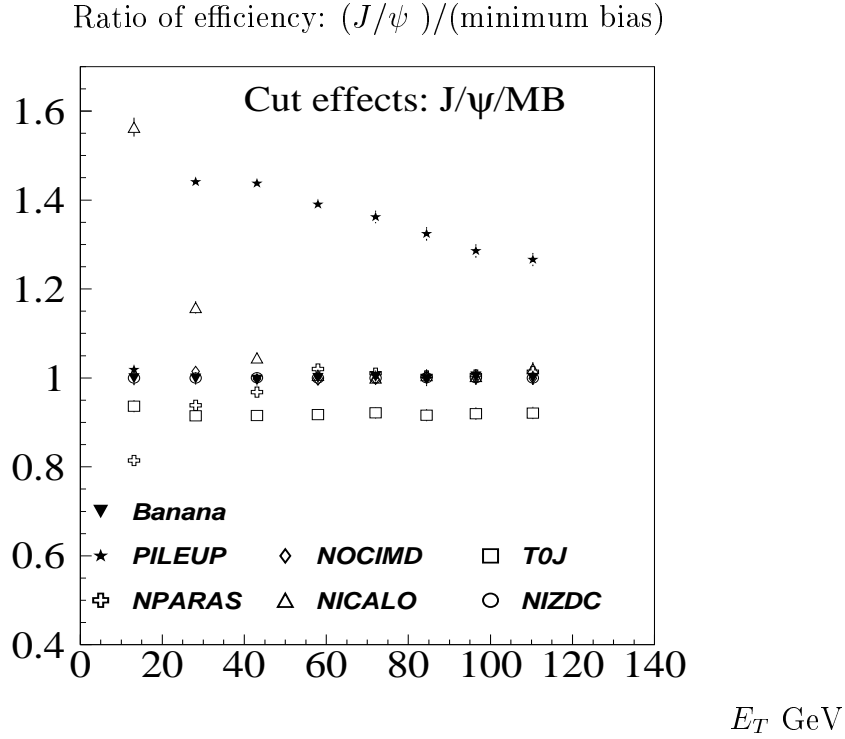


Figure 3.23: Ratio of J/ψ to Minimum bias efficiency as a function of E_T for different cuts.

3.10 Background subtraction

During the data acquisition, both the muon pairs with opposite charge and the muon pairs with the same charge are recorded. These later muon pairs originate from uncorrelated decays of pions and kaons, which are also producing a combinatorial background in the muon pairs with opposite charges. Like sign pairs are used to estimate these combinatorial muon pairs of opposite charge.

After the image cut, acceptances are similar for positive and negative charged muons, and one can consider, under some hypothesis [80]

$$N_{comb}^{\mu^+\mu^-} = 2\sqrt{N^{\mu^+\mu^+} N^{\mu^-\mu^-}}. \quad (3.3)$$

As described in section 2.4.4, the regular changing of the polarity of the magnet field contribute to minimize eventual systematic effects according to the muon's charge in a given field and then improves the image cut efficiency regarding the background

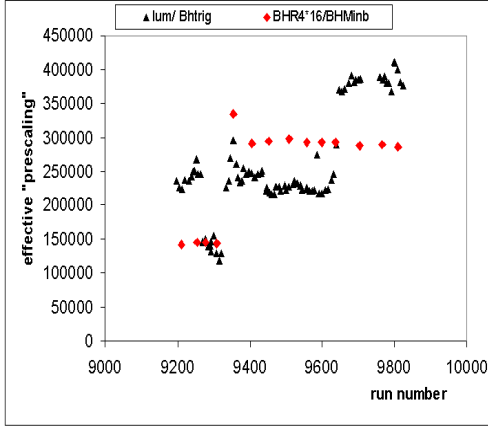


Figure 3.24: BH scalers of Only one BH blade and the BH blade logical signal prescaling versus run number.

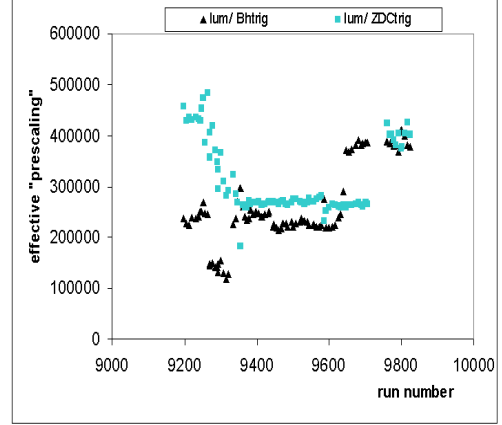


Figure 3.25: The ratio of Luminosity/BH and Luminosity/ZDC versus run number.

determination.

$$N_{Signal}^{\mu^+\mu^-} = N^{\mu^+\mu^-} - 2\sqrt{N^{\mu^+\mu^+}N^{\mu^-\mu^-}} \Big|_{\oplus} - 2\sqrt{N^{\mu^+\mu^+}N^{\mu^-\mu^-}} \Big|_{\ominus} , \quad (3.4)$$

is the signal of the correlated muon pairs $\mu^+\mu^-$ of the opposite charge, where $N^{\mu^+\mu^-}$ is the total number of measured $\mu^+\mu^-$ pairs, the subscript \oplus and \ominus indicate the sign of the spectrometer magnetic field.

For low multiplicities, systematic deviation occurs from the previous formula, and a correction factor R ($R \geq 1$) is introduced,

$$N_{Signal}^{\mu^+\mu^-} = N^{\mu^+\mu^-} - 2 R \sqrt{N^{\mu^+\mu^+}N^{\mu^-\mu^-}} \Big|_{\oplus} - 2 R \sqrt{N^{\mu^+\mu^+}N^{\mu^-\mu^-}} \Big|_{\ominus} . \quad (3.5)$$

In this analysis, we use:

$$R = 1.0 + 0.4/E_T . \quad (3.6)$$

The Figure 3.26 shows the dimuon mass spectra of the opposite-charge in low mass and high mass domains, and the combinatorial background events are superimposed in the same figure.

3.11 The centrality variables of the collision system

Experimentally, the centrality of the collisions is defined through the transverse energy. But physically speaking, a more effective centrality selection variable is the impact pa-

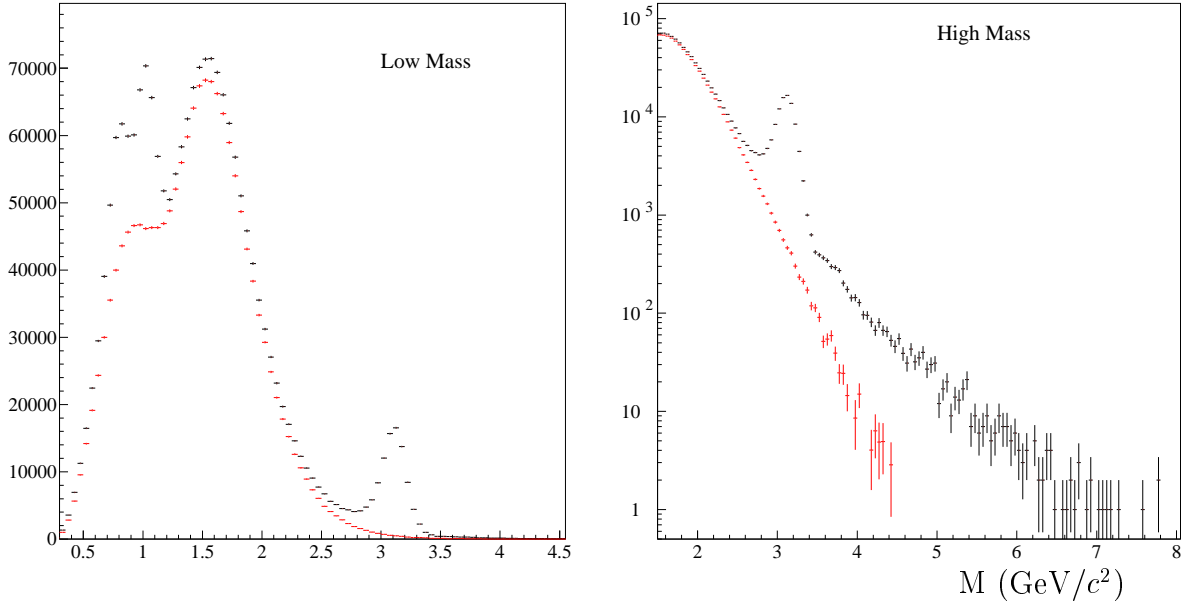


Figure 3.26: The invariant mass spectra of dimuons from the same events and the combinatorial background spectra (Eq.3.3) in low mass (*left*) and high mass (*right*) domains.

parameter b . Other related centrality variables are number of participants in the collision N_{part} and the number of nucleon-nucleon collisions N_{coll} . Being not directly accessible by the experiment, so they need a model to determine according to the measured E_T or E_{ZDC} .

3.11.1 Determination of N_{part} and N_{coll}

The measurable variables of the centrality of the collision in NA50 experiment are the transverse energy E_T , the energy deposited in the Zero Degree Calorimeter E_{ZDC} , and the multiplicity of the charged particles detected in the Multiplicity Detector. So the Glauber Model and “Wounded Nucleon Model” are used to determine the variables N_{part} , N_{coll} and b .

Glauber Model

The Glauber Model is a geometrical model describing the nucleus-nucleus collision process [1]. This model considers collisions at impact parameter b , where b defined as the minimal distance between the center of the projectile and target nuclei. Figure 3.27

gives a schematic diagram of a nucleus-nucleus collision. Nucleons of nucleus A travel along a straight line in the nucleus B and undergo one or multiple independent collisions with nucleons of B , if the distances between their trajectories is smaller than the distance corresponding to the nucleon-nucleon inelastic cross section σ_0 (30 mb). (see Figure 3.27).

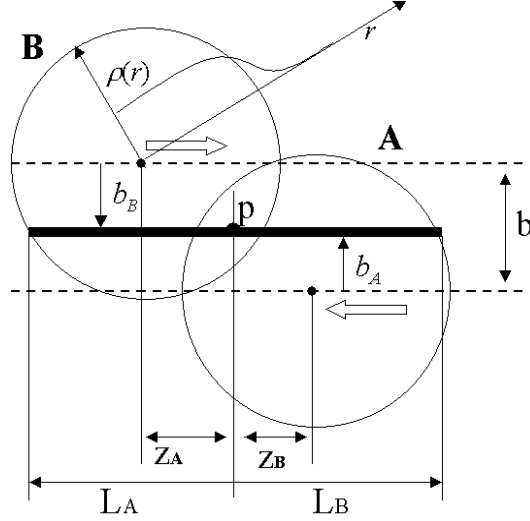


Figure 3.27: A schematic diagram of geometry of nucleus-nucleus collision.

The nuclear densities are described by Wood-Saxon parameterizations with 2 or 3 parameters (2pF or 3pF, depending on the nuclei [82])

$$\rho(r) = \frac{\rho_0}{1 + \exp(r - r_0)/C} \quad (3.7)$$

where r is the distance to the center of the nucleus, r_0 , C , ρ_0 are obtained from the electron-nuclei scattering experiments. Wood-Saxon distribution is plotted in Figure 3.28.

We determine the number of collisions thanks to a Monte Carlo calculation.

They can also be determined analytically. The probability that a nucleon inside of the nucleus A collides with a nucleon inside of the nucleus B , separated by the distance \vec{s} in the transverse plane to the collision axis AB , and with an impact parameter \vec{b} , is:

$$T_{AB}(\vec{b})\sigma_0 = \int d^2s \int \rho_A(\vec{s}, z_A) dz_A \int \rho_B(\vec{b} - \vec{s}, z_B) dz_B \sigma_0 \quad (3.8)$$

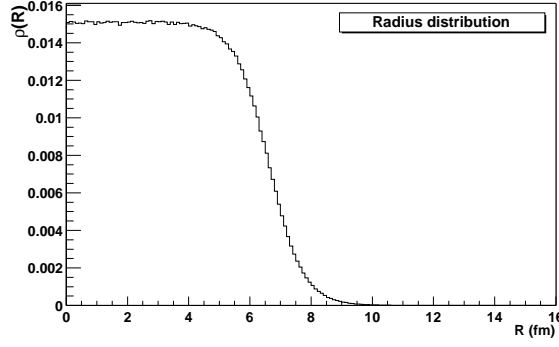


Figure 3.28: Wood-Saxon distribution with $\rho_0=0.169 \text{ fm}^{-3}$, $r_0=6.62 \text{ fm}$, $C=0.549 \text{ fm}$, normalized .

where $T_{AB}(\vec{b})$ is the nucleon density per normalized surface units, for an given impact parameter \vec{b} , i.e. $T_{AB}(\vec{b})$ is a thickness function of the nuclei A and B in the transverse plane, with $\int T_{AB}(\vec{b}) d^2b = 1$.

The probability $P_n(\vec{b})$ that n nucleon-nucleon collisions occur is described by a binomial function. For a given impact parameter \vec{b} ,

$$P_n(\vec{b}) = \frac{(AB)!}{n!(AB-n)!} [T_{AB}(\vec{b})\sigma_0]^n [1 - T_{AB}(\vec{b})\sigma_0]^{AB-n}. \quad (3.9)$$

The inelastic cross section for the event production is the summation of the probability that there is at least one nucleon-nucleon collision, given by,

$$\frac{d\sigma_{AB}}{d^2b} = \sum_{n=1}^{AB} P_n(\vec{b}) = 1 - [1 - T_{AB}(\vec{b})\sigma_0]^{AB} \approx 1. \quad (3.10)$$

The mean number of collisions $\langle n(\vec{b}) \rangle$ is given by,

$$\langle n(\vec{b}) \rangle = \sum_{n=1}^{AB} n P_n(\vec{b}) = \sigma_0 AB T_{AB}(\vec{b}). \quad (3.11)$$

Thus, demanding at least one collision, gives a mean number of nucleon-nucleon collisions, $N_{coll}(\vec{b})$,

$$N_{coll}(\vec{b}) = \frac{\sum_{n=1}^{AB} n P_n(\vec{b})}{\sum_{n=1}^{AB} P_n(\vec{b})} \approx \langle n(\vec{b}) \rangle = \sigma_0 AB T_{AB}(\vec{b}), \quad (3.12)$$

where $\sum_{n=1}^{AB} P_n(\vec{b}) = 1$.

Wounded Nucleon Model

The number of nucleons that have participated into the AB collision, N_{part} , can be calculated through the “Wounded Nucleon Model” [83], which is also used in the Glauber Model formalism. Within this model, N_{part} can be obtained as a function of the impact parameter, but it can also be related to the directly measured quantities, for instance, the transverse energy E_T released in the collision.

The average number of the participant nucleons in a AB collision is,

$$N_{part} = N_{part}^A + N_{part}^B. \quad (3.13)$$

Thus, at a given impact parameter b , N_{part} is given by,

$$\begin{aligned} N_{part} = & A \int d^2s \int \rho_A(\vec{s}, z_A) dz_A \left(1 - (1 - \sigma_0 \int \rho_B(\vec{b} - \vec{s}, z_B) dz_B)^B \right) + \\ & B \int d^2s \int \rho_B(\vec{s}, z_B) dz_B \left(1 - (1 - \sigma_0 \int \rho_A(\vec{b} - \vec{s}, z_A) dz_A)^A \right). \end{aligned} \quad (3.14)$$

Practically in the MC calculation, any nucleon suffering a collision is counted as a participant nucleon.

The “Wounded Nucleon Model” considers that the average multiplicity of the particles produced in the collisions is proportional to the number of nucleon participants. The transverse energy E_T^0 measured in the experiment is proportional to the number of π^0 s produced. If each of the participant nucleon produces secondary hadrons with the average number N_h , and each of these hadrons carries a mean transverse energy q_h , then each participant contributes $q \equiv q_n N_h$ to the total transverse energy produced in the collision. The mean E_T at a given impact parameter \vec{b} is

$$\langle E_T \rangle(\vec{b}) = q N_{part}(\vec{b}), \quad (3.15)$$

where q is the average transverse energy per participant.

Both the number of participant nucleon at a given impact parameter \vec{b} and the transverse energy produced by each participant in the collision can fluctuate. These are considered as gaussian fluctuations with σ_{E_T} (see Equation 3.19), such that the dispersion [75] is:

$$\sigma_{E_T}^2 = a q^2 N_{part}(\vec{b}), \quad (3.16)$$

where a is a dimensionless parameter and will be given hereafter. This E_T fluctuations come from both the physical fluctuations of the transverse neutral energy at a given impact parameter and the electromagnetic calorimeter detector’s resolution. One can also write the relationship

$$\frac{\sigma_{E_T}}{E_T} = \frac{\sqrt{a q}}{\sqrt{E_T}}. \quad (3.17)$$

The E_T resolution is about 14% at $E_T = 20$ GeV, 6.2% at $E_T = 100$ GeV.

Fit to the Min. Bias spectrum

Experimentally, the a and q parameters can be obtained from a fit to the minimum bias transverse energy spectrum⁵ resulting from all AB collisions $d\sigma^{MB}/dE_T$,

$$\frac{d\sigma^{MB}}{dE_T} \propto \int d^2b P(E_T, \vec{b}) \sigma_{AB} \quad (3.18)$$

where $P(E_T, \vec{b})$ is the probability of measuring a transverse energy E_T in a collision at a given impact parameter \vec{b} , described by a gaussian function,

$$P(E_T, \vec{b}) = \frac{1}{\sqrt{2\pi} a q^2 N_{part}(\vec{b})} \exp\left(-\frac{(E_T - q N_{part}(\vec{b}))^2}{2(a q^2 N_{part}(\vec{b}))}\right). \quad (3.19)$$

Figure 3.29 (a) shows the fit to the Minimum Bias E_T spectrum, one can obtain the average transverse energy $q = 0.2858$ GeV and $a = 1.342$, while the Glauber MC finds average transverse energy $q = 0.284$ GeV, and the comparison between the experimental and Glauber MC minimum bias is also plotted in Figure 3.29 (b) .

Another advantage of the Glauber MC is to determine the total inelastic cross section of Pb+Pb collisions⁶, which obtains $\sigma^{Pb+Pb} = 7106.97$ mb. Figure 3.30 shows the cross section spectrum as a function of the impact parameter extracted from the Glauber MC. This is obtained by using the p-p cross section of 30 mbarn. A higher cross section for p-p should have led to a higher total cross section through an increase of the peripheral Pb-Pb interactions.

The formula [62] :

$$\sigma^{Pb+Pb} = 68.8(A^{1/3} + B^{1/3} - 1.32)^2, \quad (3.20)$$

gives $\sigma^{Pb+Pb} = 7606$ mb, which is comparable with the value from the Glauber MC.

3.11.2 Equivalent variables of centrality measurement

The equivalent centrality variable values E_T , b , N_{part} , and N_{coll} are computed and listed in the Table 3.2, corresponding to the 9 transverse energy intervals, with $1.5 \leq M_T \leq 3.2$ GeV/ c^2 for Pb+Pb collisions. The first and second E_T bins are determined by Glauber Model.

⁵program adapted from Bernard Chaurand

⁶An inelastic Pb+Pb collision is defined as the collisions with at least one inelastic nucleon-nucleon collision.

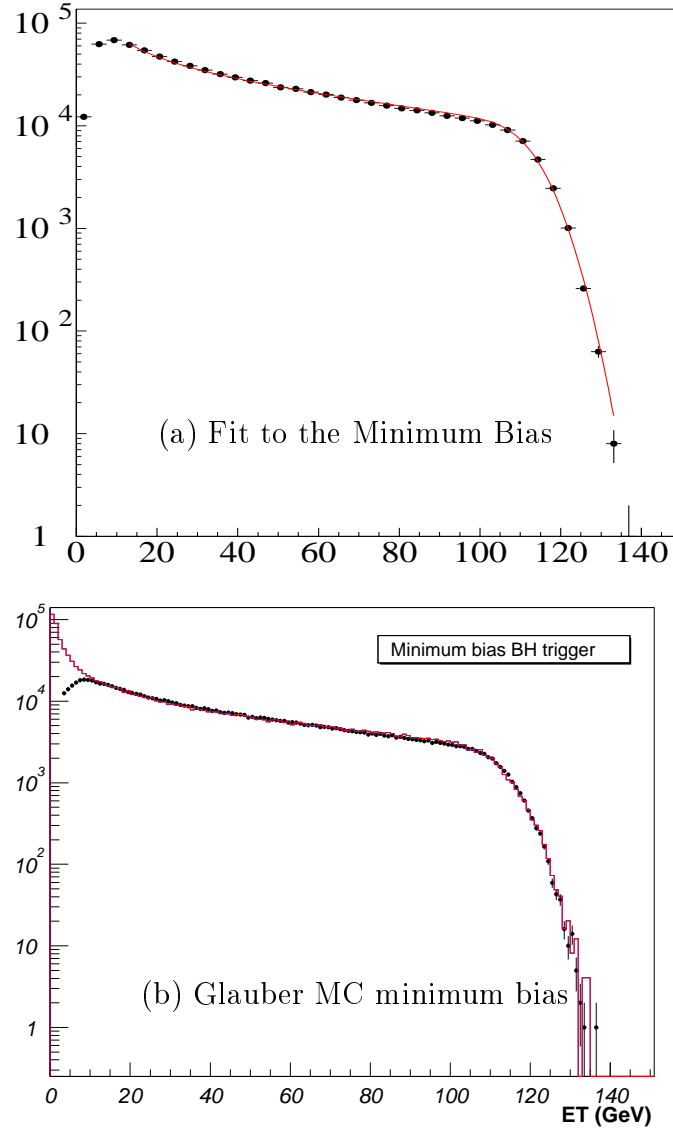


Figure 3.29: (a) Fit to the Minimum Bias E_T spectrum; (b) Comparison with the E_T spectrum obtained within Wounded Nucleon Model.

3.11.3 Centrality selection: E_T or E_{ZDC} ?

Experimentally, the centrality of AB collisions is measured either by the transverse neutral energy released (E_T), or by the beam spectators' energy (E_{ZDC}) due to the fact that the impact parameter is not directly accessible. Is one of these observables more sensitive

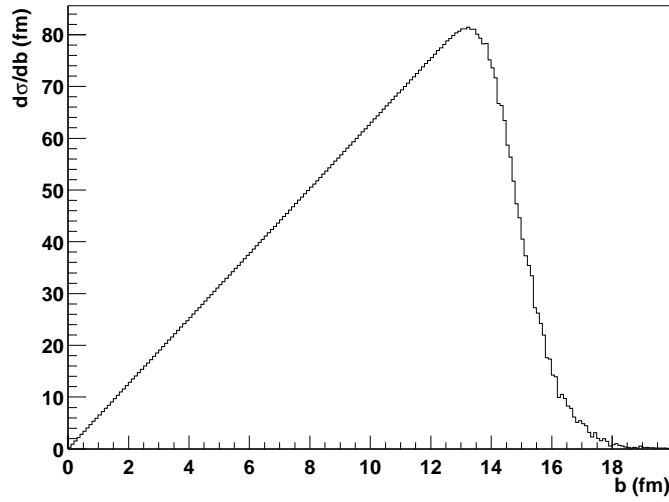


Figure 3.30: The cross section $d\sigma/db$ as a function of the impact parameter b calculated within the Glauber MC (unnormalized) .

E_T Interval (GeV)	$\langle E_T \rangle$ (GeV)	N_{part}	N_{coll}	b (fm)	centrality (%)
0 - 10	3.43	12	11	13.0	100.0
10 - 20	14.72	52	66	10.7	62.08
20 - 35	27.57	97	149	9.2	48.81
35 - 50	42.70	149	263	7.8	34.38
50 - 65	57.73	202	389	6.4	24.07
65 - 78	71.80	251	516	5.2	16.13
78 - 90	84.36	295	637	4.1	10.64
90 - 102	96.33	337	752	3.0	6.48
> 102	109.96	385	894	0.9	3.02

Table 3.2: The values of equivalent relationship for E_T , N_{part} , N_{coll} and b and centrality selection (%) in 9 E_T intervals.

to the centrality ?

In order to answer it, we use this Glauber Model Monte-Carlo to simultaneously reproduce the correlations between E_T , E_{ZDC} and b . As explained in section 3.11.1, the E_T spectrum is presented in Figure 3.29. For E_{ZDC} , it is the energy released by

the projectile spectator fragment. In a peripheral collision, only few nucleons undergo an interaction, the number of spectator nucleons is large, and a large amount of energy is released in ZDC detector. In a central collision, it goes to the contrary, E_{ZDC} is much smaller. In a real experiment, one should take into account also some participant nucleons plus part of secondary particles emitted in a collision. So with a certain impact parameter b , the average E_{ZDC} energy is the sum of two contributions, a dominate one $E_{ZDC}^{spect}(b)$, who is proportional to the number of spectator nucleons N_{spect} , plus another contribution $E_{ZDC}^{part}(b)$, proportional to the number of participant nucleons [75]:

$$\begin{aligned}
 \langle E_{ZDC}(b) \rangle &= E_{ZDC}^{spect}(b) + E_{ZDC}^{part}(b) \\
 &= 158 \times N_{spect}(b) + \alpha \times N_{part}(b) \\
 &= 158 \times \left(208 - \frac{N_{part}(b)}{2} \right) + \alpha \times N_{part}(b)
 \end{aligned} \tag{3.21}$$

where 158 GeV is the energy per spectator nucleon and the second term $\alpha \times N_{part}(b)$ is the energy released in ZDC detector by the participant nucleons and the secondary particles ($\alpha = 5.67$). The relationship between $N_{spect}(b)$ and $N_{part}(b)$ is given by Glauber Model. For a given impact parameter b , the E_{ZDC} values are fluctuating with a gaussian distribution, because of the experimental resolution of the ZDC detector and the fluctuations of $N_{part}(b)$. The width $\sigma_{E_{ZDC}}$ is given by Equation 2.3 (in section 2.3.3). (In this equation, the first two terms are related to the resolutions of the detector and the third term takes into account the smearing of the signals).

Thus we obtain the correlations of E_T - b and E_{ZDC} - b as shown in Figure 3.31, also in this figure, the correlations of E_T - E_{ZDC} are shown. The top-bottom evolutions in Figure 3.31 are obtained by improving the E_T and E_{ZDC} “resolutions” by 50%. One can see from this figure that when the experimental resolutions are high enough, the correlations between E_T , E_{ZDC} and b become more tightly. For E_T - E_{ZDC} , the correlation becomes a line, due to the strong relationship between them in the model. In contrast E_T - b and E_{ZDC} - b correlations, are still presenting a broad correlated zone, this is not related to detectors resolutions, but from the fluctuations of $N_{part}(b)$ and $N_{spect}(b)$, at a given fixed impact parameter b .

Figure 3.32 shows the correlations of $\langle E_T \rangle - \langle b \rangle$ and $\langle E_{ZDC} \rangle - \langle b \rangle$ before and after improving the “resolutions” in the Monte-Carlo. This figure is aiming at checking the sensitivity of impact parameter b in given E_T or E_{ZDC} domains, when changing the resolutions. From this figure, E_T is more selective to the centrality b than E_{ZDC} for peripheral collisions, since it is not biased. For central collisions, the both are biased when changing the resolutions. So if the detector’s resolutions are ideally high, the E_T

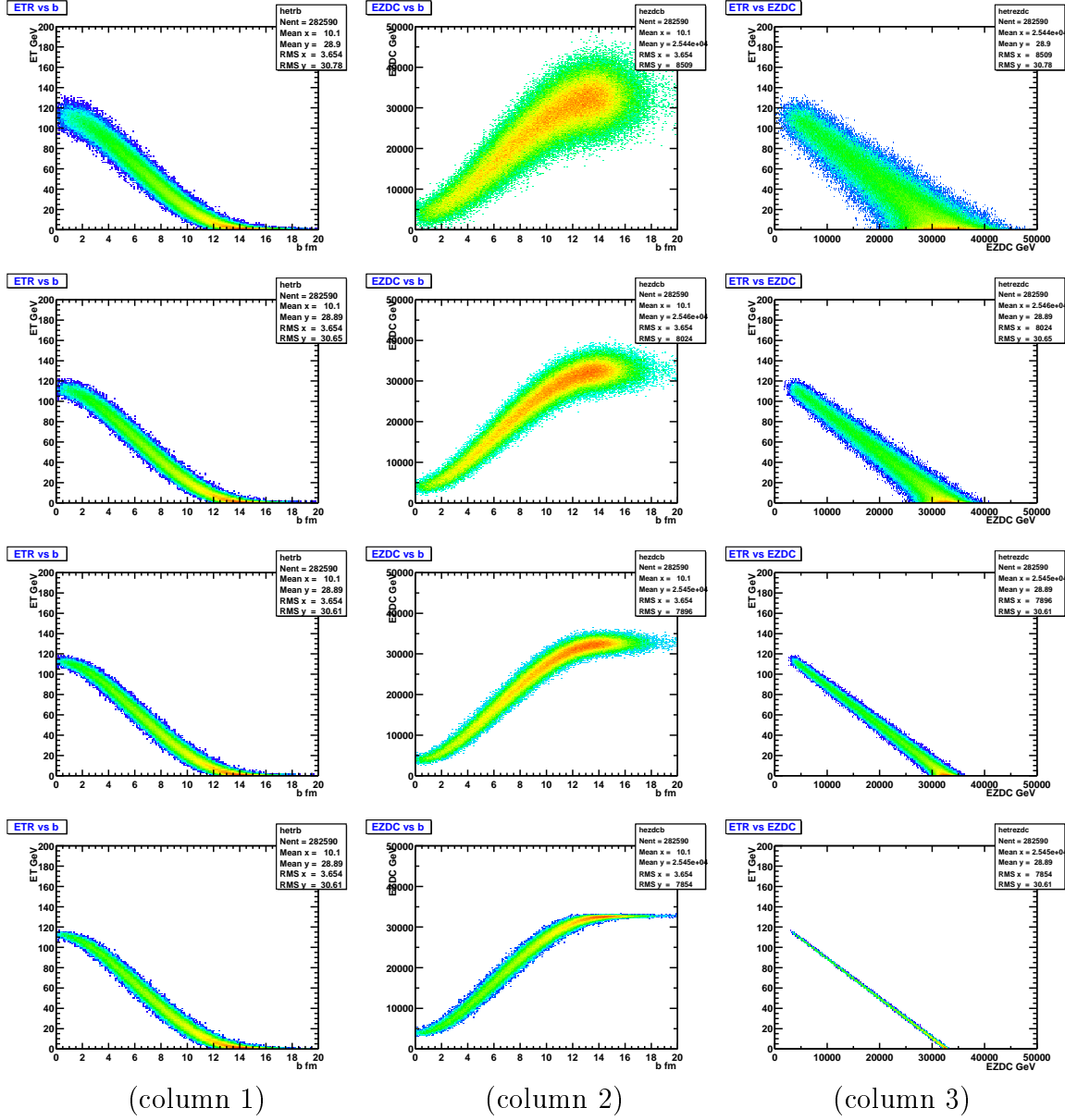


Figure 3.31: E_T - b (column 1), E_{ZDC} - b (column 2) and E_T - E_{ZDC} (column 3) correlations for σ_{E_T} and $\sigma_{E_{ZDC}}$ resolutions increasing from top to bottom.

and E_{ZDC} are both effective centrality selection variables for central collisions, we can not differ that E_T is better than E_{ZDC} to estimate the centrality selection, or on the contrary. In this analysis, E_T is used to select the centrality of Pb-Pb collisions.

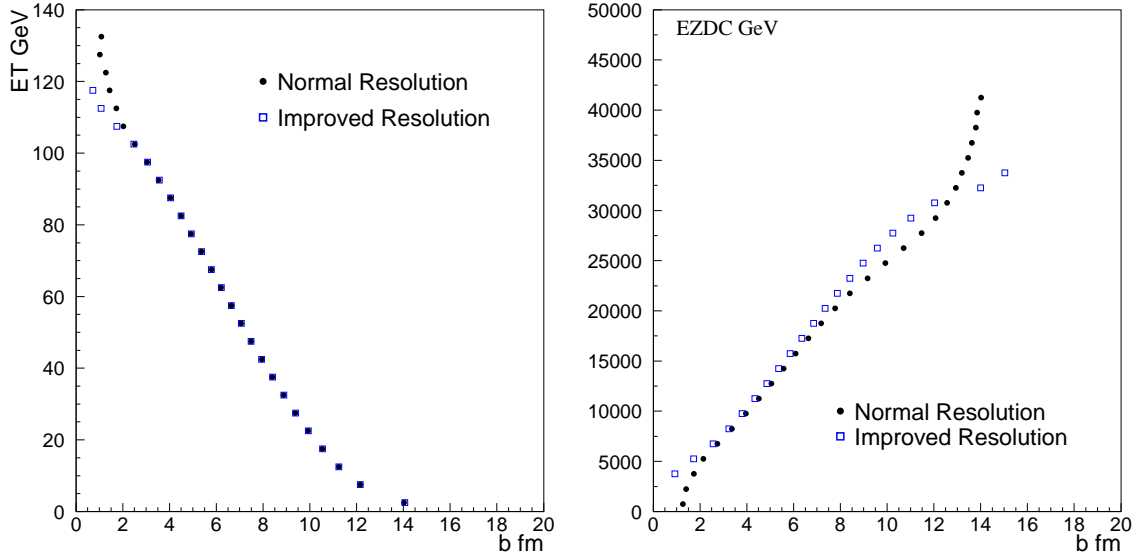


Figure 3.32: The dependence of $\langle E_T \rangle$ on b (left) and $\langle E_{ZDC} \rangle$ on b (right) for normal and improved resolutions.

3.12 Application to J/ψ analysis

J/ψ study is not the subject of this thesis but it is interesting to look at the global E_T behaviour obtained, with more E_T points and using the results of the glauher calculation made in section 3.11.1.

J/ψ study relies on *Drell-Yan* production as a reference, the later being a well studied process of the annihilation of one quark from the target-nucleon with another quark from the projectile-nucleon. *Drell-Yan* yield is observed to be proportional to the number of nucleon-nucleon collisions, but with a very low statistics. It is then difficult to study J/ψ /*Drell-Yan* ratio because of the fluctuations from *Drell-Yan* yield. As recalled in section 3.7, the ratio $J/\psi/MB$ has been considered in previous studies, allowing more E_T bins in the analyses. The number of nucleon-nucleon collisions N_{coll} should also make an alternative to *Drell-Yan*.

For J/ψ we will as previously consider the number of dimuons in a mass region, but also for the sake of completeness we perform a fit using usual ingredients.

3.12.1 The fit to the mass spectra

For the invariant masses above $2 \text{ GeV}/c^2$ in NA50, opposite-sign muon pairs originate from the production of J/ψ , ψ' , *Drell-Yan* process, $D\bar{D}$ pairs and the “background” from the π and K decays (see section 3.10). The number of signal events is deduced from the raw number of N^{+-} of the opposite-sign muon pairs after subtraction of the background:

$$N_{Signal}^{+-} = N^{+-} - 2 \sqrt{N^{++}N^{--}}, \quad (3.22)$$

where N^{++} (resp. N^{--}) is the number of pairs with two positive (resp. negative) charged muons. The mass distribution functions of different components are used the same shapes as described in [8], called standard parametrization.

In order to determine the number of events from J/ψ decay, the analysis is done as briefly described hereafter. The dimuon mass spectrum above $2.9 \text{ GeV}/c^2$ is fitted to a sum of all the contributions accounting for the continuum. The fit procedure of four steps is performed with the function

$$\frac{dN^{+-}}{dM} = N_{J/\psi} \frac{dN_{J/\psi}}{dM} + N_{\psi'} \frac{dN_{\psi'}}{dM} + N_{DY} \frac{dN_{DY}}{dM} + N_{D\bar{D}} \frac{dN_{D\bar{D}}}{dM} + \frac{dN_{BCK}}{dM}, \quad (3.23)$$

by using the parametrizations given in [8].

1. We fit the like-sign muon pairs to determine the background, in order to avoid the empty bin content than directly subtract the background by using equation 3.22. Then the background is subtracted according to the like-sign functions [84] in the mass range $2.1 \leq M \leq 3.6 \text{ GeV}/c^2$.
2. Fit the mass spectra by the sum of the background, J/ψ , ψ' and *Drell-Yan* contributions in the mass range $M > 3.05 \text{ GeV}/c^2$. The background is fixed from the step 1. The free parameters are normalization of $N_{J/\psi}$, $N_{\psi'}$, N_{DY} , the mass $M_{J/\psi}$ and width $\sigma_{J/\psi}$. For ψ' , its mass is related to the mass of J/ψ , and the width is considered to be same as J/ψ resonance. This fit step is aiming at find the mean values of the mass and width of J/ψ and ψ' shape.
3. Fit with the sum of background, J/ψ , $D\bar{D}$ pairs, *Drell-Yan* contributions in the mass range $2.2 \leq M \leq 2.6 \text{ GeV}/c^2$. Also the background is fixed from the step 1, the J/ψ and *Drell-Yan* are fixed from step 2. The only free parameter is the normalization $N_{D\bar{D}}$. This fit is to determine the $D\bar{D}$ normalization.
4. Fit with the sum of background, J/ψ , ψ' , *Drell-Yan* and $D\bar{D}$ pairs in the mass range $M > 2.9 \text{ GeV}/c^2$. In this final step fit, the background is fixed from the step

1, $D\bar{D}$ is fixed from step 3. There are 3 free parameters of the normalization $N_{J/\psi}$, $N_{\psi'}$, N_{DY} . The mass and width of the J/ψ and ψ' shape are fixed from step 2.

This 4-step fit procedure is done for all the E_T bins. As an example, the fitted mass spectrum is plotted in Figure 3.33.

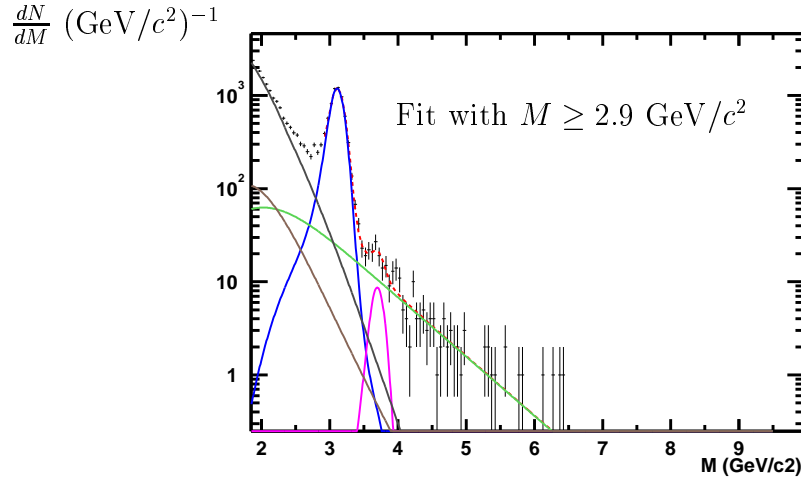


Figure 3.33: Fitted dimuon invariant mass spectrum for Pb-Pb collisions at 158 A GeV (2000 data).

3.12.2 J/ψ minimum bias behavior

The preliminary results of J/ψ E_T spectrum and $J/\psi/MB/N_{coll}$ as a function of E_T are plotted in Figure 3.34, where MB is the number of minimum bias events. Results presented here are unnormalized. From this figure, $J/\psi/MB/N_{coll}$ result shows J/ψ yield is continuously decreasing per nucleon-nucleon collision at high E_T region.

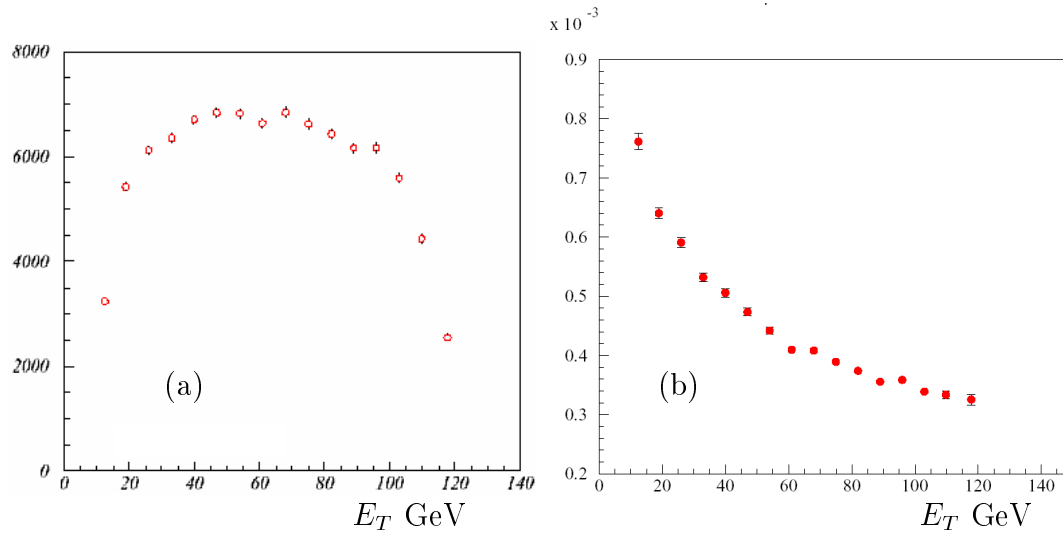


Figure 3.34: Left: E_T spectrum of J/ψ events; Right: unnormalized J/ψ multiplicity per number of collisions versus E_T for Pb–Pb collisions at 158 A GeV (2000 data).

Chapter 4

Monte-Carlo Simulation

4.1 The physical generation of DIMUJET

The Monte-Carlo simulation of the physical processes who contribute to the dimuon mass spectrum is done by using the code DIMUJET. The ρ , ω and ϕ resonances were considered, as well as a phenomenological continuum resulting from a set of processes such as Dalitz decays of the pseudo-scalars η and η' and the vector-meson ω , the *Drell-Yan* process and the semi-leptonic decays of $D\bar{D}$ pairs. The generation is based on kinematical distributions of the muon pair: the invariant dimuon mass M , the transverse dimuon mass M_T , defined as $\sqrt{M^2 + P_T^2}$, (or transverse momentum P_T), the dimuon rapidity y , the azimuthal angle φ , and the variables of the muons in the Collins-Soper reference frame azimuthal angle φ_{CS} and polar angle Θ_{CS} . The kinematic domains considered, which includes the experimental acceptance domain, are: the mass domain $0.5 < M < 3 \text{ GeV}/c^2$, the transverse mass domain $M_T > 1.3 \text{ GeV}/c^2$, the rapidity domain $-0.25 < y < 1.25$ and the polar angle $-0.8 < \cos \Theta_{CS} < 0.8$.

The generated muons are then propagated through the experimental apparatus, taking into account the energy loss and multiple scattering (occurring mainly in the absorber), and the geometry of the detector. The accepted events are subsequently reconstructed by using the same reconstruction program as for the experimental data, the DIMUREC code. They are submitted to the same cuts as the experimental data. The obtained mass distributions are used to extract the different components in the experimental mass spectra, and also to calculate the corresponding acceptances.

4.2 The generation function

4.2.1 Generation on mass distribution

The dimuon mass spectrum is the sum of the resonances ρ , ω and ϕ that decay into dimuons,

$$\rho, \omega, \phi \rightarrow \mu^+ \mu^-$$

and of a physical continuum which is the joint contribution of Dalitz decays (also called internal conversion processes):

$$\eta, \eta' \rightarrow \gamma \gamma^* \rightarrow \gamma \mu^+ \mu^-,$$

$$\omega \rightarrow \pi^0 \gamma^* \rightarrow \pi^0 \mu^+ \mu^-,$$

of semi-leptonic decays of $D\bar{D}$ pairs (*i.e.*, open charm processes mainly):

$$D^+ \rightarrow \bar{K}^0 \mu^+ \nu_\mu,$$

$$D^- \rightarrow K^0 \mu^- \bar{\nu}_\mu,$$

$$D^0 \rightarrow K^- \mu^+ \nu_\mu,$$

$$\bar{D}^0 \rightarrow K^+ \mu^- \bar{\nu}_\mu,$$

and of the *Drell-Yan* process (who is the annihilation of one quark from the target-nucleon with another quark from the projectile-nucleon, and has been better defined for high masses $M > 3 \text{ GeV}/c^2$):

$$q\bar{q} \rightarrow \gamma^* \rightarrow \mu^+ \mu^-.$$

The ρ , ω and ϕ resonances are simulated by using the classical Breit-Wigner functions, with the mass peaks and widths presented in the table 4.1, given by the Particle Physics Data Booklet 2002 [85]:

$$BW_r = \frac{\Gamma_r^2/4}{(M - m_r)^2 + \Gamma_r^2/4}, \quad (4.1)$$

where $r = \rho, \omega, \phi$. This simulation uses the classical Breit-Wigner shapes for vector mesons ω and ϕ . The ρ resonance being very broad, its description of the mass spectrum as a classical Breit-Wigner shape is not sufficient [64] (see section 1.4.3). So a phase space factor $1/M^4$ is considered in the ρ mass region.

For the continuum, accounting for the sum of all the processes that contribute to it, an effective empiric parametrization, namely a decreasing exponential shape, is used, following the phenomenologic *Drell-Yan* scaling distribution:

$$\frac{1}{M^3} \exp(-\tau/\sqrt{s}),$$

component	M_R MeV	Γ_R MeV	Generation interval of mass GeV/ c^2
ρ	771.1 ± 0.9	149.2 ± 0.7	$0.311 \leq M \leq 1.229$
ω	782.57 ± 0.12	8.44 ± 0.09	$0.757 \leq M \leq 0.808$
ϕ	1019.456 ± 0.020	4.26 ± 0.05	$0.887 \leq M \leq 1.150$
continuum			$0.25 \leq M \leq 3.0$

Table 4.1: Characteristic variable domains for components.

which is extended to:

$$\frac{dN}{dM} \propto M^{-\alpha} \exp(-M/\beta) , \quad (4.2)$$

where α and β are the adjusting parameters.

The parameters and the characteristic variable domains used for the component simulation are listed in Table 4.1 .

4.2.2 Generation on rapidity distribution

The distribution of rapidity y in the collision system is simulated by using a gaussian function :

$$\frac{d\sigma}{dy} \propto \exp\left(-\frac{y^2}{2\sigma_0^2}\right) . \quad (4.3)$$

The distribution is centered at $y = 0$, because the colliding system is symmetrical. The value $\sigma_0 = 1.4$ is used in the simulation, the used generation window is $-0.25 < y < 1.25$.

4.2.3 Generation on transverse mass distribution

The generation on transverse mass distribution is done according to a Bessel function:

$$\frac{dN}{dM_T} \propto M_T^2 K_1(M_T/T) , \quad (4.4)$$

where $M_T = \sqrt{M^2 + P_T^2}$, is the dimuon's transverse mass, K_1 is a Bessel function, the parameter T is the inverse slope of the distribution versus M_T , also called "effective temperature". In this simulation, $T = 230$ MeV is used, the chosen window is $0 \leq P_T \leq 5.0$ GeV/ c , and $M_T \geq 1.3$ GeV/ c^2 . When $M_T \gg T$, the formula 4.4 can be approximated by :

$$\frac{dN}{dM_T} \propto M_T^{3/2} \exp(-M_T/T) ;$$

and another formula is often used to determine the temperature T :

$$\frac{dN}{dM_T} \propto M_T \exp(-M_T/T) ,$$

leading to about 10 MeV lower T value.

4.2.4 Generation on $\cos \Theta_{CS}$ and φ_{CS} distribution

Figure 4.1 shows a schematic diagram of Collins-Soper reference frame, with Θ_{CS} and φ_{CS} .

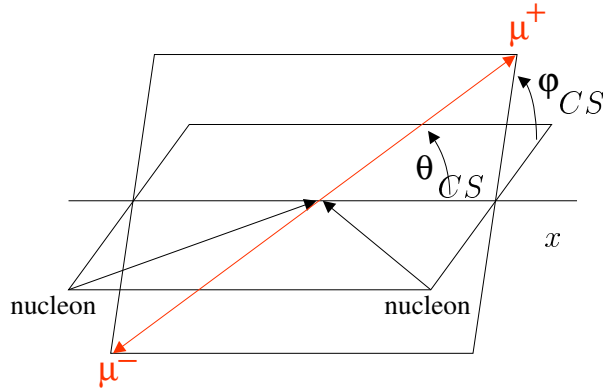


Figure 4.1: The definitions of Collins-Soper angles in the Collins-Soper reference frame.

The distribution on $\cos \Theta_{CS}$ is simulated with the shape:

$$\begin{aligned} \frac{d\sigma}{d \cos \Theta_{CS}} &\propto \text{constant} && \text{for resonances ,} \\ &\propto 1 + \cos^2 \Theta_{CS} && \text{for continuum ,} \end{aligned} \quad (4.5)$$

the chosen generation window is $-0.8 \leq \cos \Theta_{CS} \leq 0.8$, a little bit wider than the window of the angular acceptance of NA50 ($-0.5 \leq \cos \Theta_{CS} \leq 0.5$). The distribution as a function of the azimuthal angle φ_{CS} is generated as :

$$\frac{dN}{d\varphi_{CS}} = \text{constant} . \quad (4.6)$$

4.3 Accepted dimuon distributions

In Figure 4.2, one can see the plots of the generated distributions as a function of the mass, the transverse mass, the rapidity and the $\cos \Theta_{CS}$ of the produced dimuons based on the generation functions described before. Also in this figure, the accepted dimuon distributions are presented. Figure 4.3 shows the simulated mass spectra for ρ , ω , ϕ and continuum.

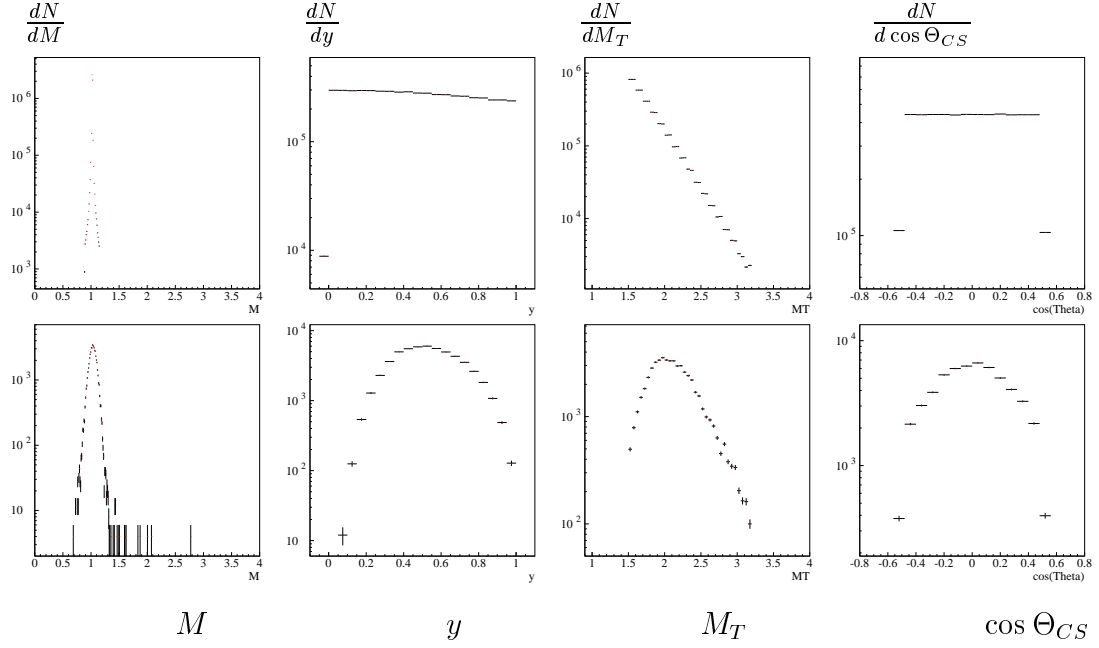


Figure 4.2: Dimuon invariant mass, rapidity, transverse mass and $\cos \Theta_{CS}$ distributions for Generated (top plots) and reconstructed (bottom plots) events. The vertical scale are in arbitrary units.

4.4 The acceptances in M_T slices

4.4.1 The acceptance as a function of M_T

The different acceptances A_R for the resonance R in a given transverse mass interval ΔM_T^i , as the ratio of the reconstructed events to the generated events in the same kinematical domains (thus they partially contain different events), are calculated as,

$$A_R = \left(\frac{N_R^{\text{Reconstructed Events}}}{N_R^{\text{Generated Events}}} \right), \quad (4.7)$$

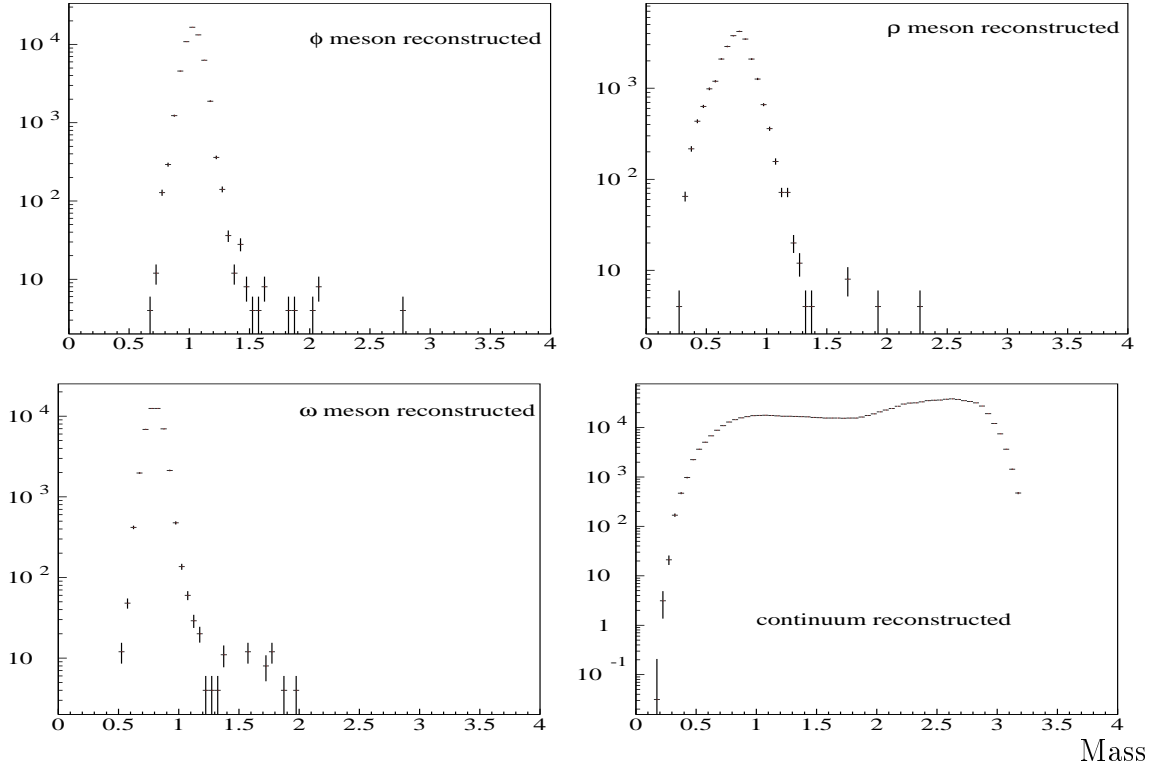


Figure 4.3: Reconstructed mass spectra for ϕ , ρ , ω and continuum (all M_T).

where the kinematical domains are: $-0.5 \leq \cos \Theta_{CS} \leq 0.5$, $0 \leq y \leq 1$ and considered M_T domains.

The acceptances as a function of transverse mass for ω and ϕ are presented in the figure 4.4 (a), and in the Table 4.2.

Acceptances in the low mass region, for dimuon with $M_T < 1.8 \text{ GeV}/c^2$ is less than 1%, and one can worry about eventual unknown systematical uncertainty, the simulation being potentially more sensitive to fine details.

Another basic requirement is that with a similar experimental setup, the acceptances of ω and ϕ should be consistent with the ones determined in previous years. Table 4.2 lists also the acceptance values (at bottom region) from 96 simulation for Pb-Pb. The acceptances of ω and ϕ for 2000 simulation are several percent (3%) higher than 96 simulation in the first M_T bin. (The first M_T bin is very important for the integrated multiplicity measurement.) The improved reconstruction method, leading to an increase of the reconstructed dimuons, could be linked to this increase of the ω and ϕ acceptances.

ΔM_T^i GeV/ c^2	1.5-1.8 (%)	1.8-2.2 (%)	2.2-2.5 (%)	2.5-2.8 (%)	2.8-3.2 (%)
2000 simulation					
ϕ	0.268 ± 0.005	1.93 ± 0.02	4.47 ± 0.08	5.88 ± 0.16	6.16 ± 0.28
ω	0.367 ± 0.007	1.61 ± 0.02	2.90 ± 0.07	3.31 ± 0.12	3.46 ± 0.20
96 simulation					
ϕ	0.26 ± 0.005	1.88 ± 0.02	4.42 ± 0.07	5.76 ± 0.15	6.32 ± 0.27
ω	0.36 ± 0.005	1.57 ± 0.01	2.76 ± 0.05	3.37 ± 0.10	3.17 ± 0.17

Table 4.2: Acceptance factors for ϕ and ω in different M_T intervals and statistical errors.

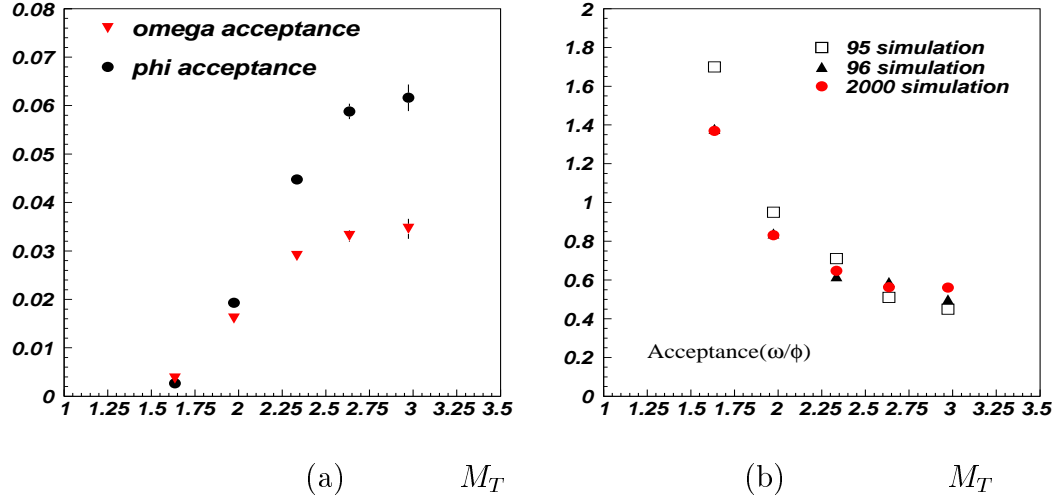


Figure 4.4: Left: the acceptance factor for ω and ϕ as a function of M_T (GeV/ c^2); Right: A comparison of the ratio of acceptance factors for ω and ϕ simulated for different data taking periods.

Acceptance ratios A_ω/A_ϕ in figure 4.4 (b) are consistent with previous 96 results.

Finally ¹, the acceptances of ω and ϕ obtained for Pb-Pb 2000 are consistent with the ones from 96 simulation, within several percent.

¹it is noteworthy that this was not the case first, and that a 20% difference at low E_T was finally explained by a side effect of an improvement in the global cut program

4.4.2 The acceptance comparison to NA38 setup

In order to study the effects on the changes of the experimental setup between S-U and Pb-Pb, and also to check the precision of the simulation for the low acceptance in Pb-Pb, some test simulations are performed. For NA50, several changes have been performed on the detector from S-U to Pb-Pb setup, mainly:

- The increase of the field in the magnet, by a factor $7/4$;
- The replacement of 80 cm carbon by 80 cm iron at the end of the absorber and the matters of the pre-absorber Al_2O_3 by BeO ;
- The modification of the spectrometer pseudorapidity domain to cope with the beam energy, including the changes of the position of the magnet, the position of PC1-PC8, etc.

Beside, some changes have occurred on the analysis side, in particular the “global” cut on the track quality (which were often taken into account in the acceptance).

The figure 4.5 displays the values obtained for the acceptance when changing the absorber, or the magnet, or both, from the NA50 setup. Figure 4.7 shows the acceptance ratios of A_ω/A_ϕ corresponding to those changes, it follows that the changes of the setup do not induce a significant change in the A_ω/A_ϕ ratio, within several percent.

It is noteworthy that the magnet is the leading effect on the decrease of the acceptance observed at low M_T , as it is emphasized by figure 4.6. The iron absorber effect on the acceptance is changing by a factor about 4 in the whole M_T range, whereas the magnet field effect is changing by an order of 8. This field effect has been checked by NA50 [62], and it has been observed that the instrumental effect is perfectly reproduced by the simulation. So finally only a rather “modest” effect, the absorber one, has not been verified by an experimental cross check. This effect being only a factor 4, and evolving smoothly with M_T , it does not seem very likely that a major uncertainty could be attached to the sole low M_T value. In conclusion, despite of the acceptance’s value lower than 1%, it follows that the acceptance determined in Pb-Pb for the 1.5-1.8 GeV/ c^2 M_T bin is not likely to suffer a very different uncertainty than the other M_T bins.

4.5 Decomposition of the mass spectra

To extract the number of resonances detected in the dimuon mass spectra as seen by the detector, one uses the simulated functions corresponding to each component. After

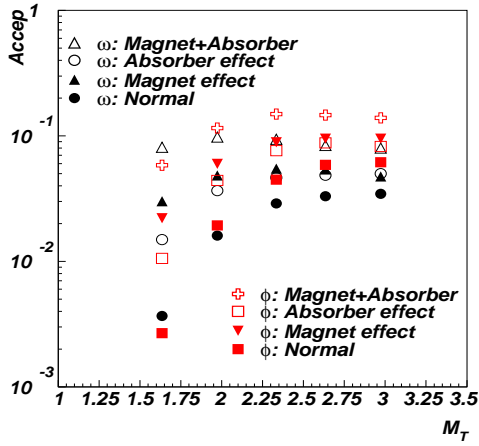


Figure 4.5: The ω and ϕ acceptance factors versus $M_T(\text{GeV}/c^2)$ obtained when changing the magnetic field, the iron absorber and both from NA50 setup.

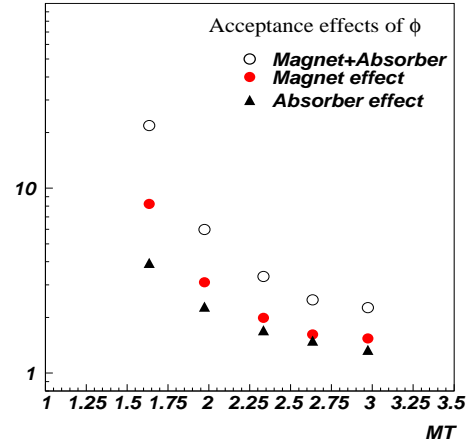


Figure 4.6: The ratio of ϕ acceptance factors calculated before and after subsequent set-up modifications.

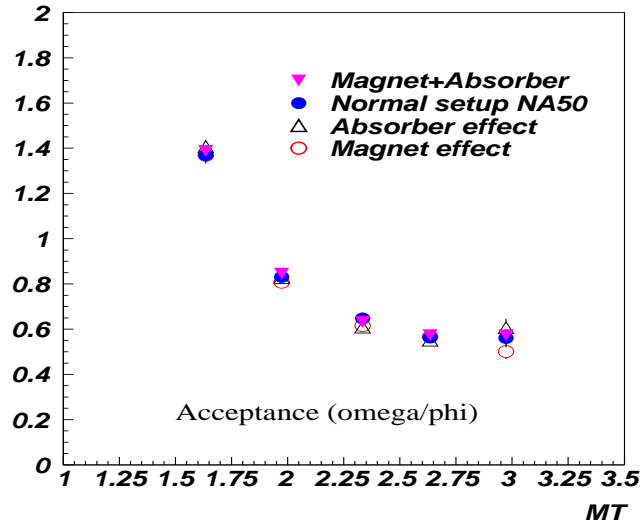


Figure 4.7: The ratios of acceptance factors for ω and ϕ versus M_T calculated including various set-up modifications in Figure 4.5.

subtraction of the combinatorial background, we then fit the dimuon mass spectra with

the sum of all the contributions:

$$\frac{dN_{\mu\mu}}{dM} = A_{\rho+\omega} \left(F_{\rho}(M) + R F_{\omega}(M) \right) + A_{\phi} F_{\phi}(M) + A_{CNT} F_{CNT}(M) , \quad (4.8)$$

where $F_{\rho,\omega,\phi}$ and F_{CNT} are the functions used in the fit for each of the components. These shapes are determined by the Monte-Carlo simulation of generation, followed by the same reconstruction treatment as applied on the real data. These distributions also take into account acceptance and smearing effects on the shapes. A_R , the yield of each component, is taken as free parameter in the fit to the mass spectra. In order to avoid statistical fluctuations in the simulation, and allow a certain freedom in the mean value with respect to the experimental reconstruction², the function F_{ω} and F_{ϕ} are gaussian (with an R.M.S. fitted to the simulated mass spectra).

Contrary to ρ , the ω and ϕ resonances' experimental shapes are dominated by the experimental resolutions. They are also the main contributions to the peaks in the ω and ϕ mass regions. Using gaussian functions (in fact using integrals of gaussian is mandatory given the broad mass bins) also shapes fluctuations in the simulation, which otherwise would add systematical effect between the various kinematical domains. The mass widths of ω and ϕ , obtained by the fit to the simulated mass spectra, are plotted in Figure 4.8. No systematical evolution appears with M_T , so constant mass widths are considered: $\sigma_{\phi} = 70$ MeV, $\sigma_{\omega} = 65$ MeV.

The ρ and ω are assumed to have the same cross section³ $\sigma_{\rho} = \sigma_{\omega}$ [86]. Since dimuon branching ratios are poorly known, their relative decay rates into $\mu^+\mu^-$ are taken equal to the ones measured through e^+e^- decay channel. So R , taking into account the difference between the ρ and ω branching ratios through $\mu^+\mu^-$ decay channel, is fixed in the fit program by

$$R = BR_{\omega \rightarrow e^+e^-} / BR_{\rho \rightarrow e^+e^-} \approx 1.6 .$$

In summary there are 5 free parameters in the fit, 3 parameters for the amplitudes and 2 parameters for the mean values of ω and ϕ .

Fitted mass spectra are shown in Figure 4.9 for the 5 M_T intervals and total M_T interval in all E_T domain ($E_T \geq 10$ GeV), in Figure 4.10 for the 8 E_T slices and total E_T region in all M_T interval ($1.5 \leq M_T \leq 3.2$ GeV/ c^2). Mass spectra from the E_T slice 2,4,6,8 and 5 transverse mass intervals are presented in Figure 4.11.

²in particular uncertainties in the energy loss correction

³and we estimate this before applying the $1/M^4$ factor

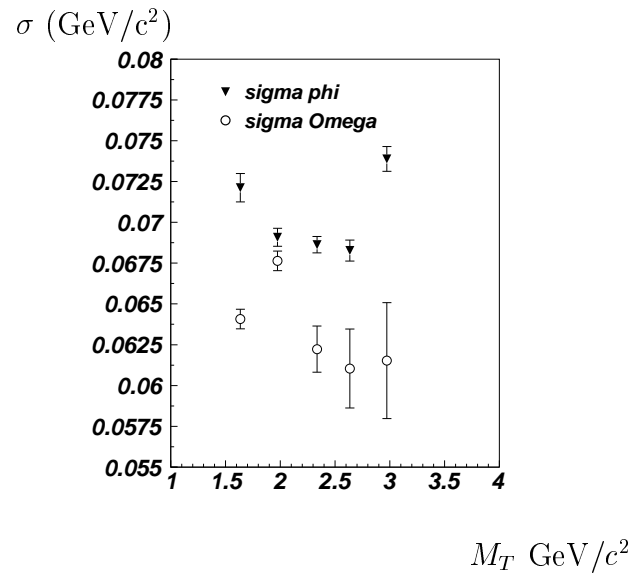


Figure 4.8: The dependence of the width of the invariant masses of ω and ϕ on M_T . The integrated Gaussian fit with 50 MeV/c² bin was used.

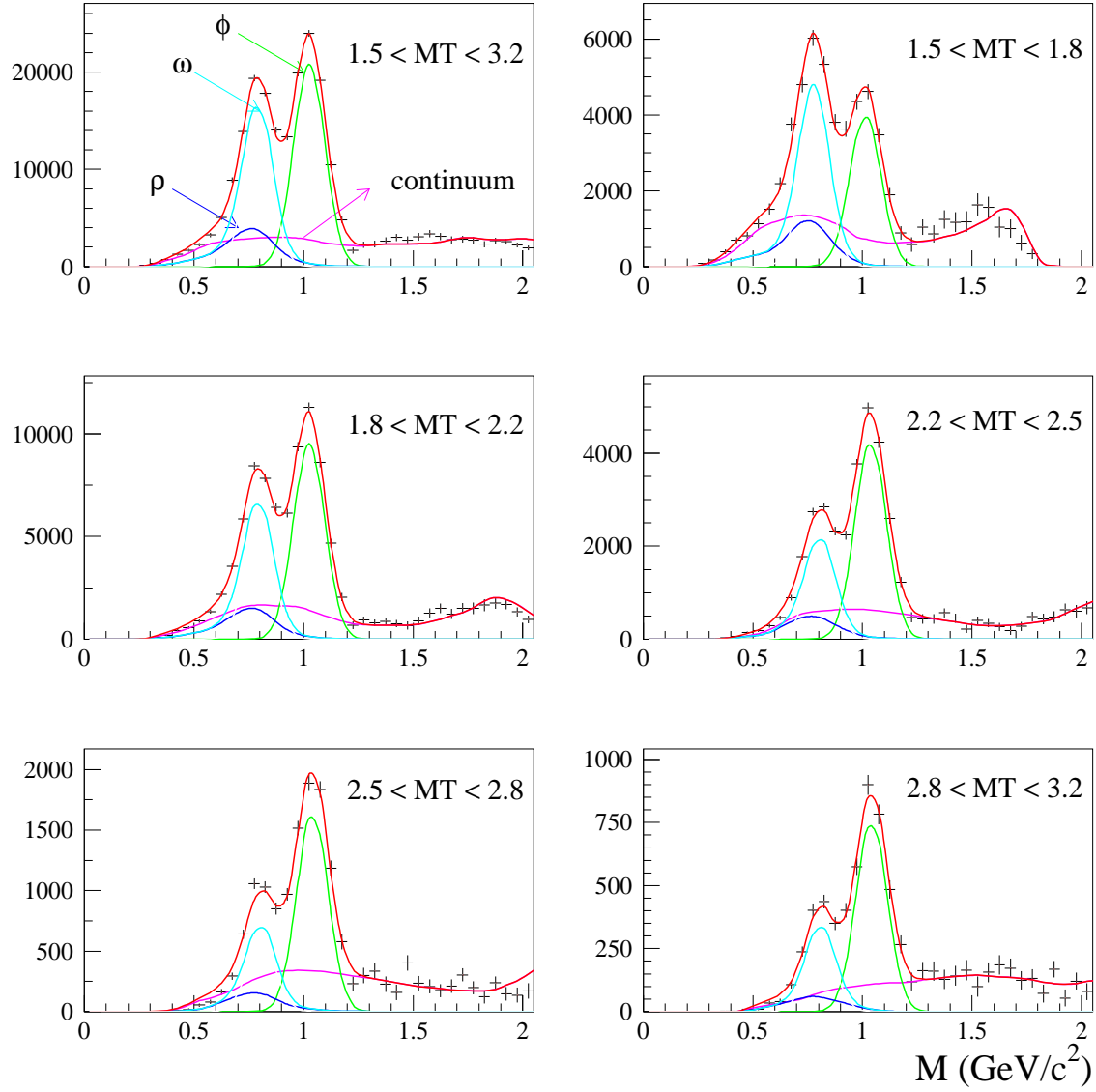


Figure 4.9: The fits to the invariant mass spectra for various M_T intervals for $E_T > 10$ GeV.

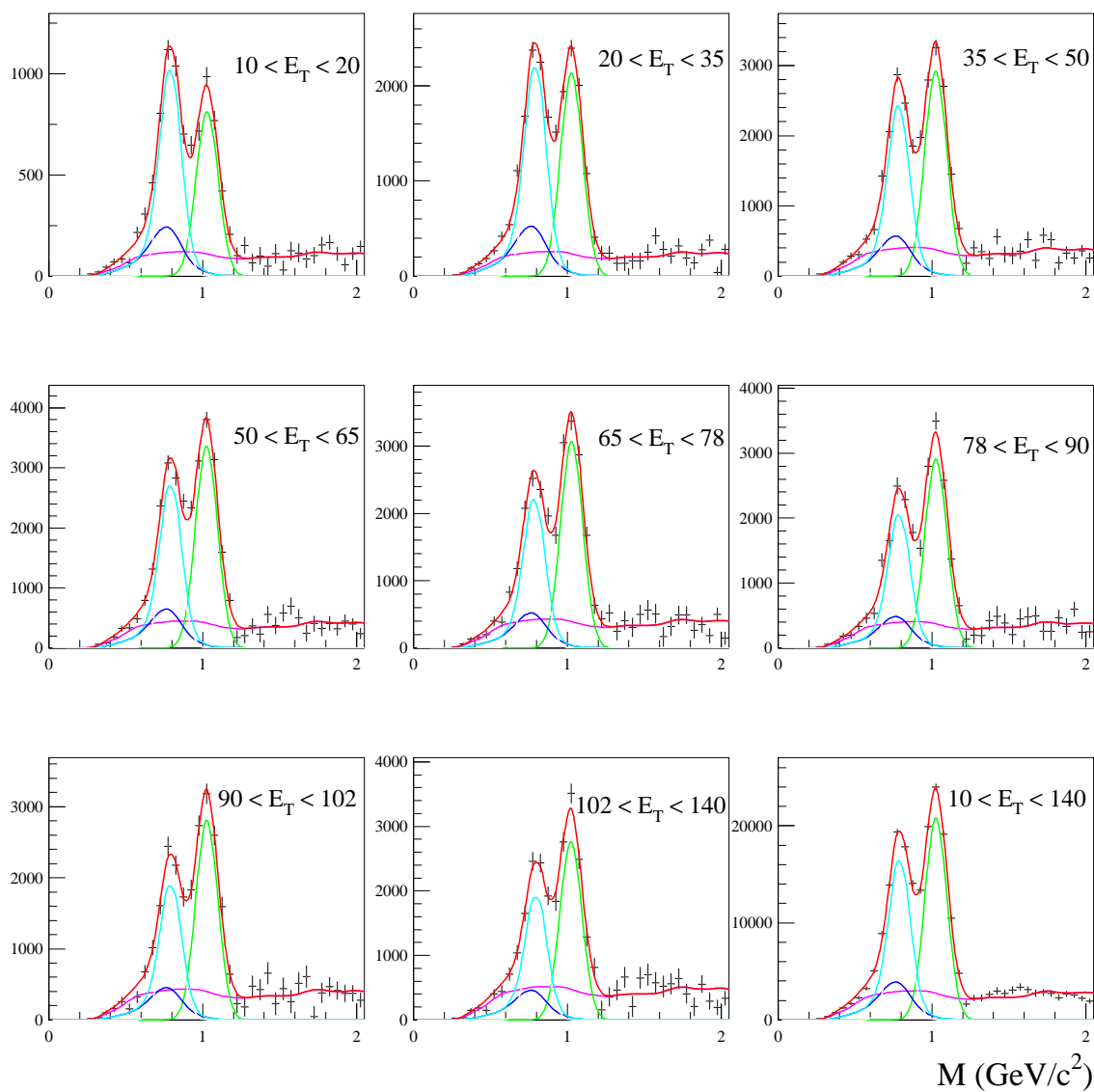


Figure 4.10: The fits to the invariant mass spectra for various E_T intervals in M_T domain $1.5 \leq M_T \leq 3.2 \text{ GeV}/c^2$.

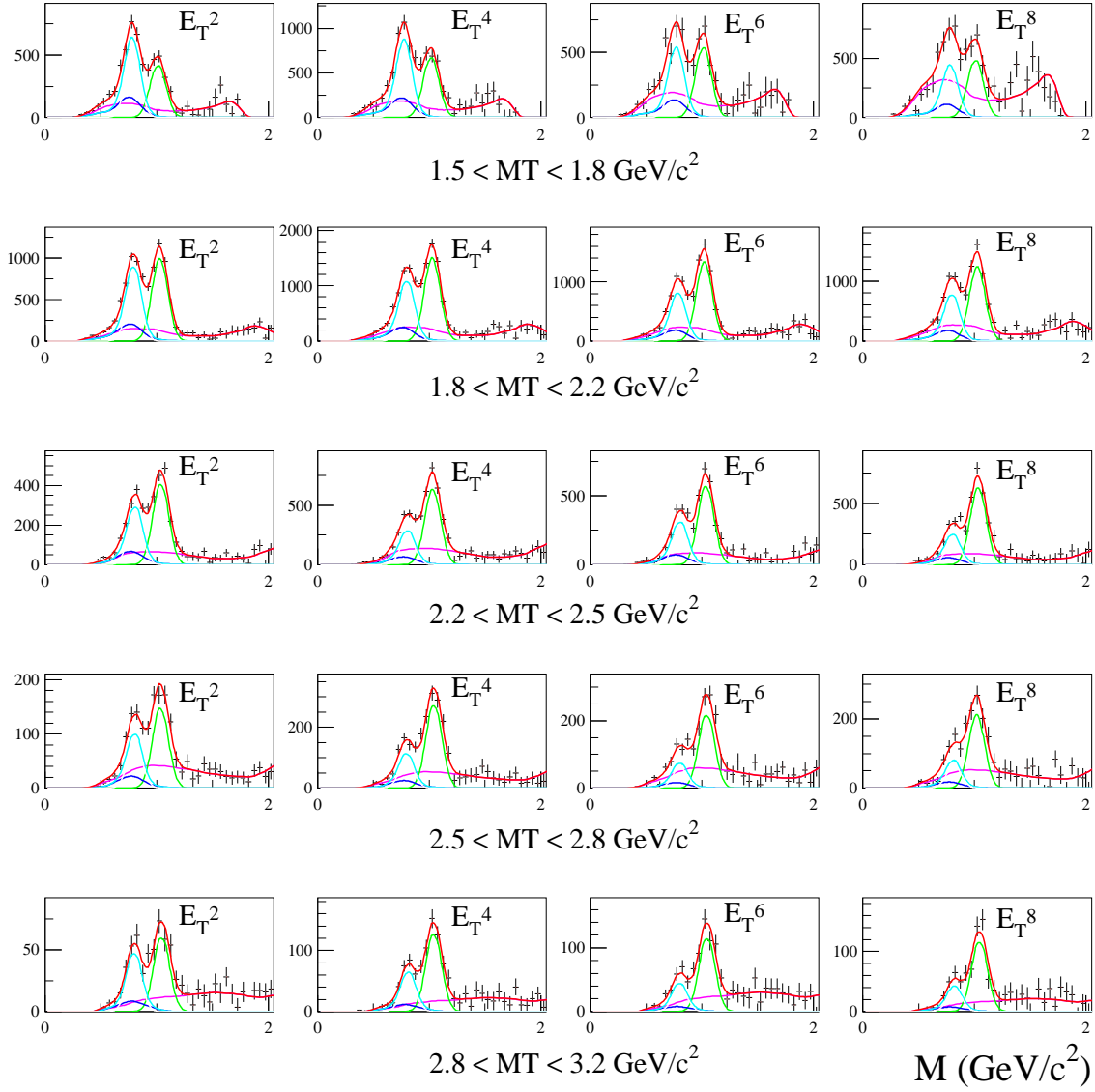


Figure 4.11: Fits to the invariant mass spectra in various E_T and M_T intervals.

Chapter 5

Experimental Results

The dimuon signal mass distributions per transverse mass domain in each transverse energy region are treated as previously described: the smeared physical contributions are extracted, then corrected for acceptance. The ratios of $\sigma_{\phi}^{\mu\mu}/\sigma_{\omega}^{\mu\mu}$ are deduced, as a function of the transverse mass (M_T) and the transverse energy (E_T).

5.1 The results $(\phi/\omega)_{\mu\mu}$

As described previously, the two resonances ρ and ω , can not be distinguished, because the NA50 spectrometer's mass resolution is about 70 MeV/ c^2 whereas their masses differ from each other by only 13 MeV/ c^2 . Due to branching ratios and widths, the peak of the mass spectra in the ω peak region ($0.5 \leq M \leq 0.95$ GeV/ c^2) is mainly dominated by the ω resonance contribution. As explained in section 1.4 this lead us to express results through the ratio of the two resonances, ϕ/ω . Of course, if the ratio ρ/ω , in the ω region, would significantly change, then the whole extraction would have to be reconsidered, since actually this extraction results rely on the $\rho + \omega$ dimuon production in the ω mass region¹.

The ratio $(\phi/\omega)_{\mu\mu}$ of the number of resonances ϕ to the number of resonances ω , produced in the experimental kinematical domain through $\mu^+\mu^-$ channel, after correcting for the acceptances, is obtained by:

$$\left(\phi/\omega\right)_{\mu\mu} = \frac{N_{\phi}^{detected}/A_{\phi}}{N_{\omega}^{detected}/A_{\omega}} \quad , \quad (5.1)$$

where $N_R^{detected}$ is the number of muon pairs for component R extracted from the dimuon mass spectrum, and A_R is the corresponding acceptance value given in the Table 4.2.

¹which nevertheless does not depend on the low mass part of the ρ , contrarily to the $\rho + \omega$ after acceptance correction (see section 1.4.3)

The quantity ϕ/ω has the advantage of being less sensitive than the absolute values to systematic errors, some of them canceling in the ratio.

5.1.1 The uncertainties of the results $(\phi/\omega)_{\mu\mu}$

The uncertainties for the results $(\phi/\omega)_{\mu\mu}(M_T)$ per E_T domain are calculated as:

$$\sqrt{\left(\Delta_{\phi}(stat + fit)\right)^2 + \left(\Delta_{\omega}(stat + fit)\right)^2 + \left(\Delta_{\phi}(method)\right)^2 + \left(\Delta_{\omega}(method)\right)^2}, \quad (5.2)$$

where $\Delta_R(stat + fit)$ is a relative error, including the statistical errors on the number of resonances as it is produced in the fit. This is then also including the error associated to the fit processes, but not including the systematic errors associated to the choice of the ingredients of the fit, which are fixed in the fit processes. These last errors have been studied in detail in [61]. They are included in the errors associated to method $\Delta_R(method)$. These errors include choice of ingredients of the fit, and error on the acceptance determination. They are here added independently for ϕ and ω (listed in Table 5.1).

M_T (MeV/c ²)	1.5-1.8	1.8-2.2	2.2-2.5	2.5-2.8	2.8-3.2
acceptance errors					
ω	4.3	3.3	2.8	3.7	5.2
ϕ	4.3	3.1	2.4	2.8	3.1
method errors					
ω	3	5	7	7	7
ϕ	7	3	4	5	6

Table 5.1: Relative errors (%) for acceptance and fit method

5.1.2 Evolution of $(\phi/\omega)_{\mu\mu}$ as a function of M_T

In Figure 5.1 and 5.2, we present the results $(\phi/\omega)_{\mu\mu}$ as a function of M_T , per transverse energy domain. No dependency on M_T of the ratio $(\phi/\omega)_{\mu\mu}$ is seen from the plots, but $(\phi/\omega)_{\mu\mu}$ is increasing from the peripheral to central collisions.

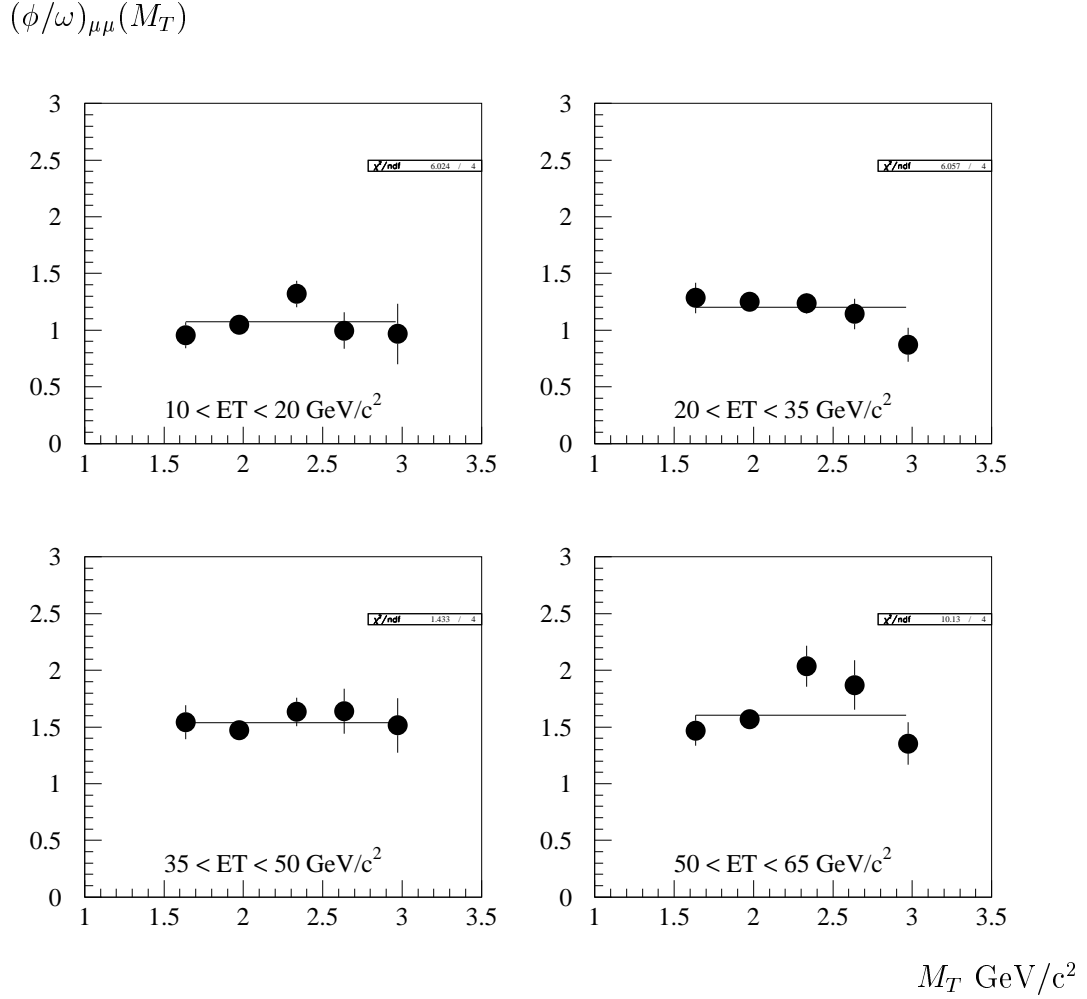


Figure 5.1: The ratio $(\phi/\omega)_{\mu\mu}$ as a function of M_T in different E_T bins.

$$(\phi/\omega)_{\mu\mu}(M_T)$$

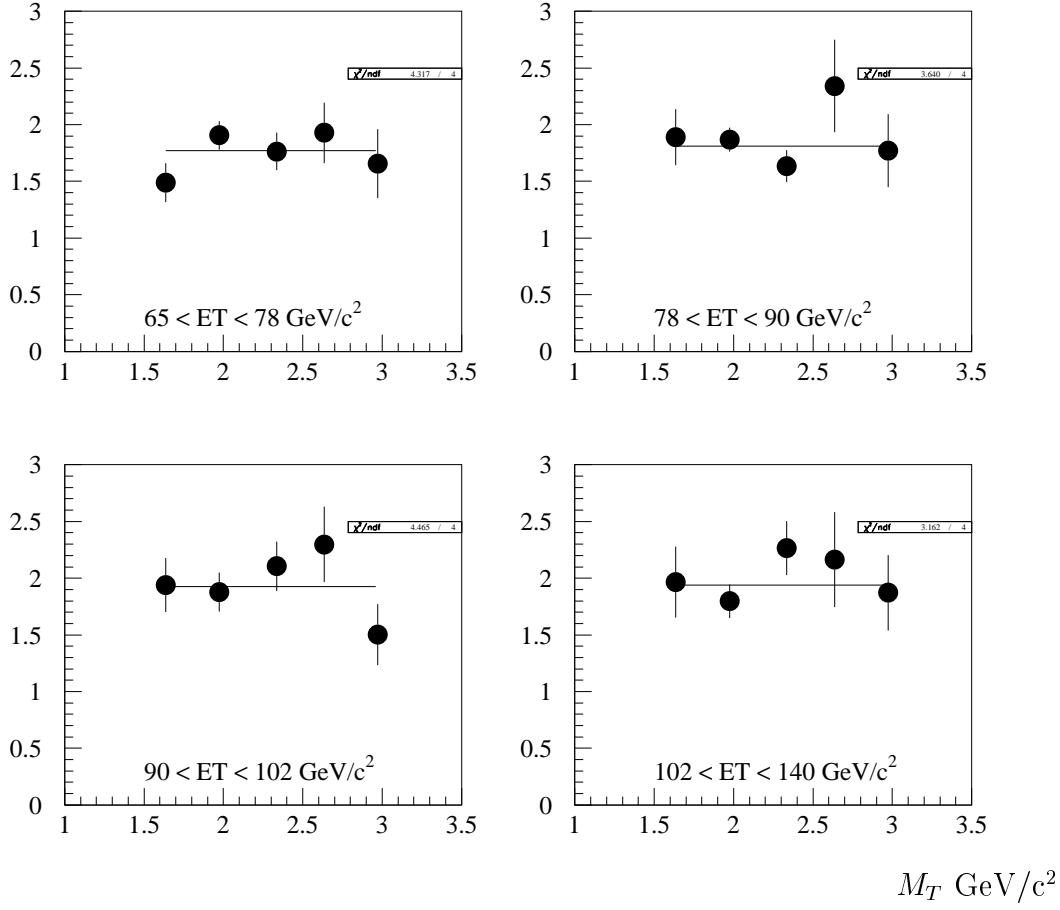


Figure 5.2: The ratio $(\phi/\omega)_{\mu\mu}$ as a function of M_T in different E_T bins.

5.1.3 Evolution of $(\phi/\omega)_{\mu\mu}$ as a function of E_T

The evolution of the the results $(\phi/\omega)_{\mu\mu}$ as a function of E_T for 5 M_T intervals and in all M_T interval are plotted in figure 5.3, an increasing behavior is seen from the figure, by a factor of 2 from peripheral collisions to the central ones. The values for the $(\phi/\omega)_{\mu\mu}$ results are listed in Table 5.2 .

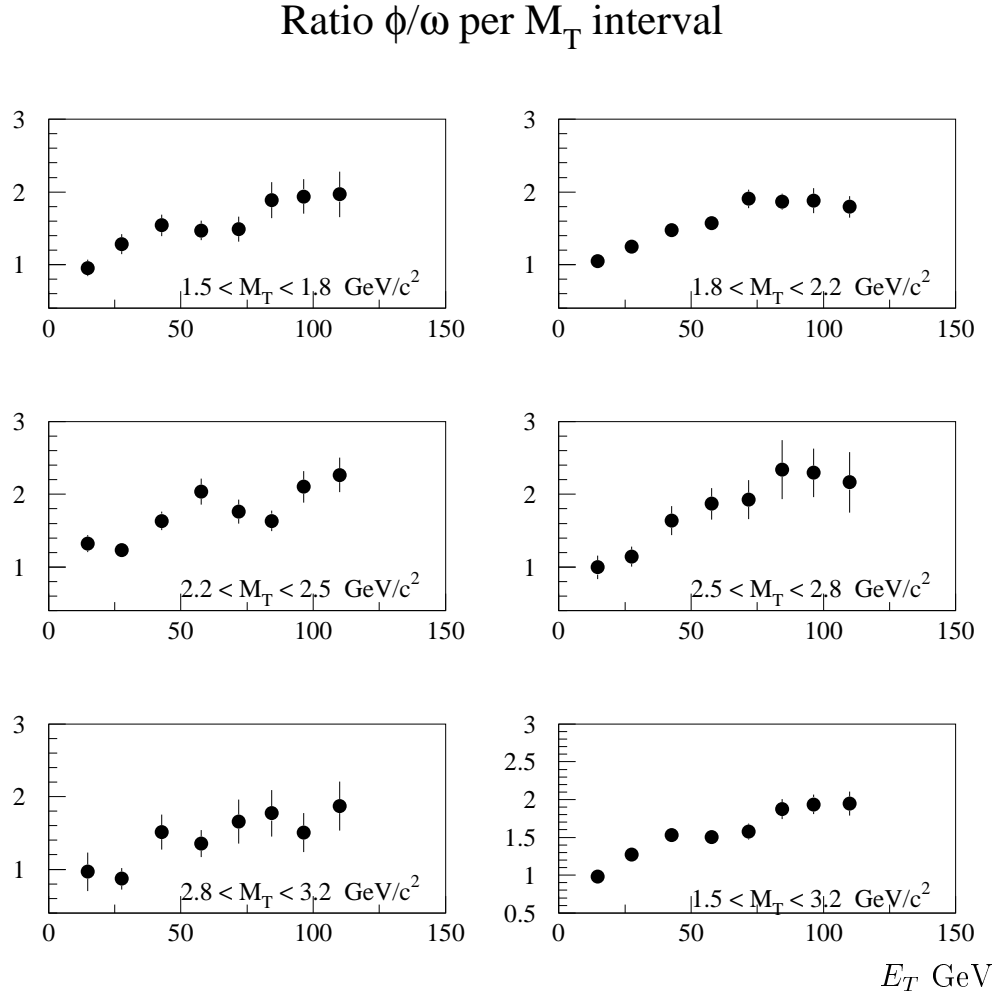


Figure 5.3: The ratio $(\phi/\omega)_{\mu\mu}$ as a function of E_T in various M_T intervals and in all M_T interval.

5.2 Cross section of σ^ϕ and σ^ω

5.2.1 Determination of σ^ϕ and σ^ω .

The cross section is nothing but the equivalent surface of the couple target-projectile, for the considered process.

The cross section for production of resonance R is then:

$$\sigma^R = \frac{N_R}{N_{inc}(0) L_{eff} n_{Target}} , \quad (5.3)$$

ΔM_T^i GeV/ c^2	1.5-3.2 Total M_T	1.5-1.8	1.8-2.2	2.2-2.5	2.5-2.8	2.8-3.2
ΔE_T^1	0.98 ± 0.08	0.95 ± 0.11	1.05 ± 0.08	1.32 ± 0.12	1.00 ± 0.16	0.97 ± 0.27
ΔE_T^2	1.27 ± 0.08	1.28 ± 0.14	1.25 ± 0.07	1.24 ± 0.09	1.14 ± 0.13	0.87 ± 0.15
ΔE_T^3	1.53 ± 0.09	1.54 ± 0.15	1.47 ± 0.08	1.63 ± 0.13	1.64 ± 0.20	1.51 ± 0.24
ΔE_T^4	1.51 ± 0.08	1.47 ± 0.14	1.57 ± 0.09	2.04 ± 0.18	1.87 ± 0.22	1.35 ± 0.19
ΔE_T^5	1.58 ± 0.11	1.49 ± 0.17	1.91 ± 0.13	1.76 ± 0.17	1.93 ± 0.27	1.66 ± 0.30
ΔE_T^6	1.88 ± 0.13	1.89 ± 0.25	1.87 ± 0.11	1.63 ± 0.14	2.34 ± 0.41	1.77 ± 0.32
ΔE_T^7	1.94 ± 0.13	1.94 ± 0.24	1.88 ± 0.17	2.11 ± 0.22	2.30 ± 0.33	1.50 ± 0.27
ΔE_T^8	1.95 ± 0.16	1.97 ± 0.31	1.80 ± 0.15	2.27 ± 0.24	2.16 ± 0.42	1.87 ± 0.33

Table 5.2: The values for $(\phi/\omega)_{\mu\mu}$ per M_T and E_T interval.

where N_R is the total number of resonance produced in the relevant kinematical domain, $N_{inc}(0)$, the number of ions in the beam. $N_{inc}(0) \cdot \exp(-x/\Lambda_{Pb-Pb})$ is the number of ions left after absorption for a given target length x . This effect is taken into account through the notion of “effective target” $L_{eff} = \Lambda_{Pb-Pb} (1 - \exp(-l/\Lambda_{Pb-Pb}))$ where l is the target length. $\Lambda_{Pb-Pb} = (\sigma^{Pb-Pb} n_{Target})^{-1}$ is the interaction length, where σ^{Pb-Pb} is the effective cross section of the Pb-Pb interaction. n_{Target} is the number of atoms of Pb in the target per volume unit, and is calculated through the mass number per volume unit ρ_{Target} ,

$$n_{Target} = \frac{\rho_{Target}}{A} \times N_A, \quad (5.4)$$

where N_A is the Avogadro constant.

The interaction cross section σ^{A-B} for the interaction of two ions with the mass number A and B , is calculated by the expression

$$\sigma^{A-B} = 68.8 (A^{1/3} + B^{1/3} - 1.32)^2 \text{ mbarns}. \quad (5.5)$$

This formula is used for estimating the σ^{Pb-Pb} cross section in order to obtain L_{eff} . The values of quantities used for calculating the cross section are listed in Table 5.3 .

5.2.2 The efficiency determination

The cuts used are *PILEUP*, *NPARAS*, *NOCIMD*, *NICALO*, *T0J*, *NIZDC*, (*P*Dtarg* for Dimuon trigger), *Banana*, as explained in section 3.8. The different efficiency values calculated from the data are listed in the Table 3.1, for BH trigger, Dimuon trigger and luminosity scalers.

Quantity	Value
A_{Pb}	207.2
σ^{Pb-Pb}	7606 mbarns
ρ_{Target}	$11.35 \pm 0.57 \text{ g/cm}^3$
n_{Target}	$3.30 \times 10^{22} / \text{cm}^3$
Λ^{Pb-Pb}	3.98cm
l	4 mm
L_{eff}	0.38 cm
N_{inc}^{BH}	6.56×10^{12}

Table 5.3: Values used for the cross section in Pb+Pb collisions.

The number of incident ions N_{inc}^{BH} considered for calculating the effective cross section is given by,

$$N_{inc}(0) = N_{inc}^{BH} \times \epsilon_{Pileup} \times \epsilon_{DAQ} \times \epsilon_{NPARAS} , \quad (5.6)$$

which is the effective number of incident ions, taking into account the DAQ unavailability, beam pile up and rejection of ions by the BH interaction counters.

The number of resonances in the experimental acceptance, corresponding to this number of incoming ions, is the one obtained in the analysis, corrected of the rejections of signal due to the various cuts used to reject the backgrounds, or corrected of instrumental inefficiencies.

$$N_R = \frac{N_R^{Detected}}{A_R} \times \frac{1}{\epsilon_{DIMUREC}} \times \frac{1}{\epsilon_{Trigger}} \times \frac{1}{\epsilon_{cuts}} , \quad (5.7)$$

where ϵ_{cuts} contains all the cuts suffered by dimuons as described in the table 3.1, and A_R is acceptance for the resonance R .

5.2.3 The uncertainties of σ^ϕ and σ^ω

Cross section are determined per M_T interval. As for ϕ/ω the uncertainty comes from the statistical and the fit uncertainties, and the systematical uncertainty comes from the uncertainties already considered for the ratio ϕ/ω (see section 5.1.1), plus the systematical uncertainties due to normalization of the beam and efficiencies acting on dimuons (see table 3.1), which were cancelling in the ratio ϕ/ω . The uncertainty on the number of atoms per cm^2 in the target is also important for the cross section precision. From

previous measurements [87], it is known that the dominant error for this target thickness is the density of Pb, which is about 2.5%. All these uncertainties are independent and are added quadratically.

5.2.4 The σ^ϕ and σ^ω values in all E_T domain

The effective cross section values per M_T bins in all E_T domain ($E_T \geq 10$ GeV/ c^2) are given in Table 5.4, the statistical and systematic error are given separately.

M_T interval (GeV/ c^2)	σ^ϕ (mbarn)	σ^ω (mbarn)
1.5-1.8	$0.1871 \pm 0.00599 \pm 0.01881$	$0.1184 \pm 0.00322 \pm 0.00924$
1.8-2.2	$0.0604 \pm 0.00091 \pm 0.00472$	$0.0372 \pm 0.00070 \pm 0.00327$
2.2-2.5	$0.0115 \pm 0.00022 \pm 0.00095$	$0.0065 \pm 0.00017 \pm 0.00066$
2.5-2.8	$0.0033 \pm 0.00009 \pm 0.00029$	$0.0018 \pm 0.00008 \pm 0.00018$
2.8-3.2	$0.0014 \pm 0.00005 \pm 0.00013$	$0.0010 \pm 0.00005 \pm 0.00010$

Table 5.4: The dimuon cross section values of σ^ϕ and σ^ω for Pb-Pb per M_T bins (for $-0.5 \leq \cos \Theta_{CS} \leq 0.5$ and $0 \leq y^* \leq 1$) .

5.3 The Effective temperature of ω and ϕ

From the expression (4.4), when $M_T \gg T$, it can be approximated as :

$$\frac{d\sigma}{dM_T} \propto M_T^{3/2} \exp(-M_T/T) . \quad (5.8)$$

Expression 5.8 will be used to fit the M_T distribution for ω and ϕ to obtain the inverse slope or “effective temperature” T .

5.3.1 Determine the M_T abscissa

The M_T abscissa values M_T^{Abs} in each M_T slice are a posteriori calculated, taking into account the T slope value. For a given interval (M_T^i, M_T^{i+1}) , the value M_T^{Abs} is determined by:

$$(M_T^{i+1} - M_T^i) \times f(M_T^{Abs}) = \int_{M_T^i}^{M_T^{i+1}} f(M_T) dM_T . \quad (5.9)$$

In this way, there is no bias between the value from the function at M_T^{Abs} and the integral in each M_T bin limits. The calculated values of the M_T abscissa are listed in the table 5.5, with $T = 216$ MeV for Pb-Pb. In Figure 5.4, the fits to the M_T distributions are shown. Other solutions are possible, like fitting by the integral in the bin [88] which is simpler. The solution used here is also convenient for plotting.

ΔM_T GeV/ c^2	1.5-1.8	1.8-2.2	2.2-2.5	2.5-2.8	2.8-3.2
$T_{\text{fix}} = 216$ MeV	1.6354	1.9735	2.3346	2.6344	2.9722

Table 5.5: The calculated values of the M_T abscissa.

5.3.2 Effective temperature as a function of centrality

The temperature as a function of the centrality (E_T here), is shown in figure 5.5 and Table 5.6.

E_T slice (GeV)	$\langle E_T \rangle$ (GeV)	T_ϕ (MeV)	T_ω (MeV)
$10 \leq E_T \leq 20$	14.72	210 ± 5	204 ± 4
$20 \leq E_T \leq 35$	27.57	209 ± 4	219 ± 4
$35 \leq E_T \leq 50$	42.70	214 ± 3	213 ± 3
$50 \leq E_T \leq 65$	57.73	219 ± 4	208 ± 4
$65 \leq E_T \leq 78$	71.80	218 ± 4	213 ± 4
$78 \leq E_T \leq 90$	84.36	220 ± 4	215 ± 4
$90 \leq E_T \leq 102$	96.33	221 ± 4	216 ± 5
$E_T \geq 102$	109.96	225 ± 5	219 ± 5

Table 5.6: Effective temperature values as a function of E_T .

From the values of T plotted as a function of E_T one can determine the average value for ω and ϕ by a fit to a line, which leads to $T_\omega = 213 \pm 4$ MeV and $T_\phi = 217 \pm 4$ MeV.

$d\sigma^\phi/M_T dM_T$ (mb GeV⁻²c⁴)

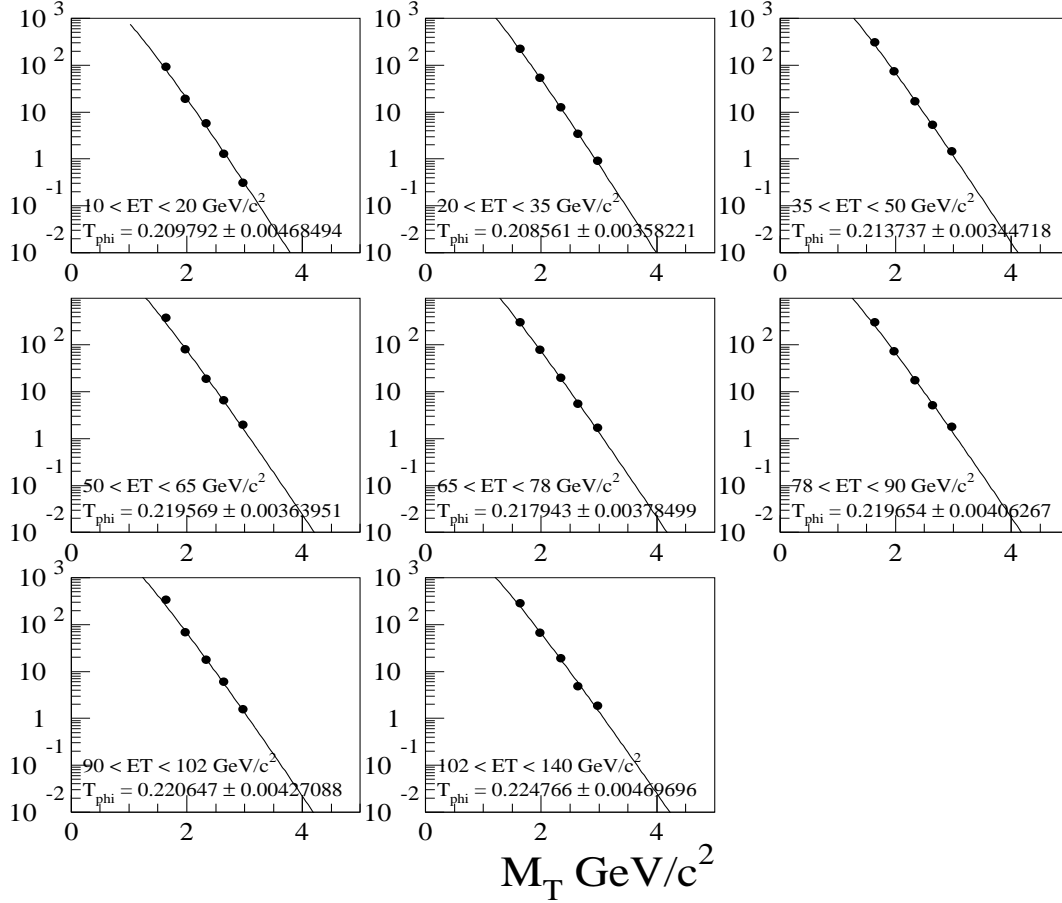


Figure 5.4: The M_T spectra of ϕ meson for various E_T intervals. The “thermal” fits to the spectra with $M_T^{3/2} \exp(-M_T/T)$ are indicating by solid lines.

5.4 The multiplicity measurement

5.4.1 The multiplicity definition

The multiplicity is the average number of particles produced per PbPb collision. The number of particles produced is determined as previously described from the mass spectra

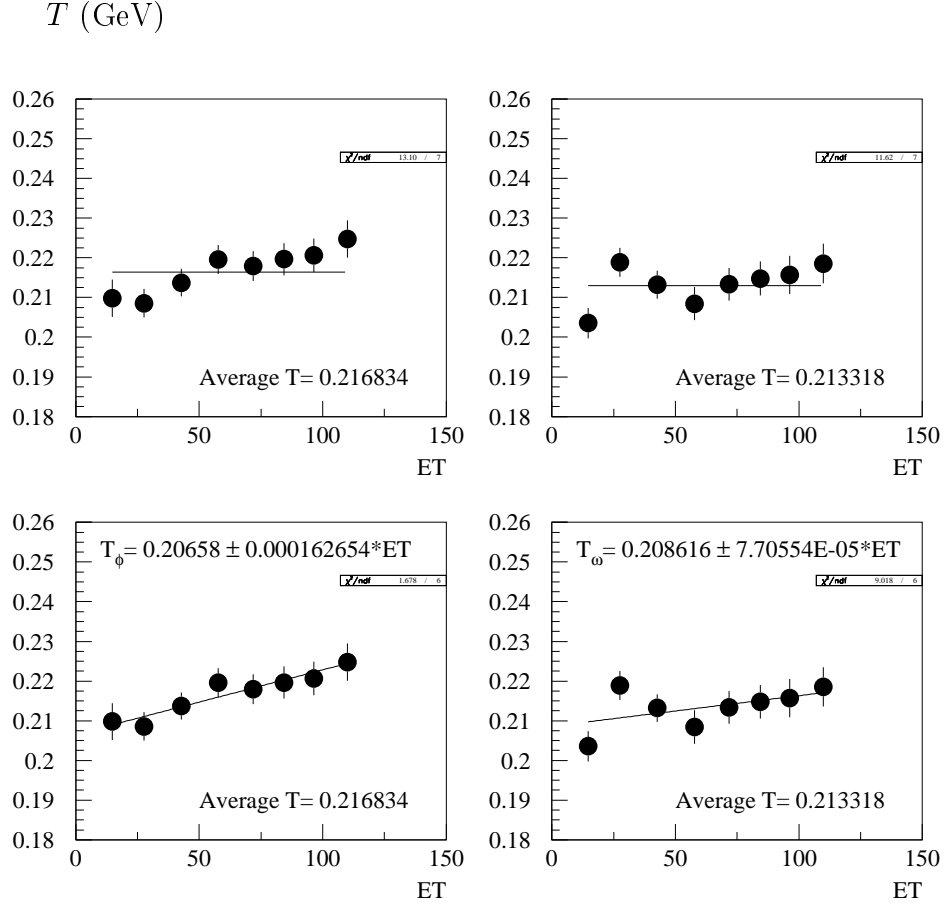


Figure 5.5: The effective temperature of ϕ and ω versus E_T with the horizontal line fits (top) and with the linear fits (bottom).

in a given E_T bin, and corrected for acceptance and eventually of branching ratio. The number of collisions in the same E_T bin is obtained thanks to the minimum bias trigger.

For the resonance R , in the domain $(\Delta M_T^i, \Delta E_T^j)$, the multiplicity N_R^{mul} is calculated through the formula,

$$N_R^{mul}(\Delta M_T^i, \Delta E_T^j) = \frac{N_R^{detected}(\Delta M_T^i, \Delta E_T^j) / (A_R \times BR_R)}{N_{M.B.}(\Delta E_T^j) \times f_{Prescaling} \times \epsilon_{Trigger}^{\mu\mu} \times \epsilon_{Dimurec} \times \epsilon_{cut}^{rel.}} \quad (5.10)$$

where $R = \omega, \phi$, A_R is the acceptance, BR_R is the branching ratio for each resonance, $N_R^{detected}(\Delta M_T^i, \Delta E_T^j)$ is the number of resonances detected in the certain ΔM_T^i and ΔE_T^j domain, $N_{M.B.}(\Delta E_T^j)$ is the event number of Min. Bias in the ΔE_T^j domain, $f_{Prescaling}$ is

the Min. Bias (BH trigger) prescaling factor, $\epsilon_{Trigger}^{\mu\mu}$ and $\epsilon_{Dimurec}$ are the dimuon trigger efficiency and the reconstruction efficiency, and $\epsilon_{cut}^{rel.}$ is the ratio of cut efficiencies for dimuons and minimum bias triggers (for most of the cuts this ratio is 1 see figure 3.23).

$f_{Prescaling}$ is the ratio of the total number of ions in BH seen by the 16 blades scalers, divided by the total number of Min. Bias BH triggers seen at the RELMIC entrance stage, i.e. before cuts. As visible in Figures 3.23, pileup effect could be very different (from 30 to 50% typically) depending on the trigger/observable considered, and this could create a bias in the multiplicity which could depend on the cut in a fictitious way. This effect has been checked [89] not introducing bias in the determination of the multiplicity.

The Uncertainty

There are 4 different kinds of uncertainties introduced by the analysis for the multiplicity calculation of resonance R ,

1. The statistical errors from the number of resonances $E_R(stat + fit)$ (see section 5.1.1) and the statistical errors from the Min. Bias $E_{NMB}(stat)$;
2. The uncertainty on the assumptions made in the simulation, playing on the acceptances determination and on the fit ;

$$\sqrt{\left(E_{AccR}^{\Delta M_T^i}\right)^2 + \left(E_{NR}^{\Delta M_T^i}(Method)\right)^2}$$

3. The systematic errors on the efficiencies (Most of the systematic errors are canceled in the ratio of Dimuon trigger to BH trigger),

$$\sqrt{\left(E_{\epsilon}^{T0J}\right)^2 + \left(E_{\epsilon}^{P*Dtarg}\right)^2 + \left(E_{\epsilon}^{\mu\mu Trig}\right)^2 + \left(E_{\epsilon}^{Recons}\right)^2} = 4.0 \% .$$

4. if needed, uncertainty on the dimuon branching ratios [85]:

$$BR_{\phi \rightarrow \mu\mu} = (2.870 \pm 0.180) \times 10^{-4} ,$$

$$BR_{\omega \rightarrow \mu\mu} = (7.042 \pm 0.481) \times 10^{-5} .$$

5.4.2 The Multiplicities of ω , ϕ as a function of N_{part}

The multiplicity values of ϕ and ω with $M_T > 1.5 \text{ GeV}/c^2$ in each E_T interval are listed in Table 5.7 and plotted in Figure 5.10. One observes an increase of the ϕ and ω multiplicities as a function of N_{part} .

In contrast ϕ and ω multiplicities per participant have different behaviors: Figure 5.10 presents the ratios of N_{mult}^{ϕ}/N_{part} and $N_{mult}^{\omega}/N_{part}$. The number of ω per participant appears constant, whereas the number of ϕ mesons per participant increases, showing that the ϕ production is enhanced.

E_T (GeV/ c^2)	$\langle E_T \rangle$ (GeV/ c^2)	$N_{multiplicity}^{\phi}$	$N_{multiplicity}^{\omega}$
10 - 20	14.72	$0.047 \pm 0.004 \pm 0.004$	$0.193 \pm 0.009 \pm 0.013$
20 - 35	27.57	$0.113 \pm 0.007 \pm 0.008$	$0.364 \pm 0.016 \pm 0.023$
35 - 50	42.70	$0.218 \pm 0.012 \pm 0.016$	$0.581 \pm 0.026 \pm 0.037$
50 - 65	57.73	$0.340 \pm 0.018 \pm 0.026$	$0.918 \pm 0.040 \pm 0.061$
65 - 78	71.80	$0.415 \pm 0.026 \pm 0.030$	$1.063 \pm 0.057 \pm 0.069$
78 - 90	84.36	$0.537 \pm 0.035 \pm 0.040$	$1.169 \pm 0.077 \pm 0.074$
90 - 102	96.33	$0.690 \pm 0.044 \pm 0.053$	$1.455 \pm 0.097 \pm 0.095$
>102	109.96	$0.703 \pm 0.055 \pm 0.052$	$1.478 \pm 0.120 \pm 0.093$

Table 5.7: The multiplicity values of ϕ and ω (for $-0.5 \leq \cos \Theta_{CS} \leq 0.5$ and $0 \leq y \leq 1$) .

The same trend are observed in each M_T domain considered in Figure 5.6 and Figure 5.7, and the behaviors of multiplicities per participant nucleon (divided by N_{part}) as a function of N_{part} are shown in Figure 5.8 and Figure 5.9.

$$dN_{mult}^{\phi}/dM_T \text{ (GeV}/c^2\text{)}^{-1}$$

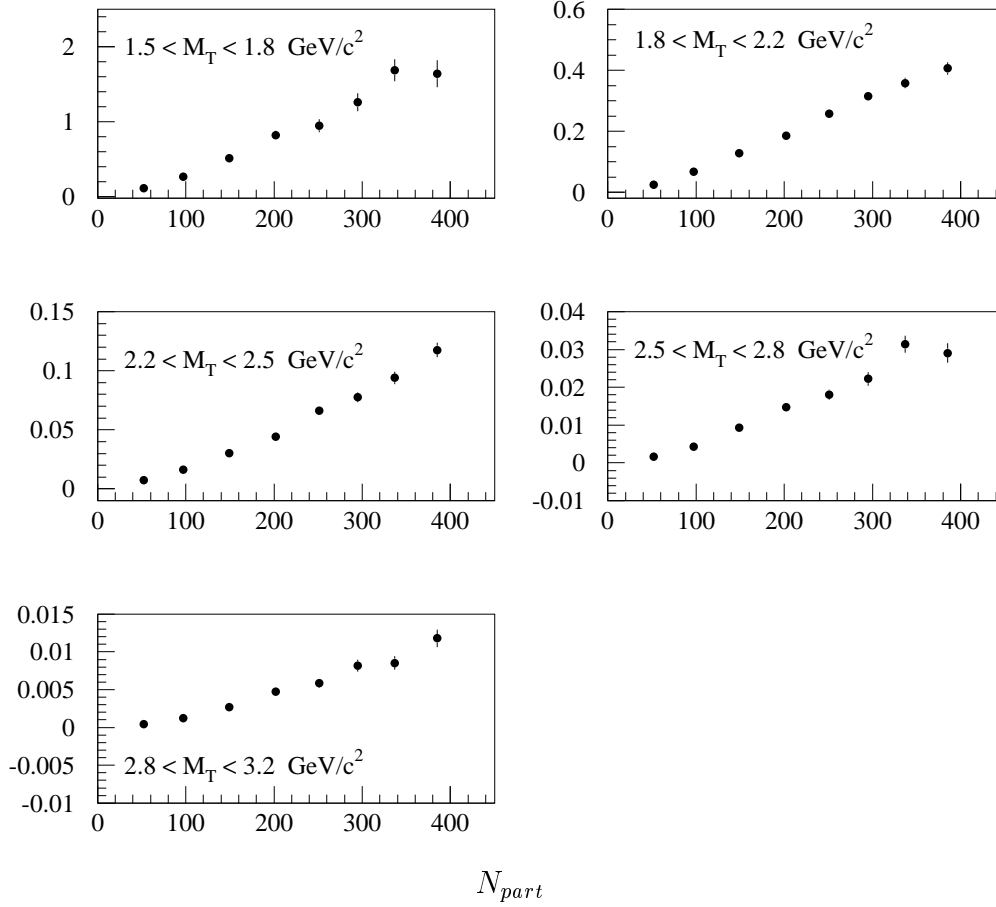


Figure 5.6: The multiplicity of ϕ as a function of N_{part} for various M_T intervals.

$$dN_{mult}^{\omega}/dM_T \text{ (GeV}/c^2\text{)}^{-1}$$

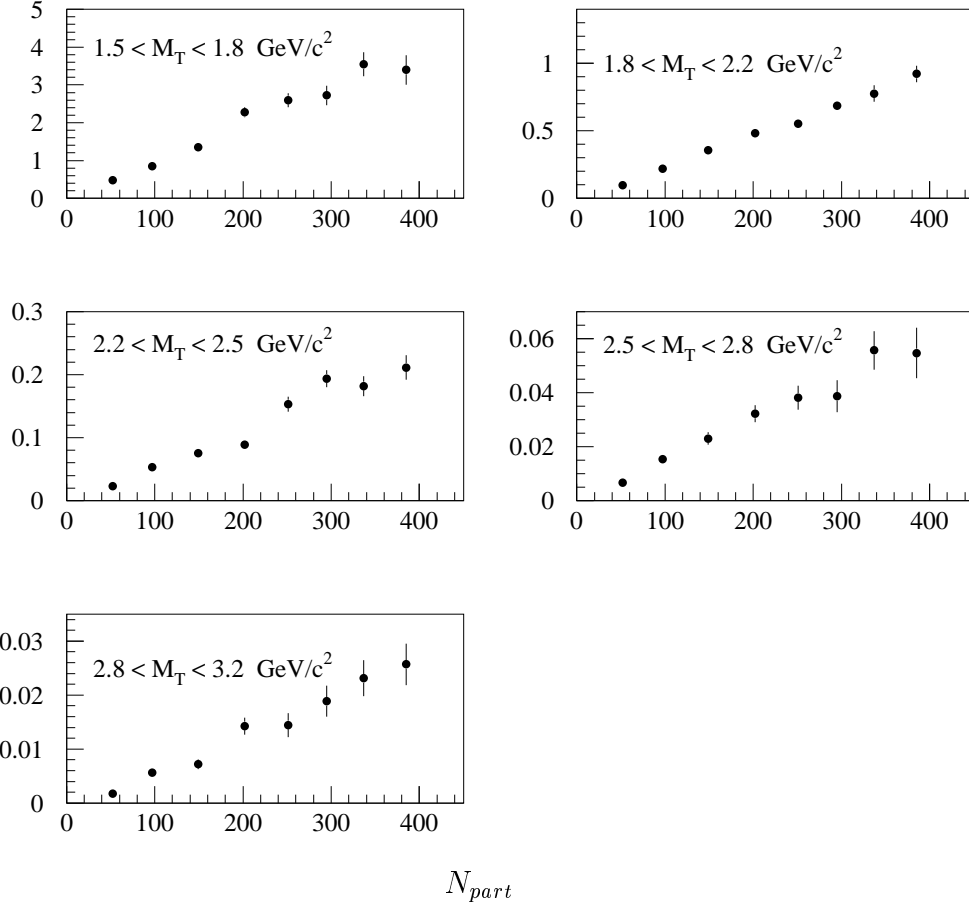


Figure 5.7: The multiplicity of ω as a function of N_{part} for various M_T intervals.

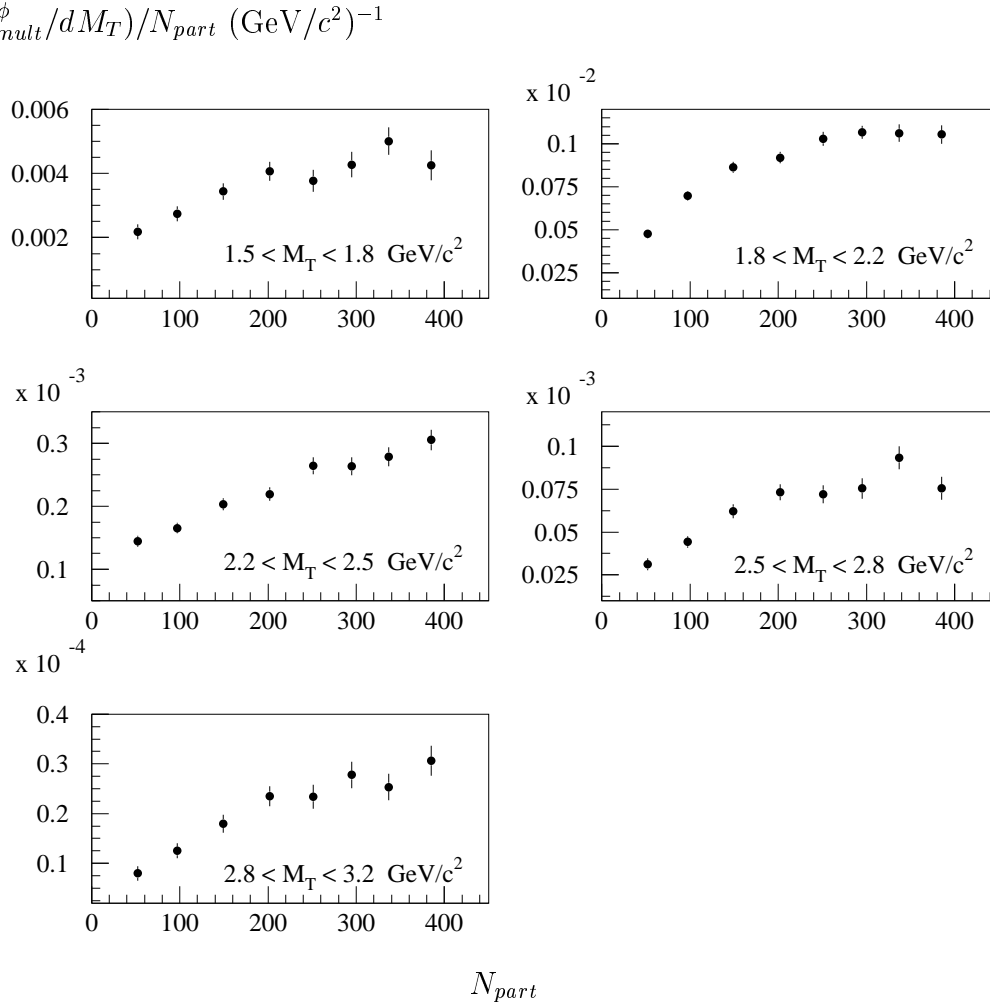


Figure 5.8: The multiplicity of ϕ per participant nucleon as a function of N_{part} for various M_T intervals.

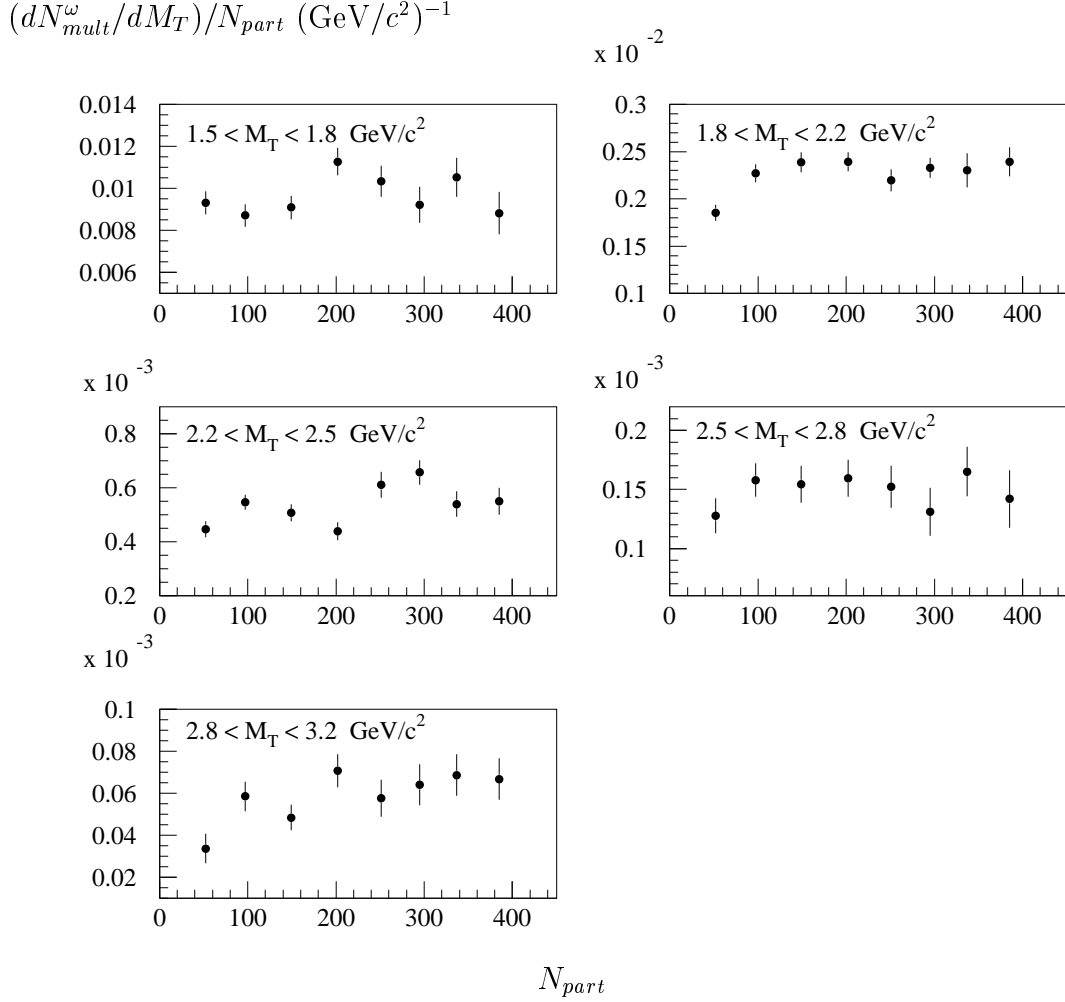


Figure 5.9: The multiplicity of ω per participant nucleon as a function of N_{part} for various M_T intervals.

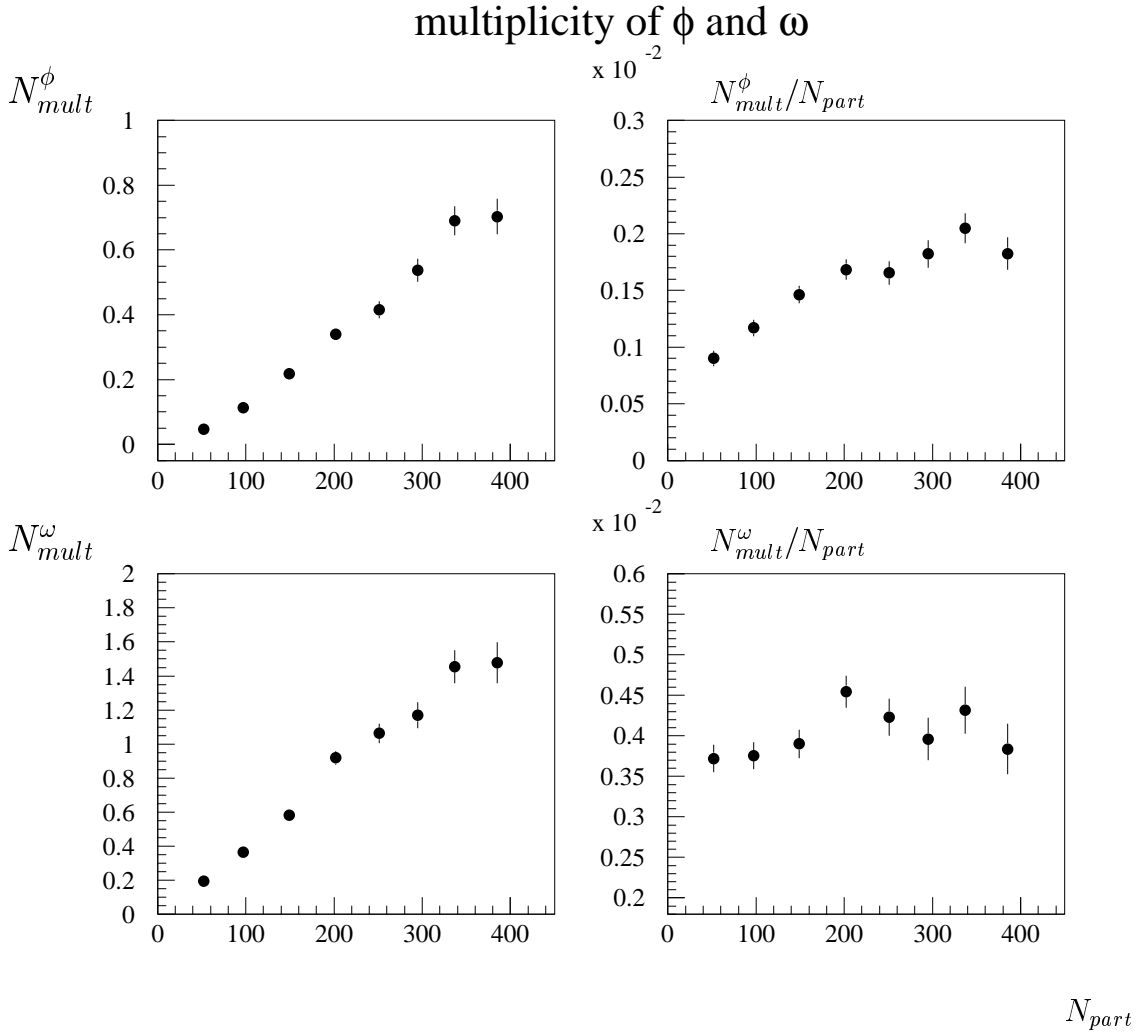


Figure 5.10: The multiplicities and the multiplicities per participant for ϕ and ω as a function of N_{part} in the interval $1.5 \leq M_T \leq 3.2 \text{ GeV}/c^2$.

Chapter 6

Results Discussion

In this chapter we intent to see how these results compare with previous ones and with ones from other experiments, and fit in the more general questioning of strangeness production enhancement, from AGS to RHIC.

6.1 Comparison of other ϕ central multiplicity determinations in NA50 and NA49

From 1997 [90, 61] when ϕ meson production in Pb-Pb collisions of NA50 1995 experiment has been presented for the second time, the question of the comparison to NA49 measurements through KK [67] channel has been raised. The multiplicity of ϕ has been presented in 1999 [91, 62] and a comparison between the two results has been made based on this presentation [68] (Figure 6.1). More recently 1998 data have been obtained, but normalized on previous 1996 data since normalization information is absent in this data set. Finally, this thesis is dealing with the last 2000 data, obtained with a setup aiming at a redundant check of the minimum bias measurement through the implementing of a second minimum bias trigger based on the beam hodoscope, and this global cross check could possibly lead to the most elaborated multiplicity measurement in NA50.

A preliminary result for these last NA50 2000 data has been obtained for the 2003 strangeness in quark matter conference [92]. The main trends of the differences observed previously between the NA49 and NA50 results are still there, in particular the difference in M_T slope, but the difference between multiplicities is not as dramatic as before (Figure 6.2).

The evolution of the ϕ multiplicities in NA50 has even reached a maximum in 2003, leading to a wide distribution of results (figure 6.3). The origin was not mainly inside

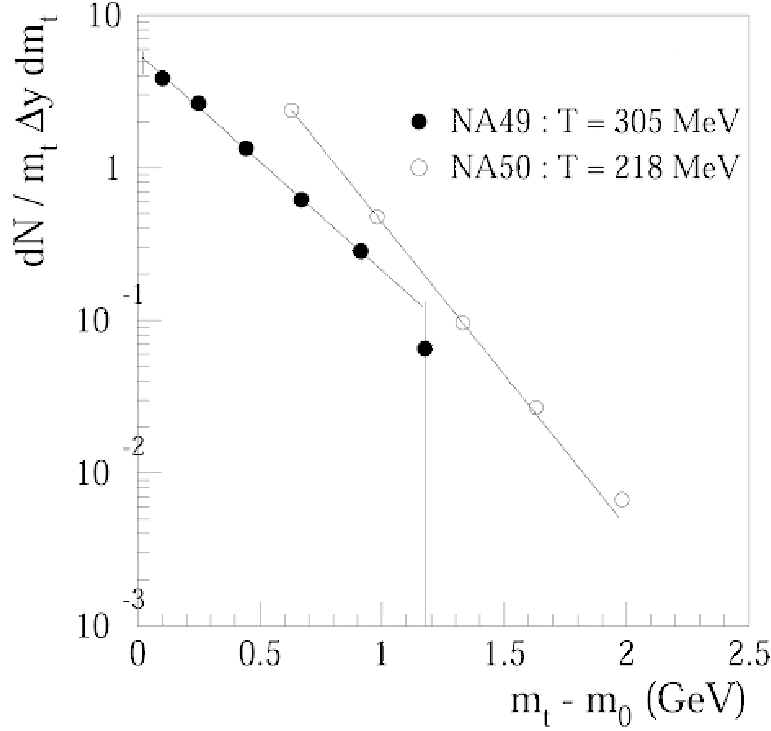


Figure 6.1: A comparison of the M_T spectra of ϕ meson in central Pb–Pb collisions at 158 A GeV measured by NA49 and NA50 (old results).

the NA50 experiment, but in the value of the ϕ branching ratio into dimuons. Indeed this value has always been poorly measured (at 20%), being for decades at the level of 2.5×10^{-4} . In 2000 the PPDB published another value, incompatible with the previous one (3σ difference): 3.7×10^{-4} . Both values were very different from the ϕ branching ratio into electrons, 2.99×10^{-4} . This later value should be very close to the one through dimuon channel, since one expects the value of the ϕ wave function at the origin to be the main parameter driving the branching ratios into leptons, and the difference in masses between electrons and muons to be negligible for the ω and ϕ . Indeed in 2002 the PPDB published a result for $BR_{\mu\mu}$ more precise and compatible with BR_{ee} , 2.89×10^{-4} . When one applies the same branching ratio, BR_{ee} , to all NA50 results, one obtains very similar results (Figure 6.4).

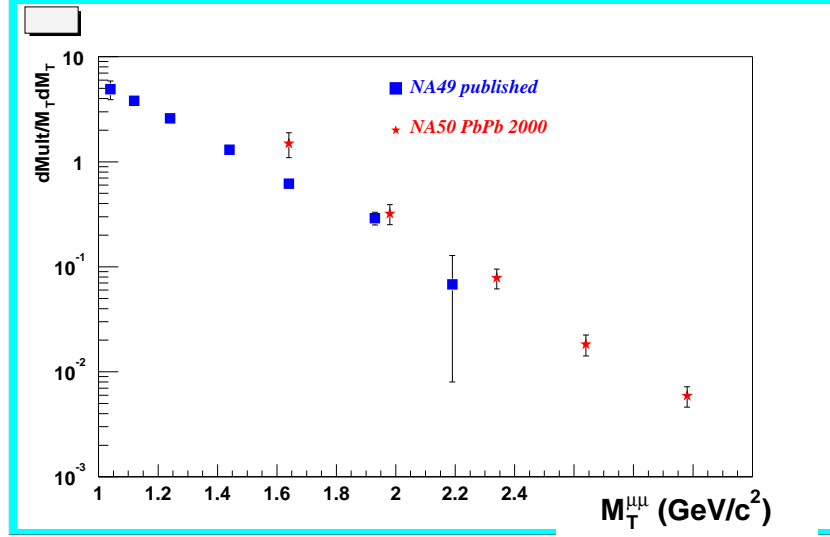


Figure 6.2: A comparison of the M_T spectra of ϕ meson as in figure 6.1 measured by NA49 and by NA50 obtained in this thesis.

Finally when comparing the various results, the slope difference between NA50 and NA49 remains, but the multiplicity differences are decreased. Assuming that the observed difference is linked to the different channels considered, models like [93] can account for part of the effect, at the level of 10%, which is sufficient to reconcile the two multiplicity measurements, but only for the highest M_T bins. Only NA60 measurement at lower M_T will be able to confirm the different trend that is observed here in the 1.5–1.8 GeV/c² bin. The low acceptance in our results could be suspected, but the instrumental checkings that have been performed [62] does not leave much room, a factor 2 assuming 100% change of the multiple scattering in the simulation, for the factor 3 observed.

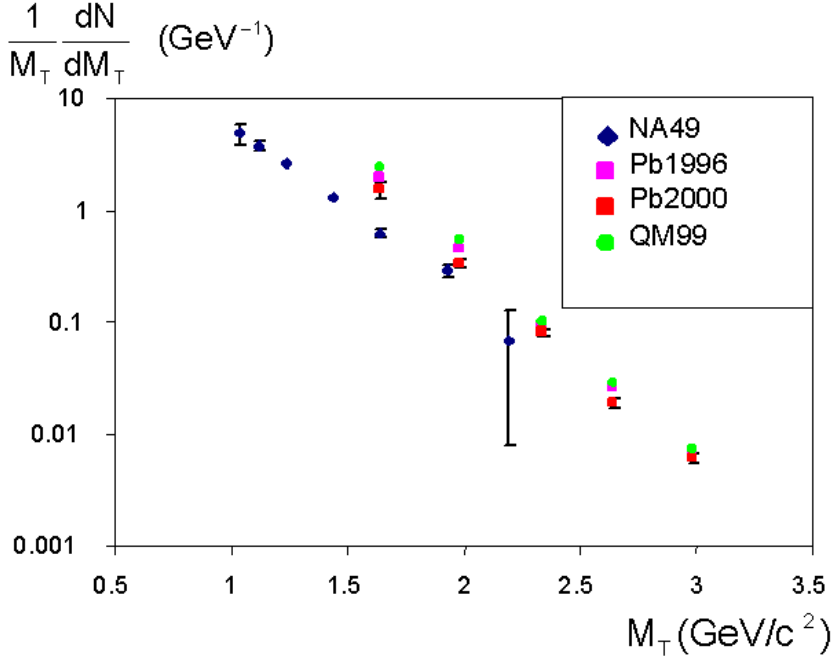


Figure 6.3: A comparison of the M_T spectra of ϕ meson as in figure 6.1 measured by NA49 and by NA50 in various analysis (early 1996 results, 1996, and 2000).

6.2 Comparison with lighter systems

NA38 experiment has measured ϕ meson production between various systems, in a wide range from proton induced to S-induced reactions. As previously explained, in NA38/NA50 two analyses have been performed concerning the ϕ and ω production. The analyses in p_T domains have been done on the p-W, S-S, S-Cu, and S-U, and the analyses in M_T domains have been performed in d-C, d-U, S-U and Pb-Pb (Figure 6.5). We will stick here to the latter analyses.

In the experimental kinematical window, figure 6.5 displays the evolutions of the ω and ϕ cross sections with respect to $A \times B$. It suggests:

1. A similar behaviour of ω and ϕ for light projectile (d-C to d-U) ;

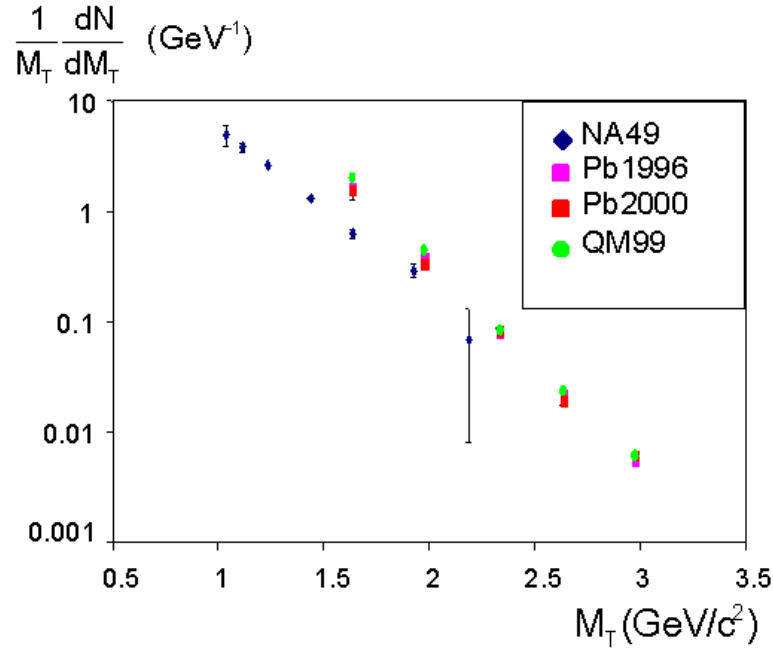


Figure 6.4: A comparison of the M_T spectra of ϕ meson as in figure 6.1 measured by NA49 and various analysis by NA50 considering the electrons branching ratio.

2. An increase of ω and ϕ cross sections for ion projectiles which is stronger than $A * B$ ($(AB)^\alpha$ with $\alpha = 1$) ;
3. An additional increase of the ϕ cross section .

Such behaviour could be linked to a trivial rapidity shift when going from the increase of target size (p-A) to the increase of projectile size (A-A), for the ω , and an additional increase of ϕ in A-A collisions.

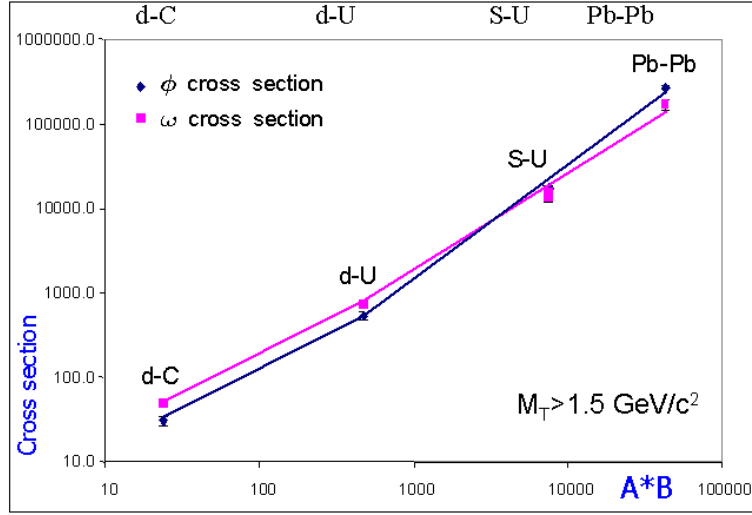


Figure 6.5: The dependence of ϕ and ω cross section for $M_T > 1.5 \text{ GeV}/c^2$ as a function of the product $A \times B$ of nuclear mass numbers of the colliding nuclei.

6.3 T slope of ϕ in Pb–Pb

From the first extractions of T slopes in NA50 Pb–Pb collisions for the ϕ , the results have been quite surprising, appearing below the one found for S-U[61]. For a part, this has been found to be linked to some bias in the first S-U 1991 data, but this trend is nevertheless present since the T slope of Pb–Pb for ϕ is at the level of S-U one, and probably lower (see figure 6.6).

Much more surprising has been the comparison with NA49 results, and the systematic made within this experiment, showing a lower value of the T slope in NA50, both for the ω and the ϕ , the difference being at the level 230 compared to 300 MeV (see figure 6.7).

The previous section has shown how the branching ratio can account for a part of the differences between the NA50 and NA49 ϕ multiplicities measured in their common M_T domain. Concerning the slopes, several effects can be considered, due to the difference in decay channels, but in particular the effect of the flow, which should lead to a flattening of the apparent slope in the low M_T region where the NA49 results stand. Figure 6.8

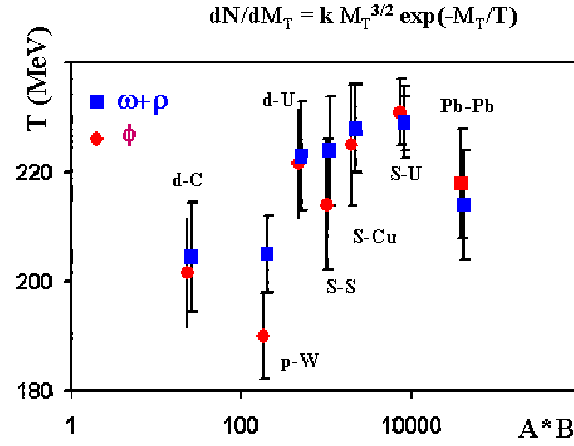


Figure 6.6: The T slopes of ϕ and $\rho + \omega$ versus $A \times B$ for different systems.

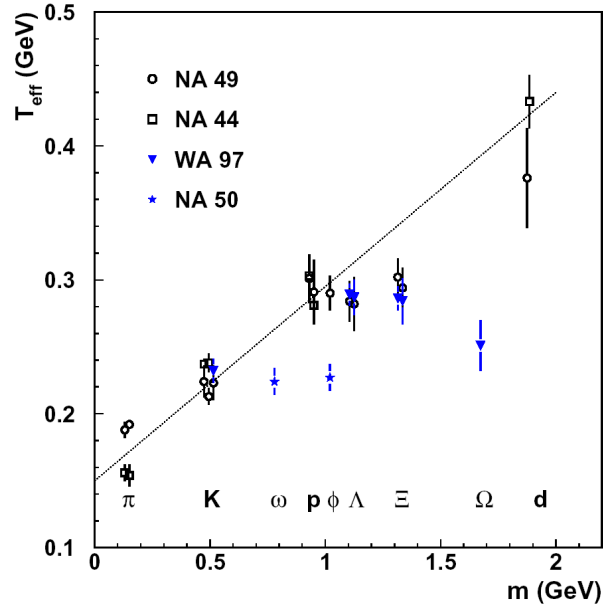


Figure 6.7: The T slopes versus particle masses measured by several experiments in Pb–Pb collisions at 158 GeV/c at SPS.

display some example of M_T spectra obtained in such a blast wave model [94].

It is also noteworthy that last results from NA49 at 80 and 40 GeV/nucleon lead to

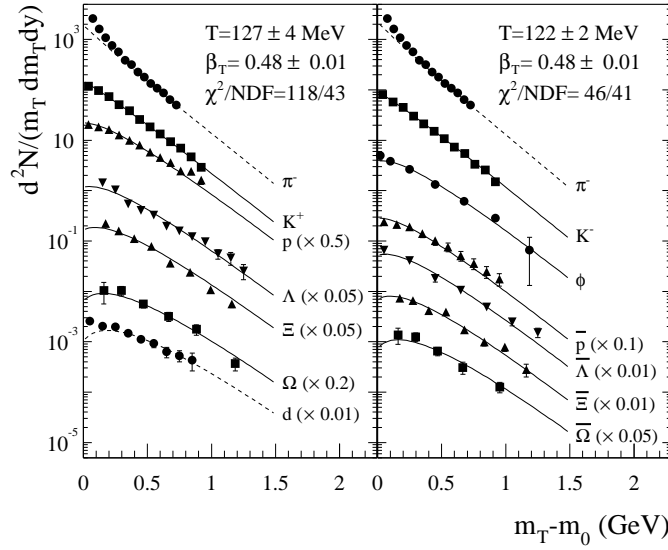


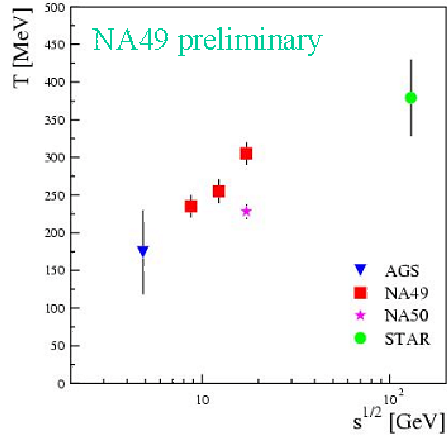
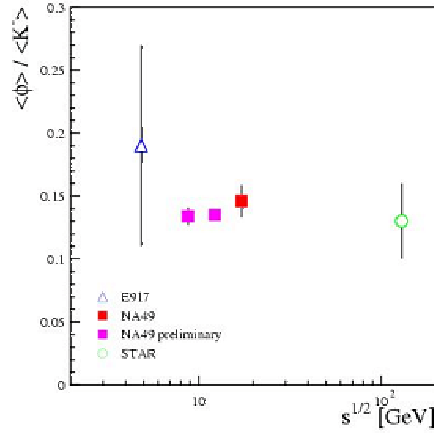
Figure 6.8: Blast wave fits to the transverse spectra measured by NA49. Pions and deuterons were excluded from the fits. (for 158 AGeV)

T slopes closer to the one we find at 158 GeV/nucleon [94] (figure 6.9). The T slope of ϕ from NA49 displays an increase with incident energy, in contrast to what is observed for K production (see Figure 1.16) but similarly to what is observed for Λ in NA49.

It is also noteworthy that for many trends, ϕ and K^- productions appears similar, contrarily with what is observed here for T slope at 158 GeV [94] (see figure 6.10). Extended systematic of the apparent T slope to lighter systems should be interesting here (as shown for NA50 in previous picture).

6.4 Incomplete saturation of strangeness

The γ_S as determined from the direct ϕ/ω measurement appears close to 0.7, when considering last ϕ branching ratio into dimuons, close to the one into electrons. What is the meaning of this value ? The answer is not completely clear, since various interpretations are considered in the literature, and there is no consensus on the γ_S value that can be inferred from experimental results, and sometimes not even on the fact that γ_S is needed[95].

Figure 6.9: T slopes of ϕ versus \sqrt{s} [94]Figure 6.10: The ratio of ϕ/K^- versus \sqrt{s} [94]

Taking into account secondary effects like reinteractions in the hadronic gas phase or weak decays, this value could be modified. Indeed ϕ meson could have small interaction cross section, contrarily to ω and ρ , and this could lead to a decrease of the ϕ/ω ratio in the hadronic phase, by an increase of the $\rho + \omega$ production. An original value of 0.9 could be possible in this framework [96]. But it is interesting and necessary to note that on the reverse side the weaker interaction cross section associated to the ϕ is not that solidly established neither [97].

Other authors [98] also consider that a γ_S value of 0.7 is actually associated to the central Pb–Pb collisions at SPS, but not for productions extrapolated from full rapidity (see figure 6.11).

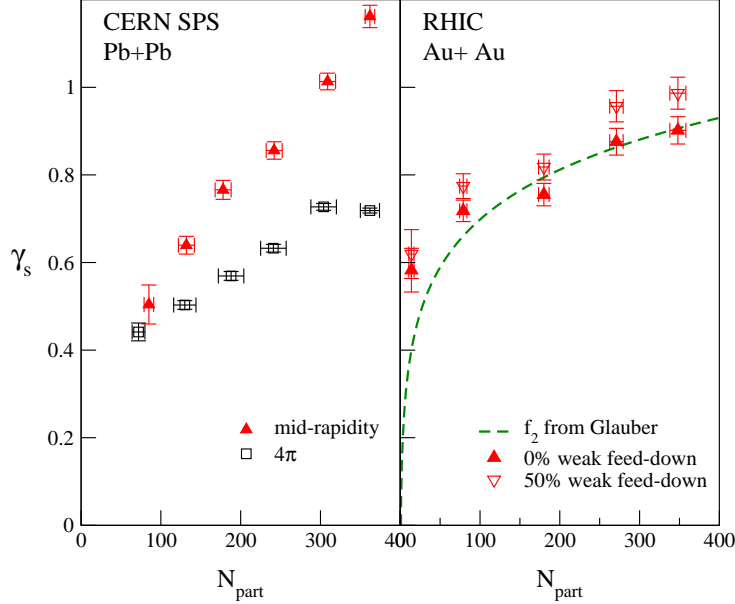


Figure 6.11: Left panel: Comparison of γ_S extracted from mid-rapidity NA49 data with the results of earlier analysis of NA49 4π -yields; Right panel: γ_S observed in Au+Au collisions as extracted from PHENIX data.

So if a partial saturation of strangeness seems to be increasingly probable, the value of γ_S is still a matter of debate, and appears to be dependent on the particles and rapidity domain considered, and to be sensitive to secondary effects. Local y - M_T ϕ/ω measurements should bring relevant information in this questioning. Already y - M_T integrated results seems to be able to separate between NA50 and NA49 ϕ production results [95], despite of the fact that they assume total strangeness phase space occupancy.

Chapter 7

Conclusions

The last NA50 measurement, aiming at extending the results toward more peripheral collisions and secure the last study made with minimum bias spectrum thanks to a redundant minimum bias trigger – in particular for high E_T domain, has confirmed most of the trends observed by the previous measurements.

- New results from 2000 data confirm that ϕ/ω ratio increases with the centrality of Pb–Pb collisions, suggesting a saturation tendency for the most central collisions (when observed with respect to E_T or to N_{part});
- The ϕ production per participant is increasing whereas the ω one is flat;
- The ϕ/ω ratio could give a direct access to the saturation factor $(\gamma_S/\gamma_q)^2$;
- The cross sections versus $A \times B$ increase from d–C to Pb–Pb indicate a two step pattern: rather similar behaviors for ω and ϕ in light projectile induced reactions, then both productions increase in ion projectile induced reactions $((AB)^\alpha$ with $\alpha > 1$);
- In addition, there is an additional increase for ϕ cross section.

Minimum bias extended study shows that:

- The ϕ multiplicity in NA50 is higher than the one observed in NA49. The differences of ϕ multiplicity between NA50 and NA49 are found to be smaller than previously determined, mainly due to the evolution of the branching ratio into dimuons, which has suffered dramatic changes in the recent years;

- The inverse slope T between NA50 and NA49 remains different, for NA50 the temperature stands at the order of $T_\phi = 220$ MeV, whereas for NA49 the temperature is higher $T_\phi = 305$ MeV;
- The 2000 data result has confirmed in another study that there is an anomalous J/ψ suppression at $E_T = 40$ GeV (See QM2002 [74]). Minimum bias study shown in this work displays no evidence of a second drop for J/ψ production at high E_T region (central collisions), but a continuous decrease is observed.

In thermal models, the ratio ϕ/ω in a M_T bin is directly related to $(\gamma_S/\gamma_q)^2$, the strangeness saturation factor. The value 2 observed for ϕ/ω should indicate a value of γ_S lower than 1, 0.7, when taking into account the branching ratios. It could indicate, as observed in several but not all analyses and predicted by some models, that the strangeness has not reached the full equilibrium, even in the hottest periods of the evolution of the system. But as we measure γ_S/γ_q , the observed value could also be due to a high γ_q value, leading to a value γ_S greater than 1, as underlined in the reference [99], which could signalize the boost of strangeness due to QGP formation.

Furthermore, Strangeness production from AGS to RHIC has displayed striking results, suggestive of sharp transitions which can be reproduced under assumptions of QGP formation.

Despite of the impressive recent successes of the thermal models, a comprehensive description of strangeness production seems to remain to achieve, from AGS to RHIC and including the detail of all strange particles, i.e. not only mainly based on Λ and K^+ which are the bulk of the production at SPS but also extended to all strange particles. It is clear that other strange production like ϕ , K^- and $\bar{\Lambda}$ have different behaviour, but with strong similarities between them [94].

Like incomplete strangeness equilibration which is observed through many thermal fits of particles abundancies and suggested by our results, a local equilibrium in rapidity domains could perhaps be also considered more systematically in order to progress on the selectivity of the description. This could also allow to account for baryonic local effects.

It is interesting to point out here that if the evolution with beam energy displays two different families, $K^+-\Lambda$ and $\phi-K^--\bar{\Lambda}$, such classification does not show up as a function of centrality, for instance for the ratio ϕ/K^+ , which could also induce some consistency problem for models using γ_S [98]. This stronger sensitivity to beam energy or collision system than to centrality is also suggested by a certain flattening of T slopes displayed by our ϕ and ω results for S-U and Pb-Pb.

In this interesting but involved situation, the ϕ could have special interest, since as a hidden strangeness particle it probably has no sensitivity to accompany particle production, contrarily for instance to K^+ with respect to Λ . The ω is the closest non strange vector meson, with identical other quantum numbers, and the closeness in mass is reducing any bias that could be associated to mass difference, like flow effect or when considering M_T integrated production. The ϕ/ω ratio could then have particular potential to characterize strangeness relative production irrespective of other local effects, for instance baryonic density. It is not obvious that this later characteristic of the medium is well described by an average on all rapidity domains, as the integrated thermal approach is assuming, and a correlated description in kinematical variables y and M_T at least should turn out to be more relevant. That is perhaps what is visible in [98] for ϕ/K^+ and γ_S value and its relationship to ϕ production. ϕ/ω ratios could bring additional information here.

The ϕ production, in particular with regards to ω one, follows the strangeness enhancement, but also could be a sensitive probe of the evolution of the system. Its reproduction by cascade models could still be a challenge, and the interpretation of the local determination of γ_S with the ratio ϕ/ω needs to be clarified in the models. It is then particularly important to get a clear picture of the experimental characteristics of this production, as we tried to do here. Additional comparison with NA49 for lighter systems should be probably interesting too in this respect. This will help to prepare meaningful studies of the production at RHIC, which will be obtained in the following years, following the first measurement of deuteron-gold, this year.

References

- [1] C.Y. Wong, *Introduction to High-Energy Heavy-Ion Collisions*, World Scientific, 1994.
- [2] J. Cleymans et al., *Phys. Rep.* **130**, 217-292 (1986)
- [3] E. Lasermann, *Nucl. Phys. A* **610** 1c-12c (1996); for a recent survey, see F. Karsch, *Nucl. Phys. A* **698** (2002) 199c
- [4] *Proc. of the large hadron collider workshop*, (Aachen Germany, 1990), ECFA, 90-133, CERN.
- [5] X.N. Wang, et al., *Phys. Rev.* **D44** (1991) 3521;
X.N. Wang, et al., *Phys. Rev. Lett.* **68** (1992) 1480.
- [6] J. D. Bjorken, *Phys. Rev. D* **27** (1983) 140-151
- [7] T. Matsui, H. Satz, *Phys. Lett. B* **178** (1986) 416
- [8] M.C. Abreu et al., *Physics Letters B* **410** (1997) 327-336
- [9] M.C. Abreu et al., *Physics Letters B* **410** (1997) 337-343
- [10] M.C. Abreu et al., *Physics Letters B* **450** (1999) 456-466
- [11] M.C. Abreu et al., *Physics Letters B* **477** (2000) 28-36
- [12] J. Alam, B. Sinha, and S. Raha, *Phys. Rep.* **273** (1996) 243
- [13] J. Alam, S. Sarkar, P. Roy, T. Hatsuda and B. Sinha, *Ann. Phys. (N.Y.)* **286** (2001)
- [14] Expt. WA98, M. M. Aggarwal, et al., *Phys. Rev. Lett.* **85** (2000) 3595
- [15] Expt. NA45 (CERES), R. Baur, *Z. Phys. C* **71** (1996) 571
- [16] Thomas Peitzmann, hep-ph/0111114.
- [17] A. Dumitru, L. Frankfurt, L. Gerland, H. Stocker, and M. Strichman, *Phys. Rev. C* **64** (2001) 054909
- [18] G. Agakichiev et al., (CERES Collaboration), *Eur. Phys. J.* **C4** (1998) 231
- [19] G. Agakichiev et al., (CERES Collaboration), *Phys. Lett. B* **422** (1998) 405.
B. Lenkeit et al., (CERES Collaboration), *Nucl. Phys. A* **661** (1999) 23c.
- [20] Johannes P. Wessels (for the CERES/NA45 Collaboration), *Nucl. Phys. A* **715** (2003) 262-271, also see nucl-ex/0212015

- [21] M.C. Abreu et al., *Euro. Phys. J.* **C14** (2000) 443
- [22] I.Tserruya, *Nucl. Phys. A* **681**, 133c (2001)
- [23] Marek Gazdzicki, Christina Markert, *Acta Phys. Polon. B* **31** (2000) 965-983, also hep-ph/9904441, and references therein.
- [24] S. Okubu, *Phys. Lett.* **5**, (1963); J. Iizuka, *Prog. Theo. Phys. Suppl.* 37-38 (1966).
- [25] J.Rafelski,B.Muller *Phys. Rev. Lett.* **81**, (1986)
- [26] Particle Data Group, D. Groom et al., *Eur. Phys. J.C* **14** (2000) 443
- [27] G. Odyniec, *Nucl. Phys. A* **681** (2001) 197c-204c
- [28] A. Shor, *Physical Review Letter* **54** (1985) 1122
- [29] P.Koch, U.Heinz and J.Pišút, *Phys. Lett.* **243** (1990) 149;
U.Heinz and K.S.Lee, *Physics Letters B* **259** (1991) 162
- [30] U.Heinz *Nucl. Phys. A* **661**, 140c (1999)
- [31] J. Cleymans and K. Redlich, *Phys. Rev. C* **60** 054908 (1999)
- [32] A. Tounsi, A. Mischke, Krzysztof Redlich, *Nucl. Phys. A* **715** (2003) 565c-568c, also hep-ph/0209284.
- [33] D.H. Rischke, M. Gyulassy, *Nucl. Phys.* **A608** 479 (1996);
Nucl. Phys. A **597**, 701 (1996)
- [34] E. Schnedermann, J. Sollfrank and U. Heinz, *Phys. Rev. C* **48**, 2462 (1993) [nucl-th/9307020]
- [35] N. Xu and M. Kaneta, nucl-ex/0104021; M. Gyulassy, nucl-th/0106072
- [36] P. Braun-Munzinger (GSI Darmstadt), K. Redlich (Uni. Bielefeld and Wroclaw), J. Stachel (Uni.Heidelberg) Quark Gluon Plasma 3, eds. R. C. Hwa and Xin-Nian Wang, World Scientific Publishing, nucl-th/0304013
- [37] U.Heinz *J. Phys. G* **25**, 263c (1999)
- [38] F. Grassi and O. Socolowski Jr., *J. Phys. G: Nucl. Part. Phys.* **25** (1999) 331-338.
- [39] R.Hagedorn, *Nuovo Cimento* **6** (1983) 1.
- [40] K.Kinoshita, H.Satz, D.Schildknecht, *Physical Review D* **17** (1978) 1834.
- [41] F.Becattini, hep-ph/0202071
- [42] Becattini F and Heinz U 1997 *Z. Phys. C* **76** 269
- [43] Becattini F and Passaleva G 2001 hep-ph/0110312, to appear in *Eur. Phys. J.*
- [44] Becattini F et al 1998 *Eur. Phys. J. C* **5** 143
- [45] Becattini F et al 2001 *Phys. Rev. C* **64** 024901
- [46] M. Gaździcki, see hep-ph/0305176

- [47] M. Gaździcki and M. I. Gorenstein, *Acta Phys. Polon.* **B30**, 2705 (1999).
- [48] M. I. Gorenstein, M. Gaździcki and K. Bugaev, hep-ph/0303041.
- [49] E.I Bratovskaya et al. *Nucl. Phys. A* **681**, 84c-91c (2001)
- [50] J.Rafelski, *Phys. Lett. B* **262**, 333 (1991) doi:10.1016/0370-2693(91)91576-H
- [51] F.Becattini, *J. Phys. G* **25**, 287-294 (1999)
- [52] J.Rafelski, Quark matter 2002 conference proceedings, *Nucl. Phys. A* **715**, 98c (2003)
- [53] F.Becattini, G.Pettini, hep-ph/0204340
- [54] E. Andersen et al., WA97 Collaboration, *Phys. Lett. B* **449** (1999) 401.
- [55] Proceedings of Quark Matter 2002, 18-24 July 2002, Nantes, France: V. Manzari et al., *Hyperon yields in Pb-Pb collisions from NA57 experiment*.
- [56] K. J. Anderson et al., *Phys. Rev. Lett.* **27**, (1976) 799
- [57] F.Becattini, *J. Phys. G* **28** (7), 1553-1560 (2002)
- [58] D.Jouan (NA50), proceedings of PANIC 2002, Osaka, to be published in *Nucl. Phys. A*, (2003)
- [59] B. Alessandro, et al., NA50 Collaboration, *Phys. Lett. B* **555** (2003) 147-155.
- [60] D.Jouan/NA38-NA50, APH N.S., Heavy Ion Physics 4 (1996) 155-165
- [61] J.Astruc, these de l'universite paris 6, 9 Juillet 1997, IPNO-T-97-31
- [62] L.Villatte, thesis PARIS VII, Universit Denis Diderot (2001)
- [63] B. Alessandro et al., *Nuclear Instruments and Methods in Physics Research A* **493** (2002) 30.
- [64] J.D.Jackson, *Nuovo Cimento* **34A** (1964) 1644.
- [65] B.Friman, *Nuclear Physics A* **610** (1996) 358c.
- [66] E. Schnedermann, J. Sollfrank and U. Heinz, *Physical Review C* **48** (1993) 2462; U. Heinz, *Nuclear Physics A* **685** (2001) 414c.
- [67] S.V.Afanasiev et al. *Phys. Lett. B* **491**, 59-66 (2000)
- [68] D.Rohrich, Quark matter 2002 conference proceedings
- [69] J.L. Nagle for PHENIX Collaboration, *Nuclear Physics A* **715** (2003) 252c-261c
- [70] S.C. Johnson, B.V. Jacak and A. Drees, *E. Phys. J.* **C** 18 (2001) 645; P. Filip and E. Kolomeitsev, *Phys. Rev. C* **64** (2001) 054905; S. Soff et al., *J. Phys. G* **27** (2001) 449; S. Pal, C.M. Ko and Z.-W. Lin, *Nucl. Phys. A* **707**, 525(2002)
- [71] PHENIX Collaboration, D. Morrison, et al., *Nucl. Phys. A* **638** (1998) 565c
- [72] PHENIX Collaboration, W. Zajc, et al., *Nucl. Phys. A* **698** (2002) 39c
- [73] B. Alessandro et al., *Nucl. Phys. B* **44** (1995) 303

- [74] L.Ramello/NA50 collaboration, Quark matter 2002 conference proceedings
- [75] R. Arnaldi/NA50 Collaboration, Heavy Ion Forum, Torino, CERN 1999; J.-P. Blaizot, P.M. Dinh, J.-Y. Ollitrault, *Phys. Rev. Lett.* **85** (2000) 4012, also QM2001 proceedings.
- [76] M.C. Abreu et al., *Physics Letters B* **499** (2001) 85
- [77] R. Arnaldi, et al., *Nuclear Instruments and Methods in Physics Research A* **411** (1998) 1
- [78] R. Shahoian, NA50 Collaboration Meeting, February 2001.
- [79] L. Ramello, NA50 Collaboration Meeting, 13 May, 2002.
- [80] D.Jouan, et al., 4 june 2002, preprint IPNO 02-015
- [81] Helena Santos, NA50 Collaboration Meeting, March 2002.
- [82] C. W. Jager, H. Vries and C. Vries, *Atomic Data and Nuclear Data Tables* **14** (1974) 479
- [83] A. Bialas et al., *Nucl. Phys. B* **111** (1976) 461-476
- [84] Thesis of Carlos Manuel A. L. Lourenco, page 72, Jan/1995.
- [85] Particle Data Group, July 2002, *Phys. Rev.* **D66**, 010001 (2002).
- [86] M. Aguilar-Benitez, et al., LEBC-EHS collaboration, *Z. Phys. C* **50** (1991) 405.
- [87] F.Bellaiche et al., *Nucl. Instr. and Meth. A* 398 (2-3) (1997) 180-188
- [88] G.D.Lafferty and T.R.Wyatt, *Nucl. Instr. and Meth. A* 355 (1995) 541-547
- [89] D. Jouan, NA50 collaboration meeting, June, 2003.
- [90] D.Jouan/NA38-NA50, *Nuclear Physics A* 638 (1998) 483c-486c
- [91] N.Willis/NA50, *Nucl. Phys. A* **661**, 534-537 (1999)
- [92] D.Jouan, T.Wu, et al., (NA50 collaboration), Proceedings of strangeness in quark matter conference, Atlantic beach, NC, USA, 12-17 march 2003, to be published in *Nucl. Phys. A* , (2003)
- [93] Johnson, B.Jacak and A.Drees, *Euro. Phys. Jour. C* **18** 645-649 (2001)
- [94] V.Friese, proceedings of strangeness in quark matter conference, Atlantic beach, NC, USA, 12-17 march 2003, and nucl-ex/0305017
- [95] J.Stachel, 7th International Conference on Strangeness in Quark Matter, Atlantic Beach, NC, USA , 12 - 17 Mar 2003, proceedings to be published
- [96] F.Becattini, private communication.
- [97] L. Alvarez-Ruso and V. Koch, *J. Phys. G* **28**, 1527-1534 (2002)
- [98] J.Cleymans, B.Kampfer and S.Wheaton, *Nucl. Phys. A* **715**, 553c (2003)

- [99] J. Rafelski, G. Torrieri and J. Letessier, Presented in October 2000 at the 6th International Workshop on *Relativistic Aspects of Nuclear Physics*, Tabatinga, Sao Paulo, Brazil.